学位論文

Precise Position Determination of Radio Core in Blazar Mrk 501 by mm-VLBI Observations

（ミリ波VLBI観測による ブレーザーMrk 501の電波コアの高精度位置決定）

平成24年12月 博士（理学）申請

東京大学大学院 理学系研究科
天文学専攻
小山 翔子

Abstract

Relativistic jets in Active Galactic Nuclei (AGNs) are believed to be powered by their central super massive black holes. Blazar is a sub-class of AGN jets in which a jet of magnetized plasma with relativistic bulk velocity pointing close to the line of sight. Recent progress in high energy observational tools makes it possible to characterize X-ray light curves of blazars by half-day time scale variability. The size of X-ray emitting blobs is constrained by the time variability, however, little is known about their positions in the jet flow due to a lack of spatial resolution of X-ray telescopes. Observational properties of X-ray light curves in blazars are well explained by the standard internal shock model and positional changes of X-ray emitting blobs at $\sim 0.1 - 10$ pc (several hundreds μas at angular distance of 1 Gpc) are expected based on the model. In order to test the internal shock model in blazars, we clarify spatial distribution scale of positions of X-ray emitting blobs by conducting multi-epoch phase-referencing observations with VLBI (Very Long Baseline Interferometry). VLBI phase-referencing observations attain a highest positional accuracy among all of the currently existent telescopes and they are able to reach the positional accuracy comparable to expected spatial distribution scale of X-ray emitting blobs. We select one of the closest TeV blazars Mrk 501 ($z = 0.034$) as our target source. Observation frequency is 43 GHz to avoid synchrotron self-absorption. Further, since the non-thermal emission from radio to X-ray is radiated by same electron populations, the positions of X-ray emitting blobs are identical to the radio core positions.

VERA (VLBI Exploration of Radio Astronomy) observations were performed for successive four-days in February and October 2011, and VLBA (Very Long Baseline Array) observations were performed in February, March, May, and June 2012, respectively. We successfully measure the phase-referenced radio core positions in a blazar by VLBI for the first time. Successive four-days observations with VERA achieved a positional accuracy of $\sim$110 μas, and a single VLBA observation achieved a positional accuracy of ~ 35 μas. Among more than one month interval observations, radio core positions along the jet axis remain stationary, and distributed within 220 μas (2.0 pc) by VERA and 130 μas (1.2 pc) by VLBA. Based on our observational results, we constrain on the bulk Lorentz factor ratio of a maximum bulk Lorentz factor divided by minimum one, spanned over more than one month, is ≤ 1.9 in the framework of internal shock model. During large X-ray flaring states, we expect significant position change of X-ray emitting blobs could be detectable with VERA and VLBA phase-referencing observations, and test the adequacy of internal shock model for blazars.

Additionally, we study the detailed structure and its kinematics at the root of the jet of

Mrk 501 by using the positions of radio core determined by our astrometric measurements. From our images after 2010 May, we find a new component NE, located 200 μas northeast to the radio core with several tens mJy, orthogonal to jet axis. The positions of component NE, referencing to the radio core, are distributed within ~ 200 μas, comparable to the distribution range of radio cores. The ratio of radio core flux to the flux of component NE can be explained in a framework of the internal shock model. When the locations of component NE and radio core correspond to the location of internal shock region, we estimate the location of the central engine is ~ 550 μas (5.2 pc) upstream of radio core, and the intrinsic opening angle of the jet is $\sim 1.8°$.

Contents

Chapter 1

Introduction

1.1 Unified Picture of Active Galactic Nuclei

In the universe, ∼10% of galaxies contain active nucleus emitting the power $\sim 10^{2-4}$ times as high as their host galaxies do (e.g., Peterson, 1997). The compact nucleus at a galactic center which emit total power $\sim 10^{42-48}$ erg s^{-1} is called Active Galactic Nuclei (AGNs). AGNs show non-thermal broad spectral energy distribution (SED) ranging from radio to X-rays or Very High Energy (VHE). It is thought that AGNs are powered by super massive black hole (SMBH) at their galactic centers. AGNs are classified into two classes with their radio loudness, divided by ten times 5 GHz flux over B-band flux, called radio-loud AGN and radio-quiet AGN (Kellermann et al., 1989). Around 10% of AGNs are radio-loud AGN. They have jet structure, which are the fast collimated outflow powered by gravitational energy released when the gas of an accretion disk fall onto SMBH (e.g., Urry & Padovani, 1995).

There are various subclasses both in radio loud and radio quiet AGNs in terms of observational properties, such as properties of optical emission line, radio loudness and time variability. However, we can understand the subclasses as unified picture with the differences of their luminosities and viewing angles (the angles between jet direction and the line of sight). The unified AGN jet scenario is suggested by Urry & Padovani (1995) and Antonucci (1993). Figure 1.1 shows a unified picture of AGNs. The black hole, the accretion disk, and the Broad line regions (BLR) are surrounded by the molecular torus. Narrow line regions (NLR) are seen in the optical spectrum of most AGNs, with line widths corresponding to random velocities of a few hundred kilometers per second. Since BLR are inferred from line widths of a few thousand kilometers per second, BLR is considered located in more inner part of the NLR. Therefore, BLR can be observed only at small viewing angles without obscuration by the molecular torus, while the NLR can be observed at any viewing angles because of significantly larger linear scale. For radio-loud AGNs, we call the former case as Broad Line Radio Galaxy (type I AGN for radio-loud AGNs) and the later case as Narrow Line Radio Galaxy (type II AGN for radio-loud AGNs). Blazars, the subject of this thesis, are considered as AGNs with relativistic jets viewed pole-on (type 0 AGN for radio-loud AGNs). The radio quiet AGNs which are not associated

with jet structure include Seyfert I and Seyfert II galaxies (Osterbrock, 1981) are also shown in Fig. 1.1.

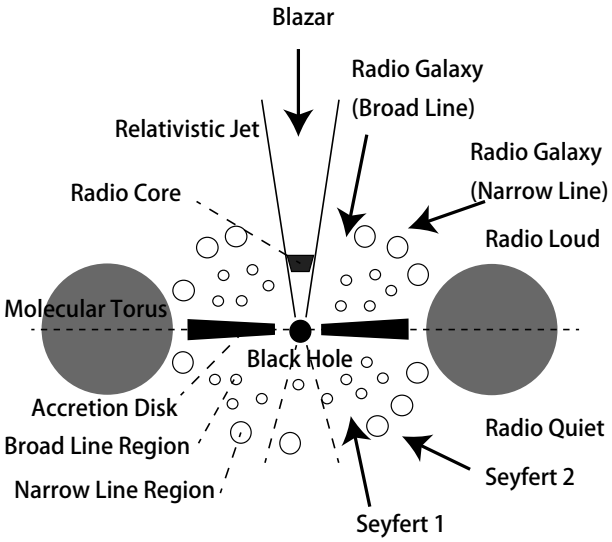

Figure 1.1: A schematic picture of unified AGN jet model obtained by Urry & Padovani (1995).

1.2 Blazars

Here we introduce the observational properties and their interpretations of blazars, as the target AGN subclass of this thesis.

1.2.1 General properties

Blazars are characterized by large amplitude variability of optical emission during more or less than 1 day, wide non-thermal emission from radio to γ-rays, and high fractional polarizations of $\sim$ several %. These characteristics are successfully explained by the unified picture of AGNs that the blazars have the relativistic non-thermal jets align close to the line of sight.

In 1990s, EGRET on Compton Gamma Ray Observatory discovered the strong γ-ray emission from more than 60 blazars out of 61 γ-ray AGNs in the GeV band (Hartman et al., 1999). These days, γ-ray emission from 862 blazars out of 882 AGNs have been reported by the second LAT AGN catalog (2LAC) obtained by the Fermi Large Area Telescope (LAT) (Ackermann et al., 2011). High Lorentz factor jet is required for γ-ray photons to escape from two-photon pair creation $\gamma\gamma \rightarrow e^+e^-$ (Begelman et al., 2008). Model fitting to broadband spectrum energy density also requires high Lorentz factor for blazar jets. If an emission blob radiating

isotropically in the rest frame moves relativistic speed β (normalized del by speed of light c ($\beta \equiv v/c \sim 1$, the photons are concentrated in a narrow cone of half angle $\theta^* \sim 1/\Gamma$ in AGN frame (e.g., Rybicki & Lightman 1979, §A.1.4), where Γ is the Lorentz factor of emission blob in the observer's flame, defined as $\Gamma = (1 - \beta^2)^{-1/2}$. Therefore, the observer's line-of-sight should lie within the beaming corn. θ and high Γ (β) are connected by Doppler beaming factor $\delta = [\Gamma(1 - \beta\cos\theta)]^{-1}$. The observed luminosity from relativistic jets with small viewing angle is highly Doppler-boosted by δ^4, where factor δ comes from the light aberration in solid angle, factor δ from blue shift of the frequency, and factor δ from the time dilation (§A.1.5). Therefore, the emission from other parts (e.g., accretion disk, line emission region) is mostly overwhelmed by the strong jet emission. Polarization observed in the radio and optical band also implies the most of the radiation is non-thermal synchrotron from relativistic electrons in the magnetic field (e.g., Gabuzda et al., 2006).

1.2.2 Broadband spectrum energy density

The broadband SED of blazars ranging from radio to TeV or GeV γ-rays has two peaks. The low energy component extends from the radio to UV, and sometimes extends to the X-ray bands. From the high polarization, the low energy component ranging from radio to UV or to X-rays comes from synchrotron emission of relativistic electrons in magnetic field. The high energy component is due to Compton up scattering by same population of relativistic electrons. The seed photons could be synchrotron photon emitted in the same region (SSC), or external to the jet (ERC), such as broad emission line clouds or the accretion disk (e.g., Ghisellini et al., 1998).

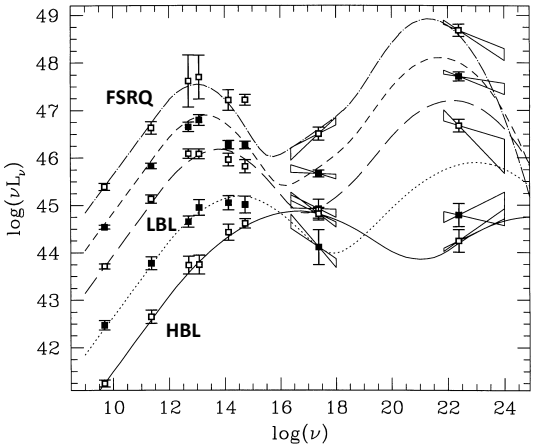

Figure 1.2: Averaged SED of all types of blazars, taken from Fossati et al. (1998).

Blazars are divided into two main subclasses, BL Lac objects and Flat Spectrum Radio Quasar (FSRQ). Blazars, which are lack of strong emission or absorption line, are called BL Lac objects.Since BL Lac objects are characterized by the absence of emission lines, contribution from the external radiation field would be negligible and SSC process is expected to be dominant. FSRQ is a blazar subclass which also belongs to quasar class, which has high optical magnitude ($<\sim -23.5$ mag) (e.g., Urry & Padovani, 1995). BL Lac objects are often separated into two groups by the synchrotron peak frequency. BL Lac objects, which synchrotron peak frequency is in UV-X-ray region, is called HBLs (High-Energy peaked BL Lacs), and in IR-optical region, is called LBLs (Low-Energy peaked BL Lacs) (Fossati et al., 1998). The authors collect data for 126 blazers and find a clear trend that as the total power decreases, both low and high energy components shift to the higher frequencies, and at the same time the γ-ray luminosity decreases. The averaged SED of FSRQ, LBL, and HBL, divided by radio luminosity, is shown in Fig. 1.2.

TeV blazers are usually classified into HBLs, because the peaks of their low energy components reach to the X-ray energy band. Multi-band spectra of TeV blazers (HBLs) are well fitted by SSC process in homogeneous one-zone approximation (e.g., Finke et al., 2008).

1.2.3 X-ray time variability

For TeV blazers, X-rays provide the best means for studying variability because X-ray flux is produced by electrons that are accelerated to the highest energies where the cooling timescales are most rapid (estimated in §A.2.3). X-ray emission from TeV blazar is known to show rapid and high-amplitude intensity variation, so-called flares. X-ray light curves of TeV blazars show the short-term variability, which means multiple flares occurring on timescales of about 1 day during continuous $\sim$7 days (e.g., Takahashi et al., 2000; Tanihata et al., 2001), and the long-term variability, which represents high amplitude variation spanned more than one month (e.g., Isobe et al., 2010). X-ray daily flares of TeV blazars were first observed in Mrk 421 (Takahashi et al., 2000), and then confirmed in Mrk 501 and PKS 2155-304, not only during flaring state but also quiescent state (Tanihata et al., 2001).

In Fig. 1.3, ASCA X-ray light curve of Mrk 421 over successive seven-days is shown. Detail analysis of multi-epoch light curves reveal that the time scale of the width of the daily flares are similar to the timescale of the flares peak-to-peak. Another observational fact is that the X-ray flares always appear to lie on top of an underlying offset-like component (Takahashi et al., 2000; Tanihata et al., 2001). The observations indicate that there is always offset-like component such that a flare does not start from zero but from the offset (see Fig. 1.3).

Statistically the variability is analyzed through structure function, which shows that there is clearly a characteristic time scale $\sim$0.5-1 day for above three TeV blazars. The variability power at shorter timescales than the characteristic time scale is strongly suppressed (Kataoka et al., 2001; Tanihata et al., 2001). By comparing the various possible time scales and concerning the symmetric flare component, it was suggested that the characteristic time scale is determined by some dynamical time scale, instead of cooling or acceleration times (Kataoka et al., 2000).

If the X-ray emitting blobs with a Lorentz factor of $\Gamma \simeq 10$ are approaching toward us, the characteristic timescale of each flare event should reflect the observed size of emitting blobs being $\leq 10^{16}(\Gamma/10)$ cm, or ≤ 0.01 pc by using the relation $R \lesssim c\Delta t\Gamma$ (Kataoka et al., 2000), where Δt is variability time scale. However, since X-ray observations are lack of spatial resolution, the positions of X-ray emitting blobs could not be studied at all so far.

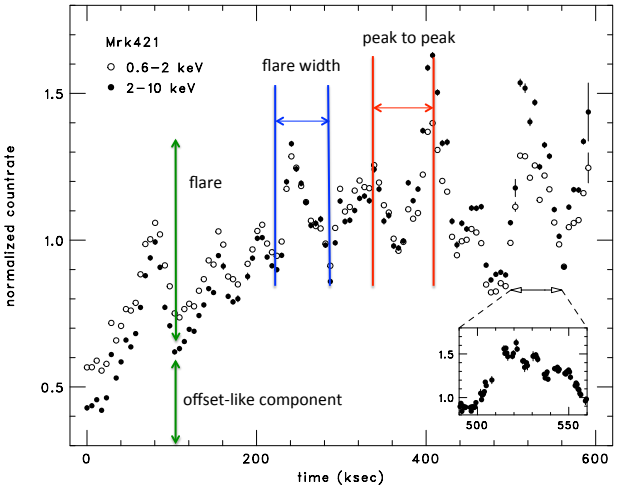

Figure 1.3: ASCA X-ray light curve for TeV blazar Mrk 421 in 1998 April, obtained from Tanihata et al. (2001).

1.2.4 VLBI observations

VLBI is the most appropriate tool for resolving AGN jets because of its highest spatial resolution among all of the existent observing tools. In the apparent upstream end of AGN jet, a brightest and innermost compact feature is called as "radio core," which is observed by VLBI (e.g., Pushkarev et al., 2012). In Fig. 1.4, a radio core image observed by VLBI is shown. Below, we introduce VLBI observational phenomena of blazars.

We divide the radio cores in terms of their opacity. Firstly, the radio core, showing optically thick spectrum for most of blazars, is considered as a brightness surface with an optical depth ~ 1 at each observing frequency. On the standard jet model (Blandford & Königl, 1979), the optical depth of radio core strongly depends on the radial profiles of the magnetic field strength $B(r)$ and the electron number density $N_{\rm e}(r)$. Assuming $B(r)$ and $N_{\rm e}(r)$ have power-law profiles of the distance from the central engine r ($B(r) \propto r^{-m}, N_{\rm e}(r) \propto r^{-n}$, $m > 0$, and $n > 0$), the core absolute position shifts upstream at higher frequencies as assuming the steady jet, that

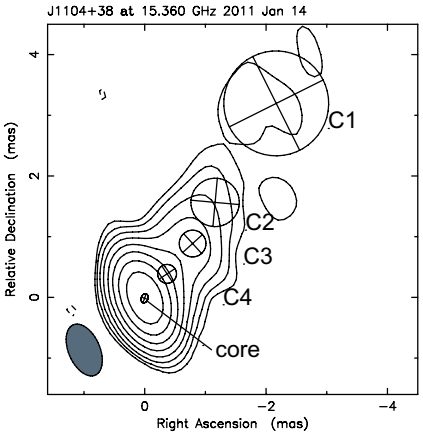

Figure 1.4: An example of VLBI image of blazar core. This is the VLBI image of well-known TeV blazar Mrk 421 at 24 GHz. Component C1, C2, C3 and C4 are the extended jet component.

is, $r \propto \nu^{-1/k_{\rm r}}$, where $k_{\rm r}$ depends on m, n, and the shape of electron energy spectrum (Konigl, 1981). The core shift phenomena are actually measured in many radio cores by referencing the radio core position to optically thin jet features which positions are not expected to change with frequency (e.g., Lobanov, 1998; Kovalev et al., 2008; O'Sullivan & Gabuzda, 2009; Sokolovsky et al., 2011).

On the other hand, recent simultaneous VLBI observations reveal that several radio cores have optically thin spectrum at higher frequency (Sokolovsky et al., 2010). Marscher et al. (2008) observed the γ-ray flare occurred when the polarized emission blob passed through the optically thin radio core in the BL Lac by VLBA 43 GHz (see Fig. 1.5). Similar phenomena are observed in several blazars (e.g., OJ 287: Agudo et al. 2011b, 3C 454.3: Jorstad et al. 2010). They suggest a physical model to explain the phenomena that the radio core corresponds to the conical standing shock located $\sim 10^5 R_s \sim 10^{18-19}$ cm away from the central black hole, and the γ-ray flares occur when the other shocks pass through the standing shock. However, the model is only based on VLBI observations, such that it has not been able to explain any other blazar characteristics, such as the short time variability of X-rays.

1.2.5 Internal shock model as a promising model for X-ray emission

Time variability of blazars shown in §1.2.3 have been naturally explained by the internal shock model (e.g., Spada et al., 2001a; Guetta et al., 2004; Tanihata et al., 2003). The key idea of the internal shock model is a shock-in-jet scenario, where the central engine injects discrete energy into the jet, producing individual blobs having slightly different bulk Lorentz factors. When a faster and later blob catches up to a slower and former one, they collide each other, form a shock, and then particles are accelerated to very high energies and radiate the

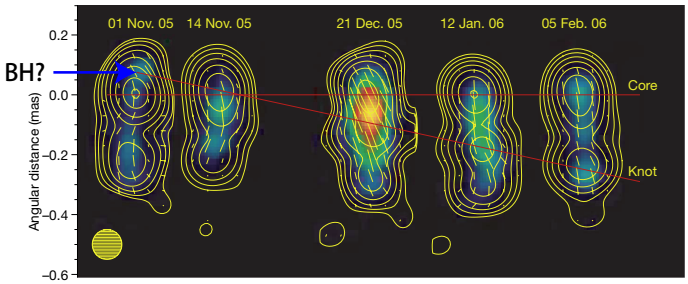

Figure 1.5: VLBA images of BL Lac at 43 GHz, taken from Marscher et al. (2008). They suggest that the location of the central black hole is 0.7 pc upstream of the radio core.

non-thermal emission. This internal shock model is standard for explaining the emission of gamma-ray bursts (e.g., Kobayashi et al., 1997; Piran, 1999). The formation of shocks in AGN jets is likely to be related to intrinsic velocity irregularities of the flow, caused by the non-steady operation of the central engine (Rees, 1978).

Several numerical simulations of internal shock model show the distance between the internal shock region and the central engine is typically 10^{17-19} cm (eg., Fig. 1.6). Tanihata et al. (2003) also shows both of the offset-like components and the flare of blazar X-ray light curve can be well reproduced by internal shock model. Compared to the successive seven-days X-ray light curves, they found the fractional fluctuation of the initial bulk Lorentz factors must be small, $\sigma'_\Gamma \equiv \sigma_\Gamma/\Gamma_{\rm avg} \leq 1.01$, where $\Gamma_{\rm avg}$ is the averaged initial bulk Lorentz factors and σ_Γ is the Gaussian distribution width of initial bulk Lorentz factors (see Fig. 1.7). Compared to Fig. 1.3, low fractional fluctuation of the initial bulk Lorenz factors (Fig. 1.7a) is more realistic within successive seven-days. However, the fluctuation of the initial bulk Lorentz factors over one month interval has not been studied yet.

The model of Tanihata et al. (2003) contains efficiency problem, that is, the dynamical efficiency for converting the kinetic energy into the internal energy in a single collision (ϵ) is quite small. For instance, when the fractional fluctuation of the initial bulk Lorentz factors in a single collision $a \leq 1.01$, $\epsilon \sim 10^{-5}$ estimated by eq. (A.36). This indicates that the extended jet is 10^5 times energetic than is observed X-ray emitting blob. On the other hand, there is no measure of the energetics of the entire jet, such low radiative efficiency near the core cannot be ruled out. The easiest way to increase the efficiency would be to have larger a. Most of previous studies on internal shock models apply the fractional fluctuation of the initial bulk Lorentz factors as $1 \leq a \leq 20$ to increase the efficiency (e.g., Spada et al., 2001b; Kino et al., 2004; Kino & Takahara, 2008; Mimica & Aloy, 2010). (For instance, in §A.2.1 if $a = 3$, the dynamical efficiency is estimated to be $\epsilon = 0.13$, and if $a = 20$, $\epsilon = 0.57$.) However, their simulated light curves are difficult to reproduce the observed flux ratio of the flare to the offset-like component.

Tanihata et al. (2003) consider the possibility of the external shock model for explaining

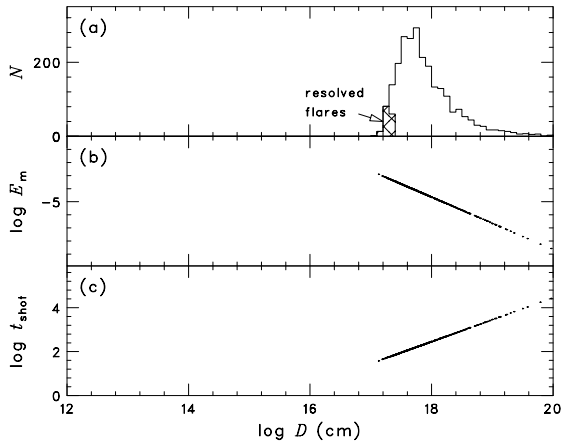

Figure 1.6: Results of a simulation of the internal shock model in Tanihata et al. (2003). They assume $\Gamma_{\rm avg} = 10$, $\sigma'_\Gamma = 0.005$, and blob ejection interval $D_0 = 3 \times 10^{13}$ cm. (a) The histogram of the collision distances D ranges 10^{17-19} cm. (b) Closer the collision occurred from the central engine, larger the dissipated energy is. (c) The generated timescale of the flare at the collision is short at the close collision distance.

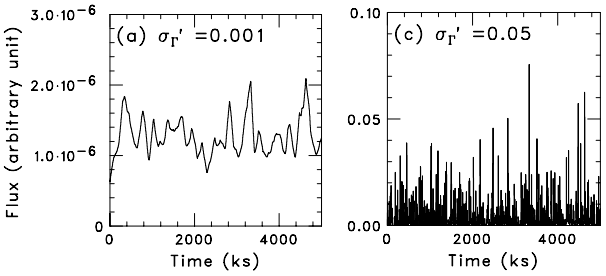

Figure 1.7: Simulated light curves based on internal shock model for the case of $\sigma'_\Gamma = (a)$ 0.001, (c) 0.05. $\Gamma_{\rm avg}$ and D_0 are same as in Fig. 1.6. The relative amplitude of the flare to offset component increases when the fractional fluctuation of the initial bulk Lorentz factors become large.

X-ray light curve of blazar. In the external shock case, to reproduce the daily flares at least over successive ten-days, ten "ordered clumps" of the external material are required for collisions with the jet. The external shock model cannot be rejected, however, more fine-tuning of the parameters is necessary as compared with the internal shock model.

1.3 Purpose of Our Study

To measure the multi-epoch positions of X-ray emitting blobs in blazars is crucial for testing the internal shock model. In this work, we aim to clarify a spatial distribution scale of X-ray emitting blobs in a blazar. However, the positions of X-ray emitting blobs in blazars have not been observationally measured so far. In the case of optically thin radio core in TeV blazars, the co-location between X-ray emitting blobs and radio core is ensured. From the numerical simulations of the internal shock model as a standard mechanism for X-ray emission, it is suggested that the X-ray emitting blobs would distribute several hundreds of μas at a angular distance of 1 Gpc ($\sim 0.1 - 10$ pc) (e.g., Tanihata et al., 2003; Spada et al., 2001a), which is comparable to the positional accuracy of phase-referencing VLBI observations. Therefore, we aim to measure the spatial distribution scale of X-ray emitting blobs with typically ~ 150 μas accuracy by conducting multi-epoch phase-referencing VLBI observations toward a optically thin radio core in TeV blazars. Further, we try to interpret the measured spatial distribution scale in the framework of internal shock model, by constraining the bulk Lorentz factor ratio.

1.4 Methodology

1.4.1 Relation between X-ray emitting blobs and radio core of TeV blazars

Since TeV blazars belong to HBLs, single population of relativistic electrons radiate both of radio and X-ray emission. Especially, in the case of optically thin radio core in TeV blazars, co-location between X-ray emitting blobs and radio core is ensured. Although the size of X-ray emitting blobs is $\sim 10^2$ times smaller than that of radio core and the cooling time scale of X-ray emission is $\sim 10^2$ times shorter than radio emission, peak position of radio core can be identical to dominant X-ray emitting blobs. In Fig. 1.8, we show the schematic picture of the relation between X-ray emitting blobs and radio core for TeV blazars.

1.4.2 Absolute position measurements

Standard VLBI data reduction lose the information of the absolute source position through self-calibration process. To measure the accurate position of radio core, we use phase-referencing technique of VLBI. In phase-referencing observations, a target source and a phase-calibrator close to the target on the sky are alternately observed within a short interval time, and then the

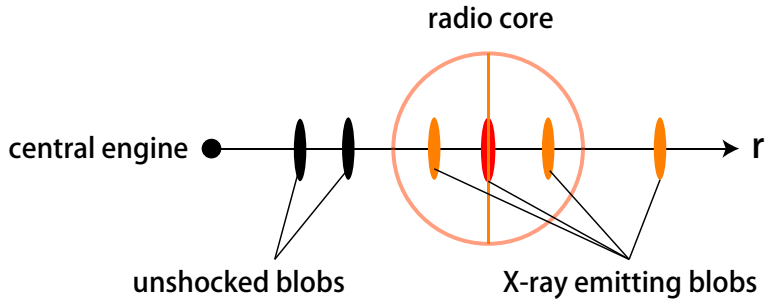

Figure 1.8: Schematic picture of the relation between X-ray emitting blobs and radio core for TeV blazars. The location of dominant X-ray emitting blob shown as red filled circle corresponds to the peak position of radio core.

phases obtained for the calibrator are subtracted from those of the target. If two sources are close enough on the sky, we can reasonably assume that the radio waves from both sources pass through the nearly same part of the propagating medium, so the differences in the propagating medium can be removed. If two sources are more than a few degrees apart, the position accuracy is dominated by propagation delay error so that it does not depend on the observing frequency so much. For example, if the separation of phase-referencing pair is two degrees, the position accuracy is typically ~ 150 μas (in the case of 2 cm delay error, and 2300 km baseline, estimated in §2). However, the higher frequency we use, the faster we should switch the target and calibrator source. Therefore, to perform realistic VLBI phase referencing observation, 43 GHz is the highest frequency at present.

We select the observing frequency at 43 GHz in order to avoid self-absorption effect as possible as we can to relate the location of radio core with that of dominant X-ray emitting blob.

1.5 Target: Blazar Markarian 501

1.5.1 General information

Mrk 501 is discovered by Markarian et al. as a part of Byurakan low dispersion spectroscopic survey (Lipovetsky et al., 1987), which selects sources with unusually strong ultraviolet continuum emission. The host galaxy of Mrk 501 is an elliptical galaxy at $z = 0.0337$ (Ulrich et al., 1975).

1.5.2 SED studies

This source is classified as TeV blazar (HBL) with its synchrotron emission peak in the ultraviolet/soft X-ray (Giommi & Padovani, 1994). Mrk 501 is one of the best known and most

prominent source among TeV blazars. It was the second source (after Mrk 421) discovered in TeV region (Quinn et al., 1996). Mrk 501 shows a large range of emitted power by one or two orders of magnitude on short timescales and intensive quasi-simultaneous broadband SED and multi-frequency correlations have been studied in the past. The SED of Mrk 501 obtained in 2009 is shown in Fig. 1.9 (Abdo et al., 2011). The VLBA core size at 43 GHz is a few times larger than the emission region in their SSC model fit (1.3×10^{17} cm). (The VERA core size at 43 GHz is several times larger than the SSC emission region.) Therefore, we expect that the VLBA & VERA 43 GHz radio core is identical to the location of X-ray emitting blobs because both emission is radiated by same electron population.

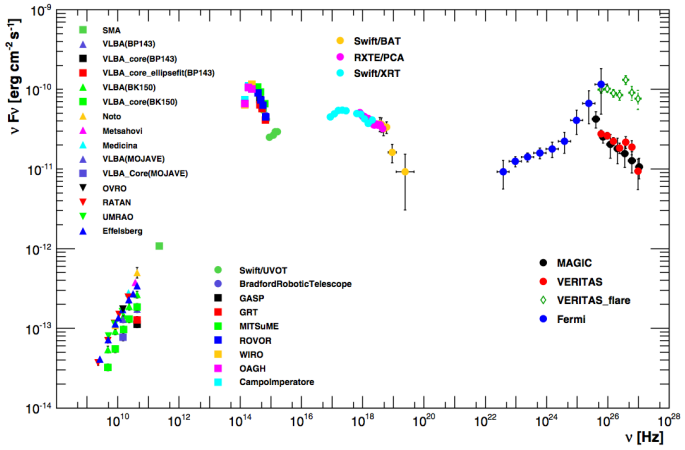

Figure 1.9: Averaged SED of Mrk 501 over the multifrequency campaign between 2009 March 15 and August 1 (Abdo et al., 2011).

1.5.3 Radio studies

In Fig. 1.10, powers of ten images of Mrk 501 is shown. On arcsec scales, Very Large Array (VLA) images show a two-sided structure oriented in position angle of $\sim 45°$ (Cassaro et al. 1999, top left in Fig. 1.10). At VLBI resolution, this source show a one-sided orthogonal to the kilo-parsec scale jet, with a clear limb-brightened structure (Piner et al. 2009, bottom middle in Fig. 1.10). The limb-bright structure also can be seen at top right image in Fig. 1.10 showing the steep spectrum in limb structure (Giroletti et al., 2004b) and at bottom right image in Fig. 1.10 showing the high polarization and perpendicular magnetic field in spine (inside the limb) structure (Piner et al., 2010). The complex limb-brightend structure makes component identification problematic and multi-epoch attempts to measure pattern speed conclude that it is not well defined (Giroletti et al., 2004b) or at most sub-luminal (Edwards & Piner, 2002). Global Millimeter VLBI Array (GMVA) image at 86 GHz in Fig. 1.10 (bottom left) probe the

innermost regions of the jet down to $\sim 200R_s$ and suggest the evidence of limb brightening on physical scales from $\lesssim 1$ pc (Giroletti et al., 2008).

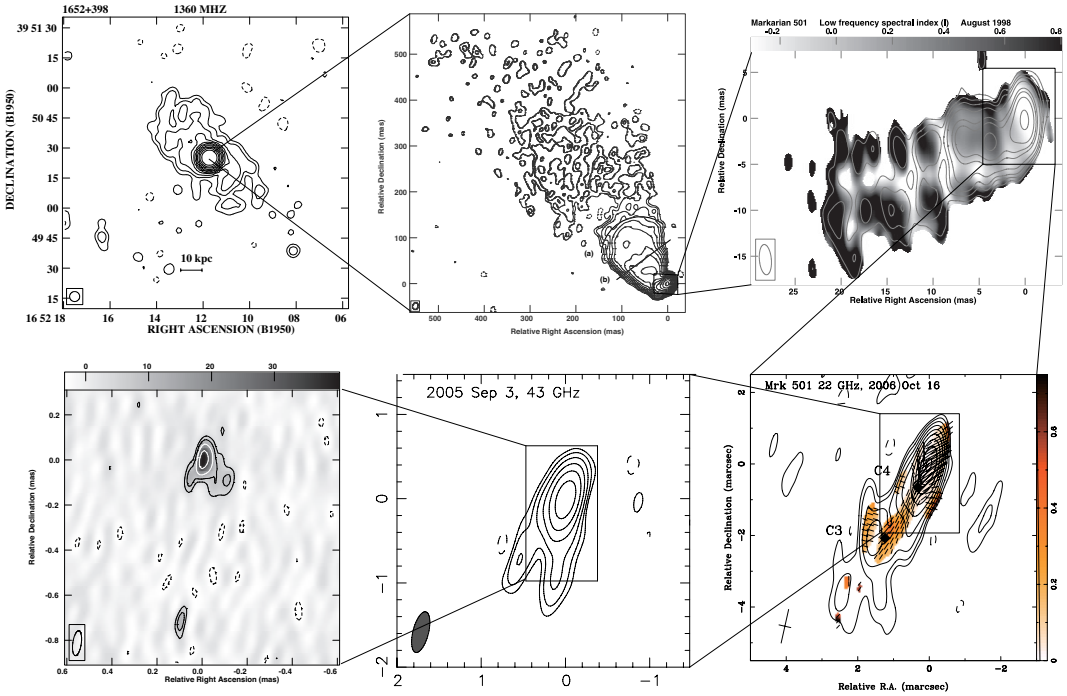

Figure 1.10: Powers of ten radio images of Mrk 501. Top left: VLA B configuration image at 1.36 GHz (Cassaro et al., 1999). Top middle: High Sensitivity Array image at 1.4 GHz on 24 November 2004 (Giroletti et al., 2008). Top right: Spectral index map between 1.6 GHz and 5 GHz with 1.6 GHz contour map, obtained by VLBI Space Observatory Programme (VSOP) on 5 and 6 March 2001. Lower right: VLBA polarization image at 22 GHz with EVPA direction tick marks and color fractional polarization (Piner et al., 2010). Lower left: VLBA image at 43 GHz on 3 September 2005 (Piner et al., 2009). Lower right: GMVA image at 86 GHz on 14 October 2005 (Giroletti et al., 2008).

1.5.4 X-rays and VHE studies

Mrk 501 went into a state of surprisingly high activity and strong variability, becoming > 10 times brighter than the Crab Nebula at energies > 1 TeV in 1997 (Catanese et al. 1997; Samuelson et al. 1998; Aharonian et al. 1999; Djannati-Atai et al., 1999). In X-ray region, the peak frequency shifted from below 1 keV to over 100 keV during the very high flux state (Pian et al., 1998), and the flaring flux increased more than ten times brighter than the usual (Tavecchio et al., 2001). In 1998-1999, the mean VHE γ-ray flux dropped by an order of magnitude, and the overall VHE spectrum softened significantly (Aharonian et al., 2001). In 2005, γ-ray flux

variability on minute timescales was observed in the VHE band, thus establishing Mrk 501 as one of the sources with the fastest γ-ray flux changes (Albert et al., 2007). This fact requires the very high Lorentz factors ($\Gamma > 50$) in the gamma-ray production region (Begelman et al., 2008). During the 2005 VHE flux variations (when Mrk 501 was three to four times dimmer than it was in 1997), significant spectral variability was detected as well, with a clear "harder when brighter" behavior. Those spectral variations are even more pronounced when compared with the spectrum measured during the low-activity level recently reported in Anderhub et al. (2009). Since 2008 Fermi Large Area Telescope (LAT) begin to monitor the sky in GeV band. During mild flux variations, remarkable spectral index variability up to one is observed and break energy around 20 GeV is found thanks to its high sensitivity (Abdo et al., 2011).

Especially by recent high time resolution of X-ray observations, the characteristic variability time scale $\sim$ 1 day is observed (e.g., Kataoka et al., 2001; Tanihata et al., 2001) and well explained by the internal shock model (Tanihata et al., 2003) (Fig. 1.11).

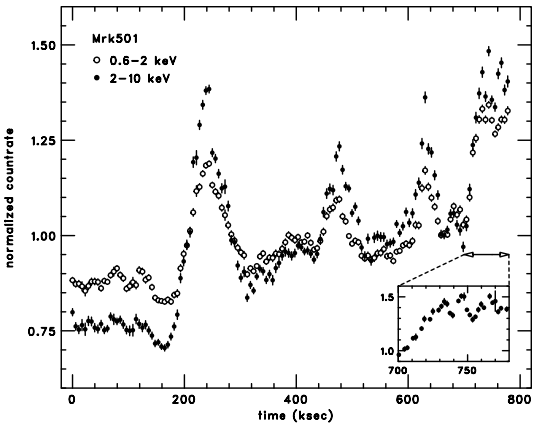

Figure 1.11: ASCA X-ray light curve of Mrk 501 during its quiescent state in 1998, taken from (Tanihata et al., 2001).

1.5.5 Merit of this source

Since Mrk 501 is one of TeV blazars, single population of relativistic electrons radiate both of radio and X-ray emission. Moreover, the VLBI core spectrum shows steep spectrum above $\sim$ 8 GHz (Fig. 1.12, Giroletti et al. 2004b), the co-location between dominant X-ray emitting blob and radio core is ensured. Additionally, the relative proximity of Mrk 501 enables us resolving into small linear scales. Especially for our phase-referencing observations, this source is the best target source because a few bright and close calibrator sources are available, while such a ideal calibrator configuration is very rare.

Throughout this paper, we adopt the following cosmological parameters : $H_0 = 71$ km s^{-1}Mpc^{-1}, $\Omega_{\rm M} = 0.27$, and $\Omega_\Lambda = 0.73$ (Komatsu et al., 2009), or 1 mas = 0.662 pc. The Schwarzschild

radius R_s for its central black hole is estimated to be 10^{-4} pc (1.4×10^{-4} mas), if we adopt $M_{\rm BH} = 10^9\ M_\odot$ (Rieger & Mannheim, 2003).

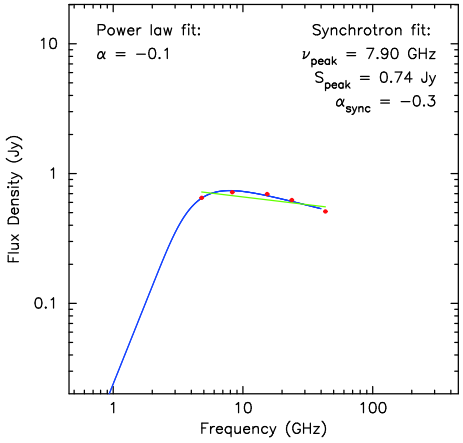

Figure 1.12: VLBI spectrum of radio core in Mrk 501. Simultaneous VLBI core spectrum shows a turnover at ∼8 GHz and the optically thin spectrum at the higher frequencies (Sokolovsky et al., 2010). The best fit synchrotron spectrum index is -0.3.

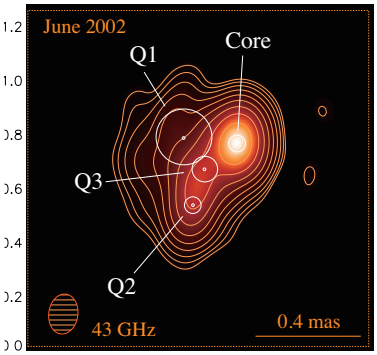

Figure 1.13: GMVA 43 GHz image of blazar NRAO 512, obtained from (Agudo et al., 2007).

1.6 Irregular Innermost Jets (Introduction to §3)

Thanks to an increasing number of detailed jet images in AGNs, irregular position angles of innermost jet features in quasars have been reported (e.g., 3C 273, Savolainen et al. 2006; 3C 345, Lobanov & Roland 2005; S5 0716+71, Bach et al. 2005; 3C 84, Dhawan et al. 1998), which do not along with lines connecting with the core and the other inner jet components. The irregular position angles typically deviate $\sim 10^\circ$ to $\sim 45^\circ$ from main jet trajectory. Some of them show position angle oscillations, believed to be triggered by changes in the direction of jet ejection nozzle (e.g. Dhawan et al., 1998). Recently, ultra-high resolution VLBI observations over 43 GHz also resolve the innermost jet orthogonal to main jet direction, and reveal that the jet components have completely different position angles from the other inner jet components in a few quasars below. In the case of NRAO 150 ($z = 1.52$), Agudo et al. (2007) show an irregular jet structure named Q1, located ∼0.13 mas (1 pc) away from the core at position angle of $\sim 60^\circ$ from Q2 component (Fig. 1.13). These inner jet features also show an extreme projected counter-clockwise jet position angle swing at an angular rate of up to $\sim 11^\circ$/year. Agudo et al. (2011a) also resolve the innermost jet in OJ 287 ($z = 0.306$), which is located at position angle of $\sim 90^\circ$ from past jet direction. The most recent result is the case of 1924−292

($z = 0.352$), and 3C 279 ($z = 0.536$) obtained by Event Horizon Telescope at 230 GHz (Lu et al., 2012, 2013). The inner jet Mc1 makes a position angle difference of $\sim 80^\circ$ with respect to the centimeter jet.

On the other hand, the innermost jets of BL Lac Objects are not studied well. Mrk 501 is the best target to resolve the innermost jet because of its proximity. Although VLBA 43 GHz images of Mrk 501 have been reported so far (Piner et al., 2009, 2010), the irregular position angle of the innermost jet was not found. Giroletti et al. (2008) show the inner 0.1 mas (0.07 pc) jet limbs have opening angle at $\sim 90^\circ$ by using Global Millimeter VLBI Array 86 GHz. This time we report the innermost jet feature of Mrk 501 by using both archival and our data at VLBA 43 GHz.

Chapter 2

Position Measurements of Radio Core in Mrk 501

In order to measure the spatial distribution scale of X-ray emitting blobs directly with high positional accuracy, we proposed and performed multi-epoch astrometric observations toward blazar Mrk 501 to the common use of VERA and VLBA at 43 GHz. In this chapter, we show our VERA observations in §2.1, the results in §2.2, our VLBA observations §2.3, and their results in §2.4.

2.1 Observations and Data Reduction of VERA Data

We conducted two phase-referencing observations over successive four-days in February and October, 2011. VERA is one of Japanese VLBI array consisted of four elements (Fig. 2.1), aiming at Galactic maser astrometry.

2.1.1 Observations and data reductions

The VERA observations were carried out 8 epochs over successive four days at 8 months intervals. The observations (proposal code : VERA 10-64) were conducted on 2011 February 15, 16, 17, 18, and 2011 October 20, 21, 23, 24. Observing date and each observing condition is summarized in Table 2.1. Each observation time was 8 hours. In order to determine the radio core positions of Mrk 501, we observed three sources (one target and two calibrators) simultaneously in the dual-beam mode of VERA for phase referencing (e.g., Honma et al., 2003).

The real-time instrumental phase difference data between the two beams were taken with an artificial noise source in each beam (Kawaguchi et al., 2000; Honma et al., 2008). Left hand circular polarization (LHCP) signals were digitized with 2-bit quantization, filtered using the VERA digital filter (Iguchi et al., 2005), and recorded with a rate of 1024 Mbps. Source configurations, dual-beam allocations, and VERA images of our observations are shown in Fig. 2.2. In the total bandwidth of 256 MHz (16 $\times$ 16 MHz), one of the sixteen 16-MHz

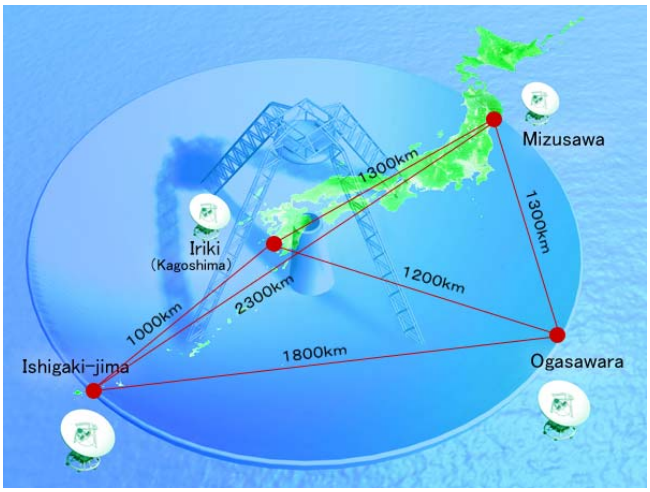

Figure 2.1: VERA array consists of 4 stations located at Mizusawa, Iriki, Ogasawara, Ishigaki-jima. The maximum baseline is 2300 km and each dish is 20 meters in diameter. Image Credit: NAOJ.

Table 2.1: Summary of VERA 43 GHz Phase-referencing Observations

Epoch	time range	Code	bad weather
2011/02/15	18:18-02:18	R11046B	OGA: 0:30-1:20 & 2:15-, IRK: 0:50-1:40
2011/02/16	18:14-02:14	R11047B	IRK: all time, OGA: 22:00-22:40
2011/02/17	18:10-02:10	R11048B	
2011/02/18	18:06-02:06	R11049B	IRK: all time, OGA: 23:40-23:58 & 00:45-1:07
2011/10/20	01:50-09:50	R11293A	OGA: -06:00, IRK: 06:00-
2011/10/21	01:46-09:46	R11294A	
2011/10/23	01:38-09:38	R11296A	ISH: -06:30, 05:30-07:00 (lack of visibility)
2011/10/24	01:34-09:34	R11297A	

Notes. −MIZ: Mizusawa, IRK: Iriki, OGA: Ogasawara, ISH: Ishigaki. MIZ has elevetion limit over ∼50 min in every observations.

IF channels was assigned to the bright calibrator, quasar 3C 345. The other 15 IF channels were allocated to the target Mrk 501, and another calibrator NRAO 512. Simultaneous phase-referencing is conducted between 3C 345 and Mrk 501 with 2.09° separation, and between 3C 345 and NRAO 512 with 0.49° separation, because the upper limit of the dual-beam separation is 2.2°. Typical uv-coverage of each source is shown in Fig. 2.3.

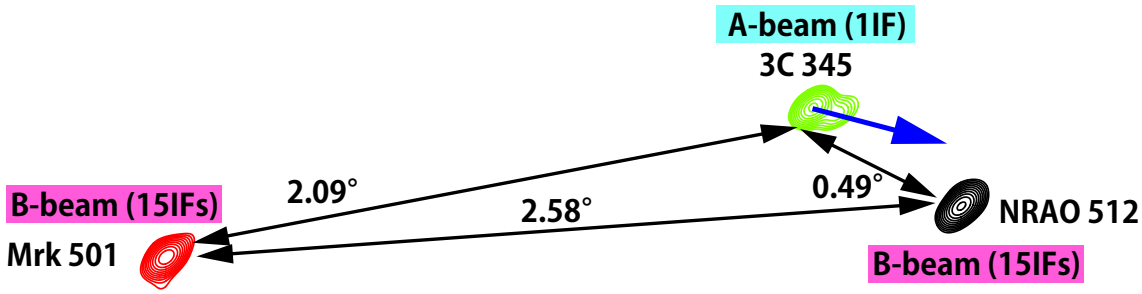

Figure 2.2: Source configurations, dual-beam allocations, and self-calibrated images of VERA observations. The target Mrk 501 is located near two bright calibrators, 3C 345 and NRAO 512. Their separation angles are written in. As explained in the AIPS memo 111, this is one of the configuration for multi-calibrator phase referencing. Self-calibration images of each sources obtained by VERA in Fig. 2.7 (a), (b), (c) are shown as red, green, black contours, respectively. Blue arrow shows the jet direction of 3C 345. With VERA resolution, Mrk 501 and NRAO 512 are almost point source.

We used the Astronomical Image Processing System (AIPS) software package developed by the NRAO for a priori amplitude calibration, fringe fitting, and passband calibration process. At first, the cross-correlation visibilities are normalized by the auto-correlation with AIPS task ACCOR. A-priori amplitude calibration was performed with the AIPS task APCAL on the basis of the measurement of the system temperatures by the R-Sky method during the observations and the antenna gain information for each antenna provide in the VERA Status Report in 2009. We use the antenna gain including the separation angle dependency of two-beam observation mode. We did not apply the opacity correction in the task APCAL since the provided system temperature was corrected the atmospheric absorption. Errors on the amplitude calibration are ∼10% (Nagai et al., 2013; Orienti et al., 2012).

To obtain the phase-referenced positions of radio core in Mrk 501, firstly we derive the phase-referenced peak positions of Mrk 501 referred to 3C 345, and then subtract the phase referenced peak positions of NRAO 512 referred to 3C 345, since the radio core positions of 3C 345 could be shift ∼ 20-500 μas per year due to identification error of radio core, measured below 10 GHz (Shapiro et al., 1979; Marcaide & Shapiro, 1984; Bartel et al., 1986; Doi et al., 2006). The flow chart of our data reduction and reduction parameters are summarized in Appendix B.

Firstly we construct self-calibrated images of all the sources to obtain the structure phase and amplitude solutions. Fringe fitting was done using the AIPS task FRING over 30 seconds

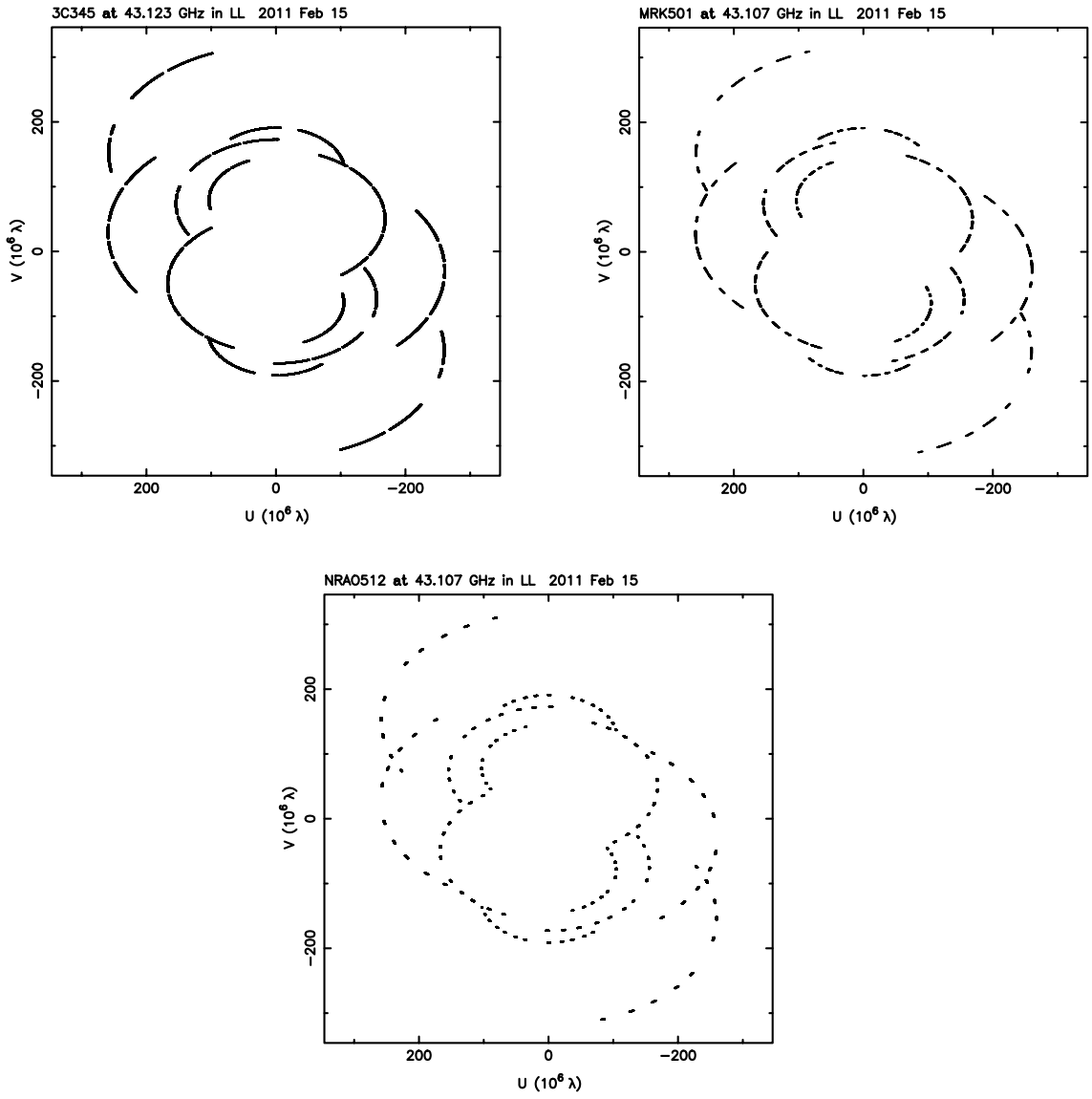

Figure 2.3: Typical uv-coverage of VERA observations. The top left image is the uv-coverage of 3C 345, the top right image is that of Mrk 501, and the bottom image is that of NRAO 512, obtained on 15th February 2011.

solution intervals for 3C 345 and NRAO 512, to determine delay and phase rate calibration to be applied to a uv data set assuming a point source model. After careful flagging of bad data and averaging $\sim$ 5 seconds in the time domain and over a passband, we combined the visibilities over successive four-days observation data into one data set by AIPS task DBCON to construct calibrator initial structure model by using modelfit and self-calibration algorithm. Imaging was performed by visibility based model fitting and self-calibration iteratively in the Difmap software package (Shepherd, 1997). For Mrk 501, this source does not have enough flux for VERA to perform fringe fitting, such that after applying fringe phase of 3C 345 to Mrk 501, we performed self-calibration of Mrk 501.

Secondly, to obtain the phase-referenced images of Mrk 501, we transferred the derived fringe solutions and its structure phase to both NRAO 512 and Mrk 501. By applying the amplitude solution of NRAO 512 and Mrk 501 to their own visibility, we obtain the phase-referenced images of NRAO 512 and Mrk 501. Peak positions of each phase-referenced images are measured by AIPS task JMFIT. Finally, we subtract the phase-referenced peak position of NRAO 512 referred to 3C 345, from the phase-reference peak position of Mrk 501 referred to 3C 345 to avoid the core position shift of 3C 345, then obtain the phase-referenced positions of Mrk 501 referred to point source NRAO 512.

2.1.2 Estimation of position errors for each phase-referencing pair

In order to determine the spatial distribution scale of dominant X-ray emission blobs, the phase-referenced core peak positions of Mrk 501 should be measured with proper error budgets. The major sources of errors in core peak position measurement come from the uncertainties of dispersive ionospheric residuals, non-dispersive tropospheric residuals, core identification process, instrumental errors, and geometrical parameters (earth orientation parameters, antenna positions and a priori source coordinates). However, our observations can reduce three of these errors because of the following advantages: (i) ionospheric effects are close to zero because the observing frequency is at 43 GHz (estimated below). (ii) since Mrk 501 and NRAO 512 are nearly a point like with the beamsize of VERA ($\sim 0.6 \times 0.4$ mas), the core identification process which come from the source structures can be neglected. Identification error which would come from the prominent jet structure of 3C 345 can be eliminated by subtracting the phase-referenced peak position of NRAO 512 referring to 3C 345, from the phase-reference peak position of Mrk 501 referring to 3C 345. (iii) We assume that the instrumental errors, typically a phase drift of less than 6° hr^{-1} at 43 GHz (Kawaguchi et al., 2000), affect both the target and the calibrator equally by applying the dual-beam calibration table provided by VERA.

We summarize the estimated error budget for each phase-referencing pair in our observations in Table 2.2. We consider these sources of errors contribute independently to each other, such that the total errors at each epoch can be obtained as the root-sum-square of them. Below details are described on the estimation for major error sources.

Random

The positional accuracy due to the random errors is described as $\theta_{\rm b}/(2 \times SNR)$, where θ_b is the interferometric beam size $\sim$0.6 mas and SNR is the signal-to-noise ratio of the phase-referenced image in Column (4) of Table 2.5, 2.6, and 2.7 for our observation.

Propagation delay

Propagation delays are mainly caused by the ionospheric and tropospheric medium. The effects of an unmodeled ionosphere and the troposphere fall into image distortion and image shift. The image distortion causes a decrease in the dynamic range of the phase-referenced images and its contribution is estimated in the image quality together with the other random errors. The image shift introduces an unknown position offset. The positional error $\delta\theta$ originated from the phase error $\Delta\phi$ is (e.g. Thompson et al., 2001)

$$\delta\theta = \frac{\Delta\phi}{2\pi D_\lambda},$$

where $D_\lambda \sim D \cdot \lambda^{-1}$, D is baseline length, and λ is the observing wavelength. $\Delta\phi$ is estimated by $2\pi c \Delta\tau \lambda^{-1}$, where $\Delta\tau$ is the propagation delay error and c is the speed of light. $\Delta\tau$ can be approximated by $\delta\tau_0$ sec$Z$, where $\delta\tau_0$ is the residual vertical delay and Z is the local source zenith angle. When measuring the difference in position of two sources separated in zenith angle by ΔZ, a first-order Taylor expansion of τ yield the expected differenced phase delay error for a single antenna (Reid et al., 1999):

$$\Delta\tau \sim \frac{\partial\tau}{\partial Z}\ \Delta Z = \delta\tau_0 \sec Z \tan Z\ \Delta Z.$$

Thus, the positional error $\delta\theta$ can be expressed as follows:

$$\delta\theta \sim \frac{c\delta\tau_0}{D} \sec Z \tan Z\ \Delta Z. \tag{2.1}$$

Z in degree, δZ is source separation angle in radian, and D is baseline length in m.

Ionosphere

Propagation delays due to dispersive ionospheric medium introduce frequency dependent errors which should be proportional to ν^{-2}. The residual ionospheric zenith delay is $\delta\tau_{0;\rm ion} = 40.3\ \delta I/\nu^2$, with residual total electron content δI in m^{-2} and ν in Hz (Thompson et al., 2001). During our VERA observations, we estimate $I \sim 1 \times 10^{17}$ m^{-2} over the sky of VERA stations by using GPS data provided by NASA. Global ionospheric model based on GPS satellites have an accuracy of about 10 $\sim$ 25% (Mannucci et al. 1998). Adopting the uncertainty of 25%, δI corresponds to $\sim 2.5 \times 10^{16}$ m^{-2} and the zenith-angle-averaged values result in < 1 μas at 43 GHz for VERA's maximum baseline $D = 2.3 \times 10^3$ m and $\Delta Z = 2.09°$.

Troposphere

The non-dispersive tropospheric medium causes propagation delays which are independent of observing frequency. Therefore, positional error caused by the residual tropospheric delay is independent of observing frequency. Positional accuracies at higher frequency ($\geq$8.4 GHz) are generally dominated by an inaccurate tropospheric zenith delay at each antenna in a correlator model. Similarly to the ionosphere, these residuals also contribute to the image distortion and the image shift. Adopting a typical $\sim$2 cm misestimation of the zenith delay for the model used by the VERA correlator (Honma et al., 2008), this introduces the shift of the absolute position up to $\sim$ 122 μas for $\delta Z = 2.09^\circ$ (Mrk 501-3C 345 pair), and $\sim$ 28 μas for $\delta Z = 0.49^\circ$ (NRAO 512-3C 345 pair) at 43 GHz and $Z \sim 50^\circ$ with $D = 2.3 \times 10^3$ m.

Table 2.2: Estimated positional error budgets in the phase-referencing observation by VERA 43 GHz toward Mrk 501, referencing to calibrator 3C 345. The units are in μas.

Epoch	$\sigma_{\rm random}$		$\sigma_{\rm trop}$	$\sigma_{\rm ion}$	$\sigma_{\rm earth}$		$\sigma_{\rm ant}$		$\sigma_{\rm coord}$		$\sigma_{\rm rss}$	
	x	y			x	y	x	y	x	y	x	y
(1)	(2)	(3)	(4)	(5)	(6)	(7)	(8)	(9)	(10)	(11)	(12)	(13)
2011/02/15	27	26	122	< 1	3	5	1	5	2	3	125	125
2011/02/16	16	16	122	< 1	3	5	1	5	2	3	123	124
2011/02/17	56	61	122	< 1	3	5	1	5	2	3	134	136
2011/02/18	27	26	122	< 1	3	5	1	5	2	3	125	125
2011/10/20	13	15	122	< 1	3	5	1	5	2	3	123	123
2011/10/21	23	28	122	< 1	3	5	1	5	2	3	124	125
2011/10/23	16	21	122	< 1	3	5	1	5	2	3	123	124
2011/10/24	16	16	122	< 1	3	5	1	5	2	3	123	123

Notes.$-$(1) Observing epoch, (2) random error estimated by beamwidth over 2 times signal-to-noise ratio in the direction of right ascension, (3) in the direction of declination, (4) tropospheric residual errors, (5) ionospheric residual errors, (6) earth orientation parameter error in the direction of right ascension, (7) in declination, (8) antenna position error in the direction of right ascension, (9) in declination, (10) apriori source coordinates error in the direction of right ascension, (11) in declination, cause the positional error of phase-referenced image. The error contributions from the geometrical errors (6)-(11) are estimated based on the simulation presented in Pradel et al. (2006). Total error in right ascension (12) and in declination (13) is estimated as the root-sum-square of each error.

Table 2.3: Estimated positional error budgets in the phase-referencing observation by VERA 43 GHz toward NRAO 512, referencing to calibrator 3C 345. The units are in μas.

Epoch	$\sigma_{\rm random}$		$\sigma_{\rm trop}$	$\sigma_{\rm ion}$	$\sigma_{\rm earth}$		$\sigma_{\rm ant}$		$\sigma_{\rm coord}$		$\sigma_{\rm rss}$	
	x	y			x	y	x	y	x	y	x	y
(1)	(2)	(3)	(4)	(5)	(6)	(7)	(8)	(9)	(10)	(11)	(12)	(13)
2011/02/15	18	16	28	< 1	3	5	1	5	2	3	33	33
2011/02/16	17	17	28	< 1	3	5	1	5	2	3	33	34
2011/02/17	64	70	28	< 1	3	5	1	5	2	3	70	76
2011/02/18	15	14	28	< 1	3	5	1	5	2	3	32	32
2011/10/20	17	18	28	< 1	3	5	1	5	2	3	33	34
2011/10/21	22	29	28	< 1	3	5	1	5	2	3	36	41
2011/10/23	21	24	28	< 1	3	5	1	5	2	3	35	38
2011/10/24	18	20	28	< 1	3	5	1	5	2	3	34	35

Notes.−Same as Table 2.2.

Table 2.4: Estimated positional error budgets in the phase-referencing observation by VERA 43 GHz toward 3C 345, referencing to calibrator NRAO 512. The units are in μas.

Epoch	$\sigma_{\rm random}$		$\sigma_{\rm trop}$	$\sigma_{\rm ion}$	$\sigma_{\rm earth}$		$\sigma_{\rm ant}$		$\sigma_{\rm coord}$		$\sigma_{\rm rss}$	
	x	y			x	y	x	y	x	y	x	y
(1)	(2)	(3)	(4)	(5)	(6)	(7)	(8)	(9)	(10)	(11)	(12)	(13)
2011/02/15	17	16	28	< 1	3	5	1	5	2	3	33	33
2011/02/16	15	18	28	< 1	3	5	1	5	2	3	32	33
2011/02/17	86	95	28	< 1	3	5	1	5	2	3	91	90
2011/02/18	11	11	28	< 1	3	5	1	5	2	3	30	31
2011/10/20	15	14	28	< 1	3	5	1	5	2	3	32	32
2011/10/21	19	22	28	< 1	3	5	1	5	2	3	34	37
2011/10/23	15	18	28	< 1	3	5	1	5	2	3	32	34
2011/10/24	18	20	28	< 1	3	5	1	5	2	3	33	38

Notes.−Same as Table 2.2.

2.2 VERA Results

2.2.1 VERA images

Phase-referenced images of Mrk 501 referring to 3C 345, NRAO 512 referring to 3C 345, and 3C 345 referring to NRAO 512 for all epochs are summarized in Fig. 2.4, 2.5, 2.6, respectively. The image performances are summarized in Column (1), (2), (3), (4) of Table 2.5, 2.6, 2.7. We detect all sources with image SNR more than 9 except for the observation on 17th February 2011, which observation is affected by bad weather. We also confirmed the self-calibration image of all three observed sources shown in Fig. 2.7 and summarized their image performances in Table 2.8. From Fig. 2.7, NRAO 512 and Mrk 501 are nearly point source, while 3C 345 is resolved into two or three bright components by VERA 43 GHz. Compared to a self-calibrated image of 3C 345 with VERA 43 GHz obtained by Jung et al. (2011) in 2005 April, our self-calibrated images of 3C 345 does not show any extended structures. The differences are due to source structure and flux change in different observing epoch, and different observation sensitivities. For the observation in 2005 April, 128 MHz bandwidth is allocated to 3C 345, however, for our observations, only 16 MHz is allocated. As a confirmation of our flux calibration accuracy, we checked VLBA 43GHz archival data within one month error and found the restored peak flux of 3C 345 is consistent with our peak flux in Table.2.8 within 10%.

2.2.2 Core peak position of single epoch observation

In Fig. 2.8 and 2.9, the phase-referenced core peak positions of NRAO 512 and Mrk 501, referencing to 3C 345, are plotted respectively. The peak positions and their position error are summarized in Table 2.6 and 2.5. We estimate the position error of each epoch between each phase-referencing pair as the root-sum-square of all the error sources estimated in previous section because we consider all the sources of errors contribute independently to each other. From Fig. 2.8 and 2.9, each phase-referenced core peak position (without error) during successive four-days observations are consistent within ~ 90 μas both in Right Ascension and in Declination. As a confirmation of our phase-referencing observations, we made phase-referenced image of 3C 345 referencing to NRAO 512, and summarized the core peak positions in Table 2.7. The phase-referenced peak positions of 3C 345 are consistent with inverse phase-referenced peak positions of NRAO 512 in RA and Dec (Table 2.6) within ~ 40 μas except for 2011 February 17.

From Fig. 2.9, ~ 0.1 mas position difference between the successive four-days observations in 2011 February (blue squares) and October (red squares) can be seen, which would reflect the peak position change of 3C 345, because NRAO 512 is nearly point source by VERA. The phase-reference position of Mrk 501 referencing to 3C 345 in Fig. 2.8 would include the core position changes of both sources. To extract the radio core positions of Mrk 501, we remove the possible position changes of 3C 345 by subtracting the core positions of NRAO 512 referencing to 3C 345 from the core positions of Mrk 501 referencing to 3C 345. As a result, we obtain the

plot of core peak position of Mrk 501 relative to NRAO 512 in Fig. 2.10, assuming the core peak position of NRAO 512 is stationary. The position error of Mrk 501 relative to NRAO 512 is estimated by summing the root sum square of random error and all the other systematic error between the position error of Mrk 501-3C 345 and that of NRAO 512-3C 345. The core peak positions of Mrk 501 relative to NRAO 512 for successive four epochs do not move both in RA and in Dec with $> 98\%$ probability within a χ^2/ndf of 0.14/3. Therefore, we discuss weighted-mean core peak position of Mrk 501 with position error of single epoch, since no significant motion of the core peak was detected.

2.2.3 Core peak positions of successive four-days observations

In order to determine the core peak positions of Mrk 501 with high accuracy, we discuss the averaged core peak position of Mrk 501 referencing to core peak position of NRAO 512, weighted by single epoch position error in Fig. 2.11, assuming the core peak position is stationary during successive four-days observations. The positional accuracy of successive four-days as one observation is estimated to be $\sim$ 110 μas by using positional accuracy over root of successive observation number, and summarized in Table 2.10. Therefore, the spatial distribution scale of averaged radio core peak positions in February and October 2011 is estimated to be $(61 \pm 142, 65 \pm 151)$ μas in RA and Dec.

We further discuss the core peak positions of Mrk 501 along its jet axis. In Fig. 2.12, we plotted the projected averaged phase-referenced core peak positions of Mrk 501 along jet position angle $\sim 158^\circ$, which is the averaged position angle of extended jet components C3 and C4 in Table 3.2. The spatial distribution scale of Mrk 501's core peak positions referred to NRAO 512 along jet axis in 2011 February and October is 83 $\pm$ 140 μas, and the positions are consistent with 66% probability. Therefore, the phase-referenced core peak positions of Mrk 501 referencing to NRAO 512 lie within 220 μas along its jet direction. Using inner jet viewing angle $\sim$ 4 deg (Giroletti et al., 2004b), the core peak positions of Mrk 501 along the jet direction lie within de-projected 2.1 pc between February and October 2011.

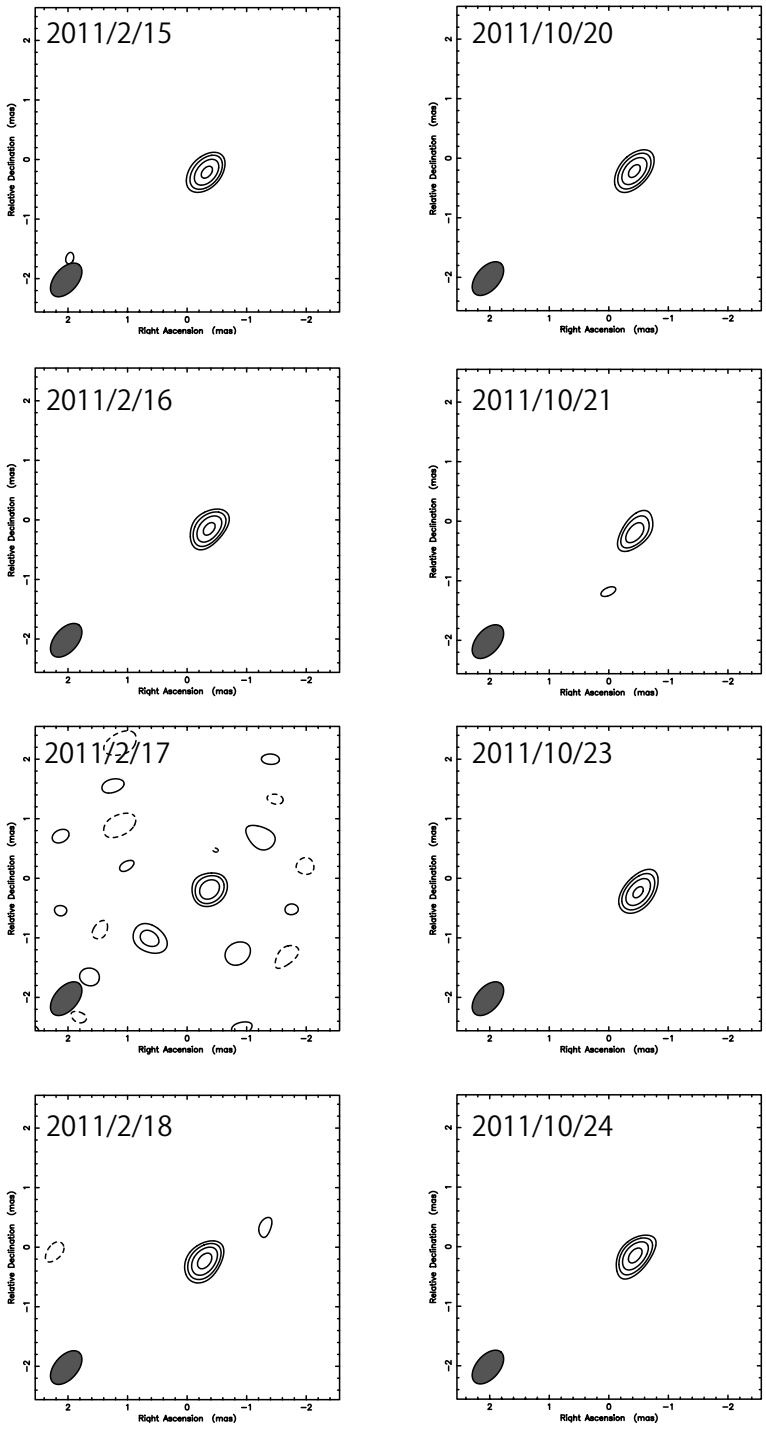

Figure 2.4: Phase-referenced images of Mrk 501 by VERA 43 GHz. Reference calibrator is 3C 345. The restored beam size is 0.669 mas × 0.391 mas at a position angle at $-40.9°$ and the contour start from three times 28.0 mJy beam^{-1}.

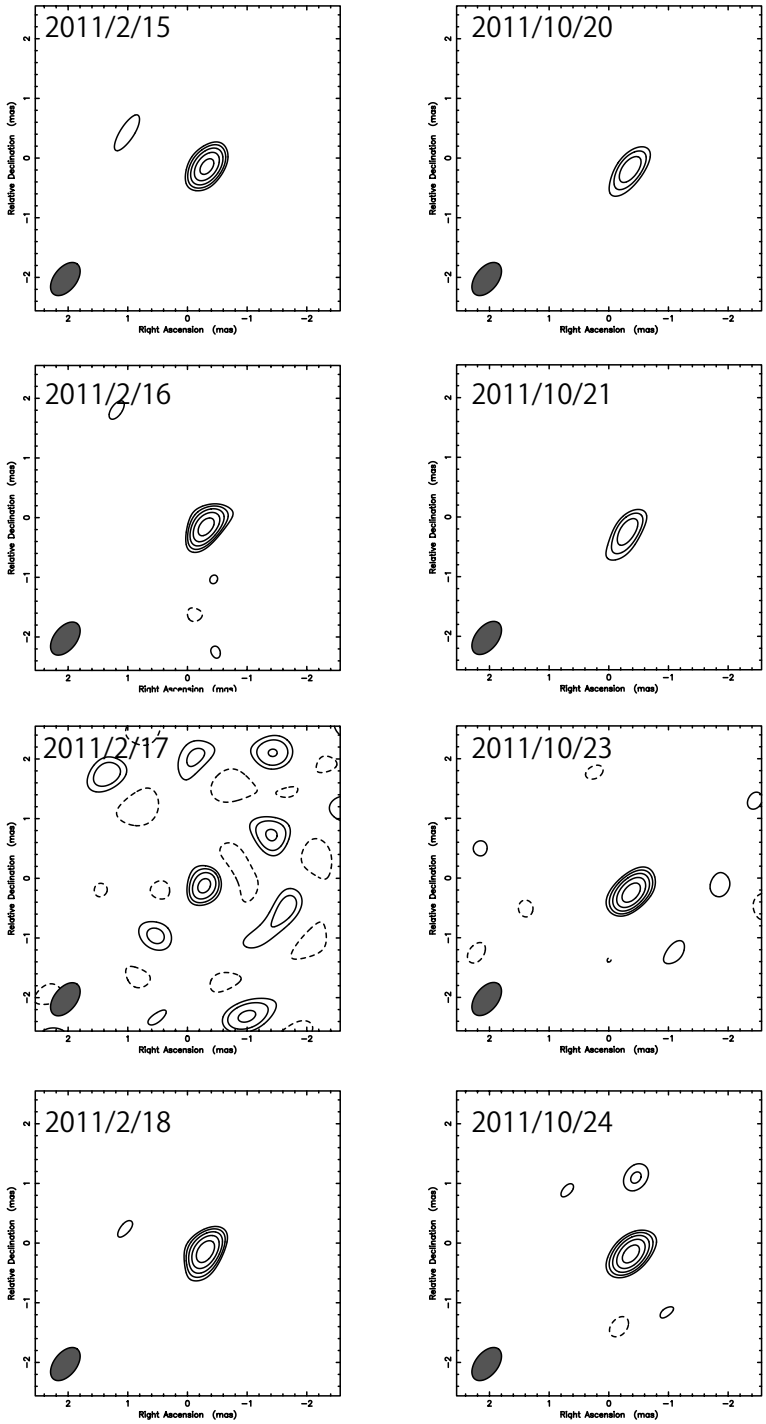

Figure 2.5: Phase-referenced images of NRAO 512 by VERA 43 GHz. Reference calibrator is 3C 345. The restored beam size is 0.642 mas × 0.379 mas at a position angle at −38.3° and the contour start from three times 28.0 mJy beam^{-1}.

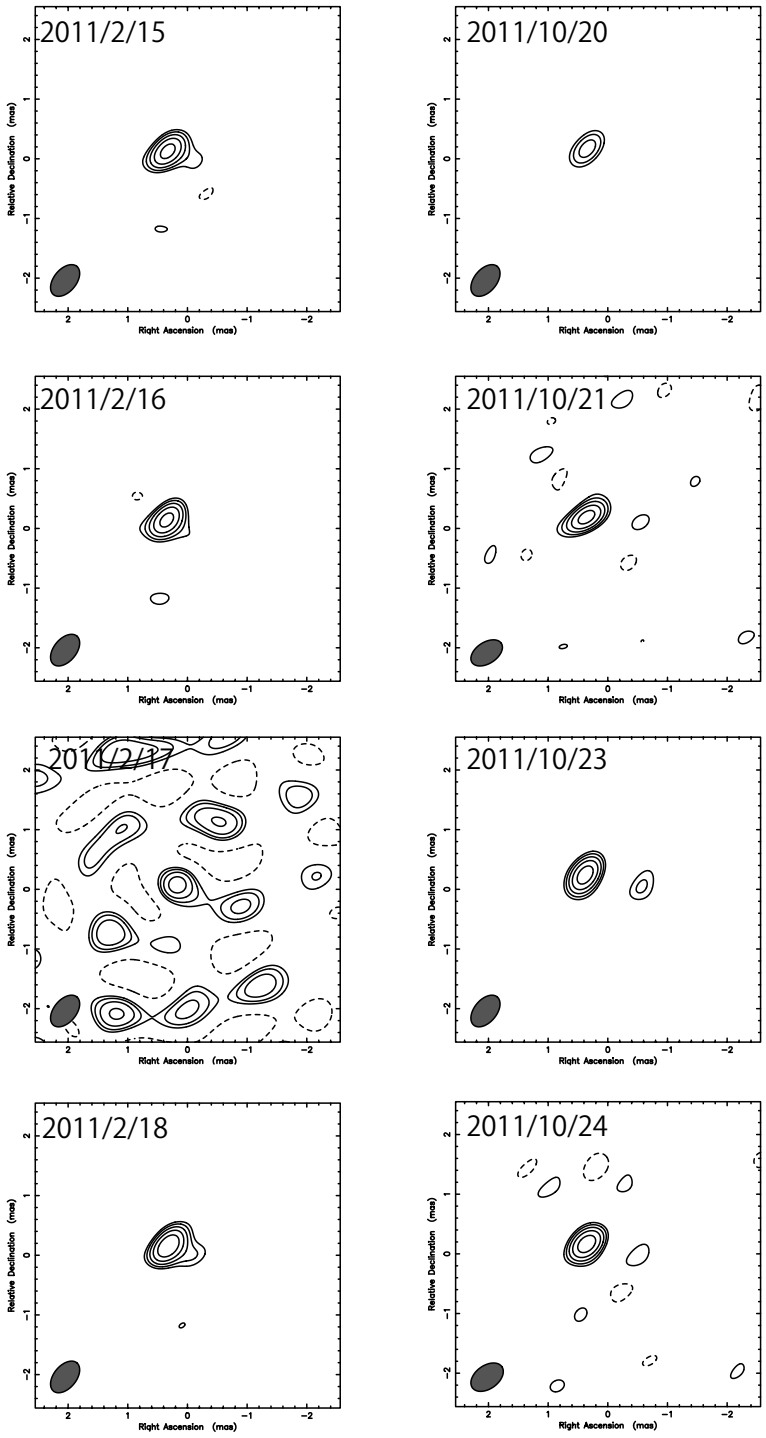

Figure 2.6: Phase-referenced images of 3C 345 by VERA 43 GHz. Reference calibrator is NRAO 512. The restored beam size is 0.615 mas × 0.377 mas at a position angle at −39.7° and the contour start from three times 112 mJy beam^{-1}.

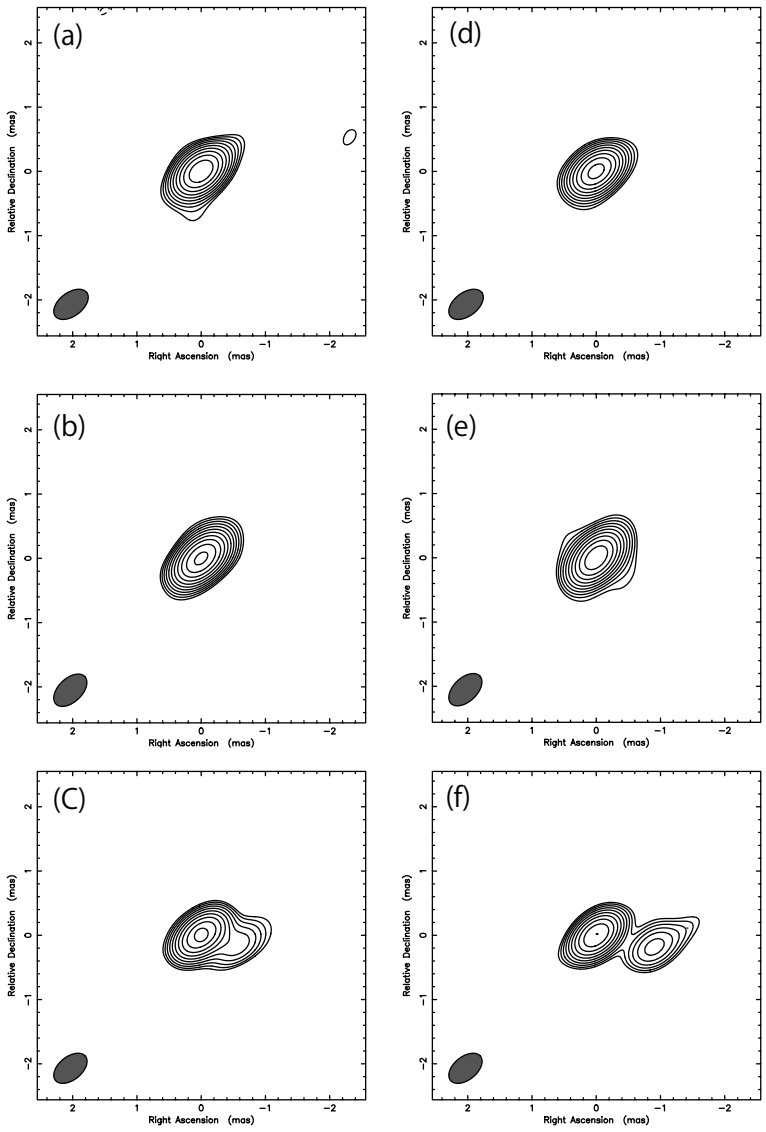

Figure 2.7: Self-calibrated images of all sources by VERA 43 GHz. (a), (b), (*c*) are imaged by combining uv data sets of 2011 February 15, 16, 17, 18 and (d), (e), (f) are 2011 October 20, 21, 23, 24. The upper panel shows self-cal images of Mrk 501 with restored beam size of 0.613 mas $\times$ 0.366 mas at a position angle at $-53°$. Contours start from three times 3.04 mJy beam^{-1}. The middle panel shows self-cal images of NRAO 512 with restored beam size of 0.621 mas $\times$ 0.368 mas at a position angle at $-46.4°$. Contours start from three times 5.15 mJy beam^{-1}. The bottom image is self-cal images of 3C 345 with restored beam size of 0.600 mas $\times$ 0.361 mas at a position angle at $-51.1°$. Contours start from three times 30.0 mJy beam^{-1}. The beam size and contour level of each images are aligned to that of (a), (b), (*c*).

Table 2.5: VERA phase-referenced image qualities of Mrk 501, referencing to 3C 345.

Epoch	$I_{\rm p}$ (Jy beam^{-1})	$\sigma_{\rm rms}$ (Jy beam^{-1})	$I_{\rm p}/\sigma_{\rm rms}$	$\Delta\alpha$ (mas)	$\Delta\delta$ (mas)
(1)	(2)	(3)	(4)	(5)	(6)
2011/02/15	259	29.1	9	-0.332 ± 0.125	-0.211 ± 0.125
2011/02/16	262	21.0	12	-0.371 ± 0.123	-0.148 ± 0.124
2011/02/17	224	44.9	5	-0.377 ± 0.134	-0.184 ± 0.136
2011/02/18	275	30.8	9	-0.296 ± 0.125	-0.229 ± 0.125
2011/10/20	262	15.5	17	-0.429 ± 0.123	-0.213 ± 0.123
2011/10/21	210	24.4	9	-0.439 ± 0.124	-0.194 ± 0.125
2011/10/23	254	18.5	14	-0.494 ± 0.123	-0.234± 0.124
2011/10/24	270	18.4	15	-0.443 ± 0.123	-0.146 ± 0.123

Notes.−(1) Observing epoch, (2) peak intensity, (3) rms of image noise, (4) image dynamic range, (5) and (6) position shift from phase-tracking center of Mrk 501, measured by two-dimensional gaussian fitting using task JMFIT in AIPS minus each core identification error.

Table 2.6: VERA phase-referenced image qualities of NRAO 512, referencing to 3C 345.

Epoch	$I_{\rm p}$ (Jy beam^{-1})	$\sigma_{\rm rms}$ (Jy beam^{-1})	$I_{\rm p}/\sigma_{\rm rms}$	$\Delta\alpha$ (mas)	$\Delta\delta$ (mas)
(1)	(2)	(3)	(4)	(5)	(6)
2011/02/15	388	28.5	14	-0.326 ± 0.033	-0.142 ± 0.033
2011/02/16	408	32.2	13	-0.312 ± 0.033	-0.152 ± 0.034
2011/02/17	272	61.6	4	-0.280 ± 0.070	-0.124 ± 0.076
2011/02/18	438	27.5	16	-0.301 ± 0.032	-0.139 ± 0.032
2011/10/20	228	17.4	13	-0.360 ± 0.033	-0.184 ± 0.034
2011/10/21	222	25.2	9	-0.319 ± 0.036	-0.229 ± 0.041
2011/10/23	424	38.4	11	-0.376 ± 0.035	-0.244 ± 0.038
2011/10/24	410	32.5	13	-0.371 ± 0.034	-0.182 ± 0.035

Notes.−(1) Observing epoch, (2) peak intensity, (3) rms of image noise, (4) image dynamic range, (5) and (6) position shifts from phase-tracking center of NRAO 512, measured by two-dimensional gaussian fitting using task JMFIT in AIPS minus core identification error.

Table 2.7: VERA phase-referenced image qualities of 3C 345, referencing to NRAO 512.

Epoch	$I_{\rm p}$ (Jy beam^{-1})	$\sigma_{\rm rms}$ (Jy beam^{-1})	$I_{\rm p}/\sigma_{\rm rms}$	$\Delta\alpha$ (mas)	$\Delta\delta$ (mas)
(1)	(2)	(3)	(4)	(5)	(6)
2011/02/15	1.57	113	14	0.332 ± 0.033	0.138 ± 0.033
2011/02/16	1.55	113	14	0.349 ± 0.032	0.153 ± 0.033
2011/02/17	1.23	376	3	0.151 ± 0.091	0.076 ± 0.090
2011/02/18	1.89	95.1	20	0.321 ± 0.030	0.165 ± 0.031
2011/10/20	0.82	54.5	15	0.342 ± 0.032	0.170 ± 0.032
2011/10/21	1.60	149	11	0.356 ± 0.034	0.188 ± 0.037
2011/10/23	1.67	115	14	0.381 ± 0.032	0.238 ± 0.034
2011/10/24	1.71	140	12	0.354 ± 0.033	0.165 ± 0.038

Notes.−(1) Observing epoch, (2) peak intensity, (3) rms of image noise, (4) image dynamic range, (5) and (6) position shifts from phase-tracking center of 3C 345, measured by two-dimensional gaussian fitting using task JMFIT in AIPS minus core identification error.

Table 2.8: Self-calibrated image performances of NRAO 512, Mrk 501, and 3C 345 by VERA.

Source	Epoch	$I_{\rm p}$ (Jy beam^{-1})	$\sigma_{\rm rms}$ (Jy beam^{-1})	$I_{\rm p}/\sigma_{\rm rms}$
	(1)	(2)	(3)	(4)
NRAO 512	2011/02	467	5.15	92
	2011/10	542	1.94	278
Mrk 501	2011/02	279	3.04	92
	2011/10	239	1.78	134
3C 345	2011/02	2.21	30.0	74
	2011/10	2.04	17.0	120

Notes.−(1) Observing epoch, (2) peak intensity, (3) rms of image noise, (4) image dynamic range.

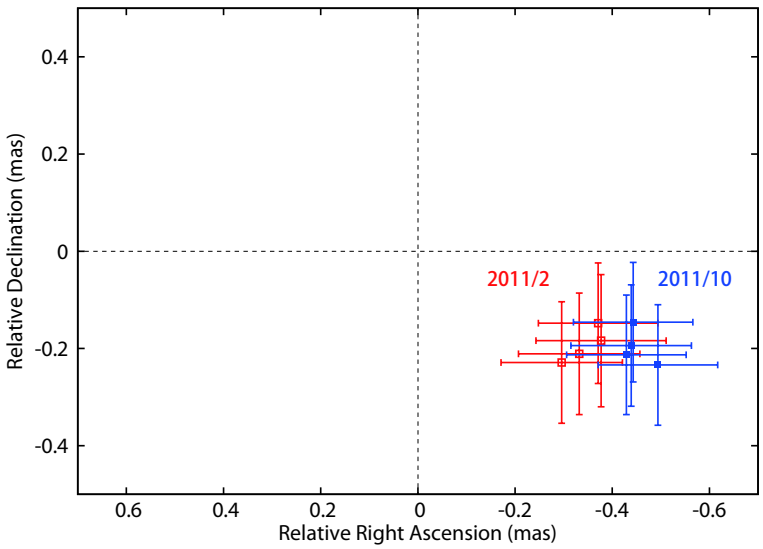

Figure 2.8: Phase-referenced core peak positions of Mrk 501 relative to core peak positions of 3C 345. Red blank squares represents the data obtained in 2011 February and blue filled squares represents the data obtained in 2011 October. The value of each peak position and its error is summarized in Table 2.5.

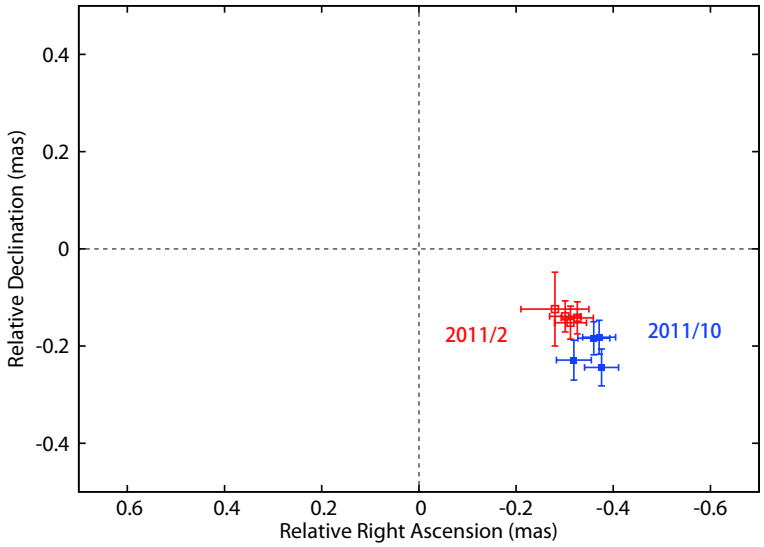

Figure 2.9: Phase-referenced core peak positions of NRAO 512 relative to core peak positions of 3C 345. Red blank squares represents the data obtained in 2011 February and blue filled squares represents the data obtained in 2011 October. The value of each peak position and its error are summarized in Table 2.6.

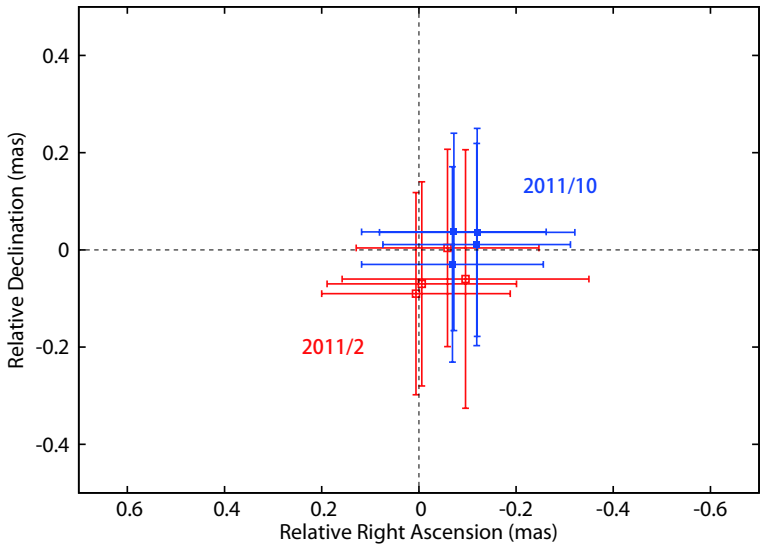

Figure 2.10: Core peak position of Mrk 501 relative to core peak position of NRAO 512. This plot is produced by subtracting the phase referencing position of NRAO 512 relative to 3C 345 from Fig. 2.8. Red blank squares represents the data obtained in 2011 February and blue filled squares represents the data obtained in 2011 October. The value of each peak position and its error is summarized in Table 2.9.

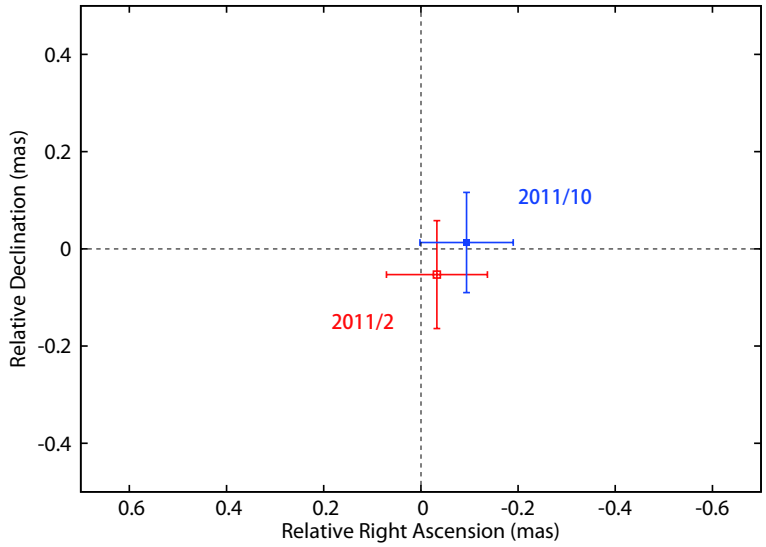

Figure 2.11: Weighted-mean core peak position of Mrk 501 relative to NRAO 512. Core peak position of Mrk 501 during successive observations are averaged using weighted averaging. Red squares represents the data obtained in 2011 February and blue squares represents the data obtained in 2011 October. The value of each peak position and its error is summarized in Table 2.10.

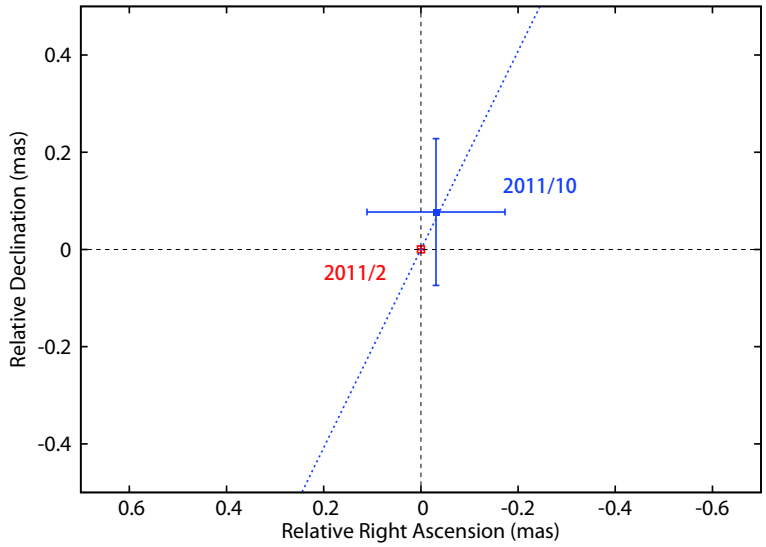

Figure 2.12: Projected weighted-mean core peak position of Mrk 501 in Fig. 2.11 at an averaged jet position angle of Mrk 501 $\sim 158°$, shown as dotted line. The projected weighted-mean core peak position in 2011 October (blue square) is plotted by aligning the position in 2011 February (red square) to the coordinate origin.

Table 2.9: Core peak position of Mrk 501 relative to NRAO 512.

Epoch	$\Delta\alpha$ (mas)	$\Delta\delta$ (mas)
(1)	(2)	(3)
2011/02/15	-0.006 ± 0.195	-0.070 ± 0.210
2011/02/16	-0.059 ± 0.188	0.004 ± 0.203
2011/02/17	-0.096 ± 0.254	-0.060 ± 0.266
2011/02/18	0.006 ± 0.194	-0.090 ± 0.208
2011/10/20	-0.069 ± 0.187	-0.030 ± 0.201
2011/10/21	-0.120 ± 0.201	0.036 ± 0.214
2011/10/23	-0.119 ± 0.193	0.011 ± 0.208
2011/10/24	-0.072 ± 0.190	0.037 ± 0.203

Notes.−(1) Observing epoch, (2) and (3) core peak position of Mrk 501 relative to NRAO 512 in right ascension and declination, respectively. These values are derived by subtracting (5) and (6) in Table 2.6 from Table 2.5. Each error is estimated as root-sum-square of corresponding error in Table 2.6 and Table 2.5.

Table 2.10: Weighted-mean core peak position of Mrk 501.

Epoch	$\Delta\alpha$ (mas)	$\Delta\delta$ (mas)
(1)	(2)	(3)
2011/02/15,16,17,18	-0.033 ± 0.104	-0.053 ± 0.111
2011/10/20,21,23,24	-0.094 ± 0.096	0.013 ± 0.103

Notes.−(1) Observing epoch, (2) and (3) weighted-mean core peak position of Mrk 501 relative to core peak position of NRAO 512 in right ascension and declination, respectively. These values are derived by using (5) and (6) in Table 2.9. Each error bars are estimated as root-sum-square of corresponding error in Table 2.9.

2.3 Observations and Data Reductions of VLBA Data

VLBA observations have two advantages compared to VERA observations: (1) the longest baseline is ∼8600 km (Fig. 2.13), which is about three times longer than that of VERA. VLBA 43 GHz provides an angular resolution as fine as ∼0.3 mas, corresponding to 0.2 pc in the case of Mrk 501, and the main positional error due to tropospheric error is reduced to typically more than one-third of VERA ones. (2) the image sensitivity of VLBA is typically seven times higher than that of VERA for the point source, because the number of VLBA antennas are 10, but that of VERA antennas are 4. Therefore, we perform the VLBA observations for one day per one month due to better positional accuracy and higher sensitivity.

Figure 2.13: VLBA is a system of ten radio-telescope antennas, each with a dish 25 meters in diameter. Image Credit: NRAO.

2.3.1 Observations and data reductions

On February 12, March 16, May 6, and June 11 in 2012, our phase-referencing observations toward Mrk 501 with VLBA at 43 GHz were conducted (proposal code: BK172A, BK172B, BK172C, BK172D). The observations involved rapid switching within 30 seconds between Mrk 501 and the nearby radio source 1659+399, which are separated by 1°.5 on the sky, including a few scans of the bright fringe-finder source 3C 345. Each session was about a four-hour

observation time at a data recording speed of 512 Mbps, correlated by software (Deller et al., 2011).

The initial data calibration was performed using the Astronomical Image Processing System (AIPS) mostly based on the standard VLBI data reduction procedures. The amplitude calibration with the opacity corrections was applied by using the measured system noise temperature and the elevation-gain curve of each antenna, and corrected ionospheric dispersive delays by using the ionospheric model provided by the Jet Propulsion Laboratory (JPL) and instrumental delays and phases by using a scan of 3C 345. Because Mrk 501 is much brighter than 1659+399, we chose Mrk 501 as a phase calibrator and transferred the derived fringe solutions to 1659+399. We performed a fringe-fitting on Mrk 501 and removed residual delays, rates and phases assuming a point source model. We further corrected the source structure phases due to the deviation of the point source model by imaging and self-calibrating to the Mrk 501 data. In standard phase-referencing data reduction, firstly these corrected phase and gain solutions are applied to 1659+399, then its phase-referenced images were created,and measure the peak position of phase-referenced images by fitting single Gaussian to the peak component using AIPS task JMFIT. In the case of VLBA 43 GHz observation, this peak position measurement would include negligible component identification error, because the target source has extended structure. This time we perform the new reduction procedure to remove the phase effect of target source structure. We produced the visibility of single point source with total flux of target source by using AIPS task UVMOD, and apply the calibrator fringe phase and structure phase to the visibility. Therefore, we could measure the peak position of phase-referenced target source free from its structure effect. The observing equations are summarized in Appendix C.

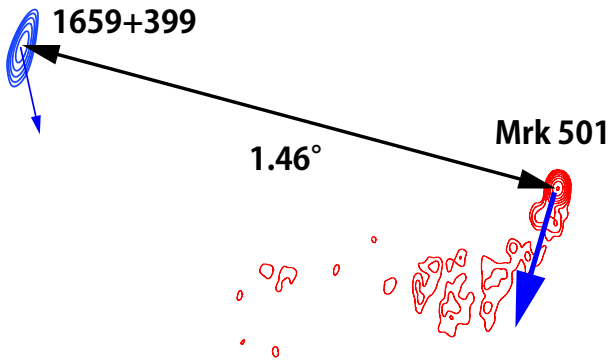

Figure 2.14: Source configuration of VLBA observation. Thanks to its high sensitivity, VLBA observations can use the closest calibrator 1659+399, which flux density is $\leq$200 mJy, by applying the phase of Mrk 501. These two self-calibrated images are produced from our observations. We found calibrator 1659+399 has the tiny jet elongated toward south-west direction shown as thin blue arrow.

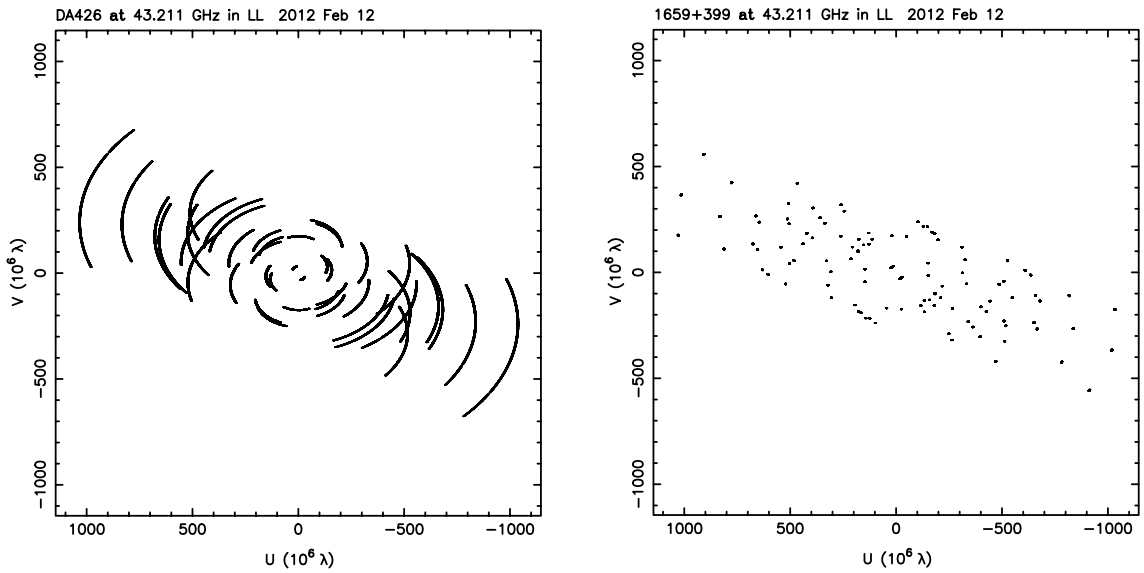

Figure 2.15: Typical uv-coverage of VLBA observations. The left image is the uv-coverage of Mrk 501, and the right image is that of 1659+399, obtained in 2012 February 12th.

2.3.2 Estimation of position errors

We estimate the position error in the same way as §2.1.2. Our VLBA observations can reduce three of seven error budgets explained in §2.1.2 because of the following advantages: (i) ionospheric effects are close to zero because the observing frequency is at 43 GHz. (ii) since apply the difference phase to point source uv, the core identification process which come from the source structures can be neglected. (iii) the instrumental phase error is zero because we observe both the target and the calibrator with the same VLBA system.

We summarize the estimated error budget in our phase-referencing observations in Table 2.11. Since these sources of errors contribute independently to each other, the total errors at each epoch can be obtained as the root-sum-square of them. Below details are described on the estimation for major error sources especially for VLBA observations.

Ionosphere

During our VLBA observations, $I \sim 7 \times 10^{16}$ m^{-2} over the sky of VLBA stations. Global ionospheric model based on GPS satellites have an accuracy of about $10 \sim 25\%$ (Mannucci et al. 1998). Adopting the uncertainty of 25%, δI corresponds to $\sim 1.8 \times 10^{16}$ m^{-2} and the zenith-angle-averaged values result in < 1 μas at 43 GHz for $\delta Z = 1.5^\circ$ and $D = 8.6 \times 10^3$ m.

Troposphere

Adopting a typical ∼2 cm misestimation of the zenith delay for the model used by the VLBA correlator (Neill 1996), this introduce the shift of the absolute position up to ∼ 26 μas at 43 GHz for $Z \sim 50^\circ$ and $\delta Z = 1.5^\circ$.

Table 2.11: Estimated positional error budgets in the phase-referencing observation by VLBA 43 GHz toward 1659+399 referencing to calibrator Mrk 501. The units are in μas.

Epoch	$\sigma_{\rm random}$		$\sigma_{\rm trop}$	$\sigma_{\rm ion}$	$\sigma_{\rm earth}$		$\sigma_{\rm ant}$		$\sigma_{\rm coord}$		$\sigma_{\rm rss}$	
	x	y			x	y	x	y	x	y	x	y
(1)	(2)	(3)	(4)	(5)	(6)	(7)	(8)	(9)	(10)	(11)	(12)	(13)
2012/02/12	4	10	26	< 1	3	5	1	5	2	3	27	29
2012/03/16	8	17	26	< 1	3	5	1	5	2	3	27	32
2012/05/06	8	19	26	< 1	3	5	1	5	2	3	28	33
2012/06/11	16	21	26	< 1	3	5	1	5	2	3	31	35

Notes.−(1) Observing epoch, (2) random error estimated by beamwidth over 2 times signal-to-noise ratio in the direction of right ascension, (3) in the direction of declination, (4) tropospheric residual errors, (5) ionospheric residual errors, (6) earth orientation parameter error in the direction of right ascension, (7) in declination, (8) antenna position error in the direction of right ascension, (9) in declination, (10) apriori source coordinates error in the direction of right ascension, (11) in declination, cause the positional error in μas of phase-referenced image. The error contributions from the geometrical errors (6)-(11) are estimated based on the simulation presented in Pradel et al. (2006). Total error in right ascension (12) and in declination (13) is estimated as the root-sum-square of each error.

2.4 VLBA Results

2.4.1 VLBA images

At first, we confirmed the self-calibration images of target 1659+399 and calibrator Mrk 501 shown in Fig. 2.16 and Fig. 2.17, respectively. Image qualities of Mrk 501 self-calibrated images are summarized in Chapter 3. Phase-referenced images of 1659+399 are summarized in Fig. 2.18. The image qualities of the phase-referenced images are summarized in Table 2.12. Phase-referenced target is detected with signal-to-noise ratio over 9.

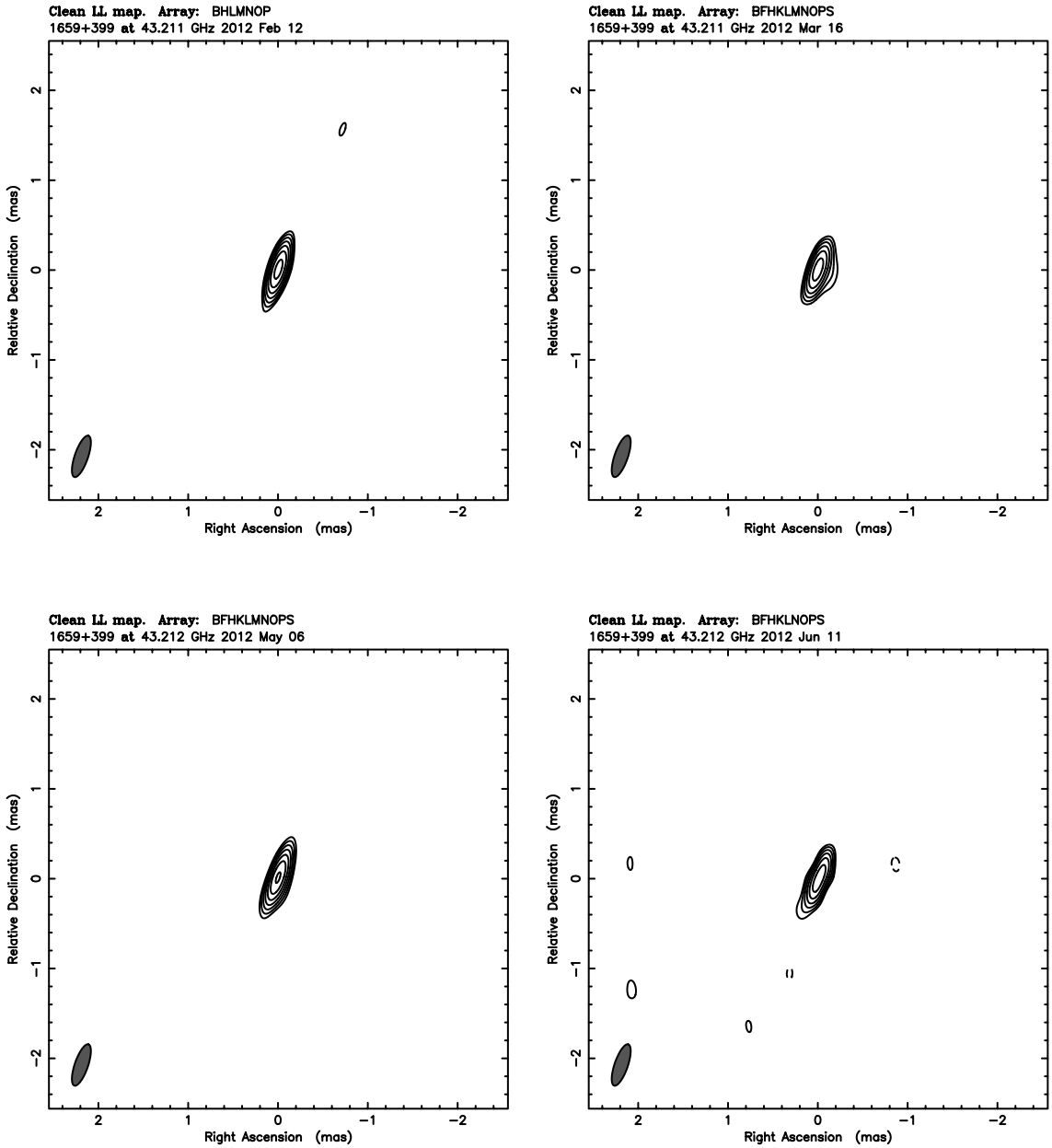

Figure 2.16: VLBA self-calibrated image of 1659+399. All the four epoch images of 1659+399 are shown with restored beam size of 0.486 mas × 0.148 mas at a position angle at −19.0°. Contours start from three times 5.73 mJy beam^{-1}, which is aligned to that of third epoch.

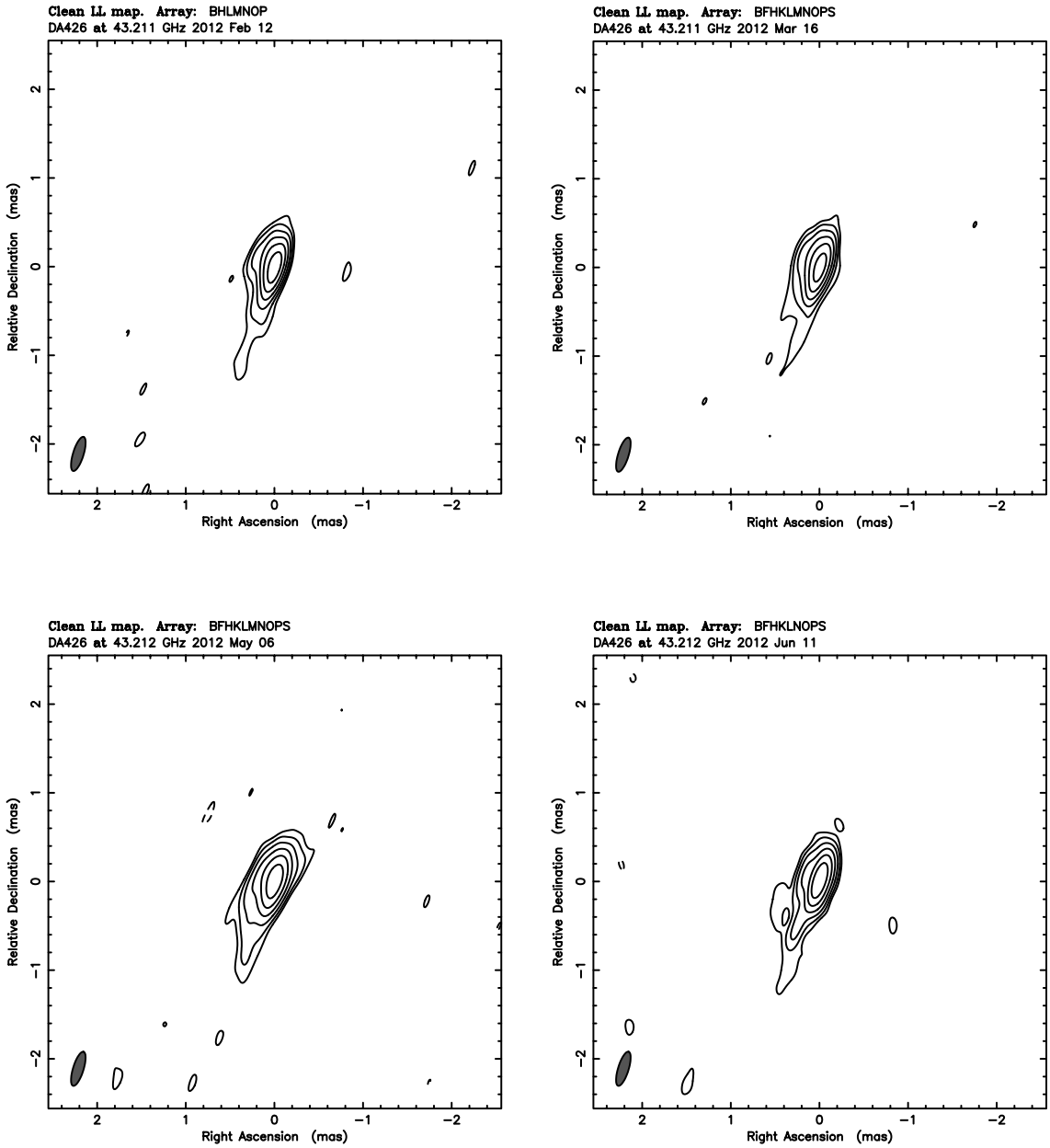

Figure 2.17: VLBA self-calibrated image of Mrk 501.All the four epoch images of Mrk 501 are shown with restored beam size of 0.402 mas $\times$ 0.119 mas at a position angle at $-17.2°$. Contours start from three times 1.30 mJy beam^{-1}, which is aligned to that of third epoch.

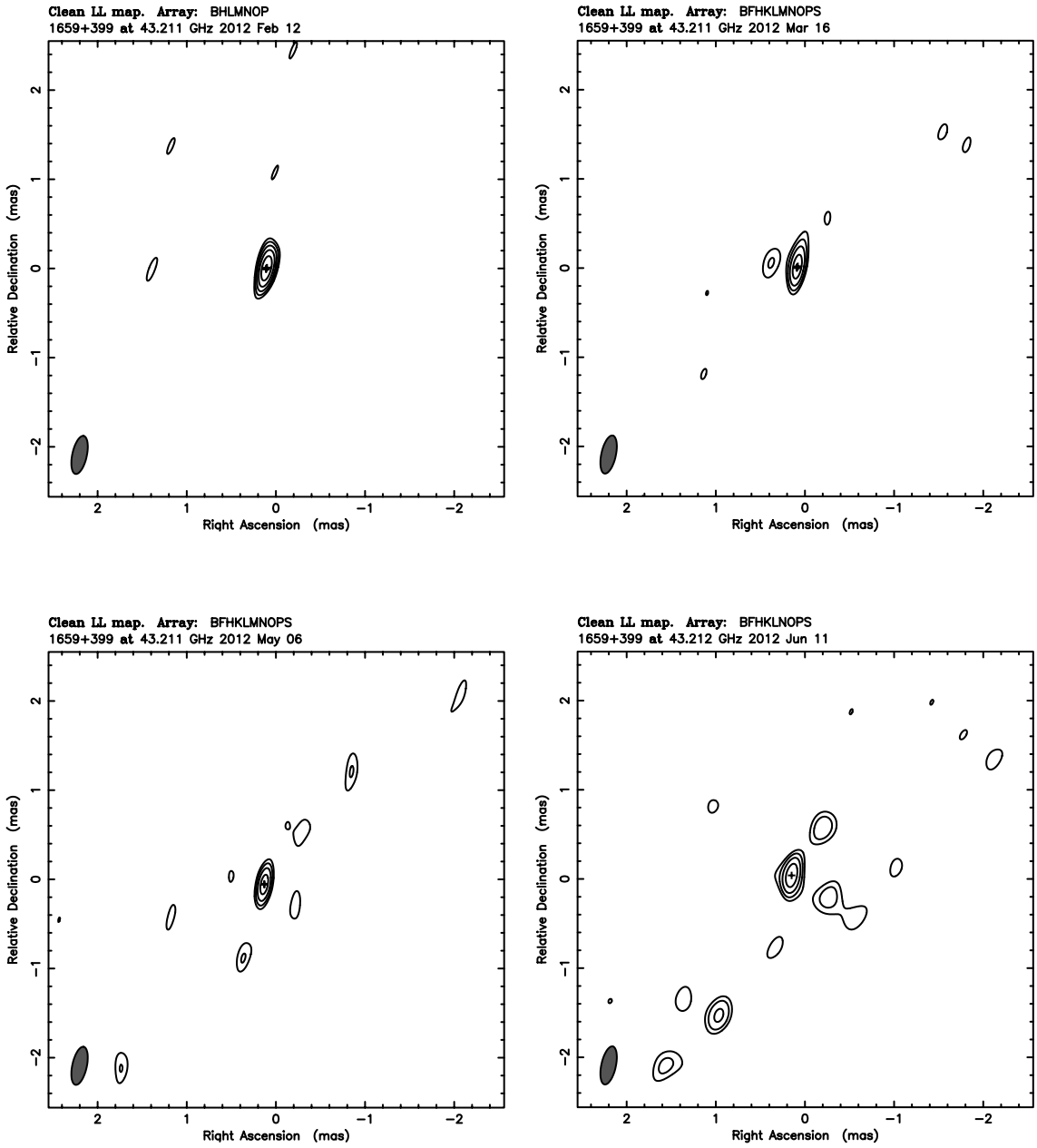

Figure 2.18: Phase-referenced image of 1659+399 relative to Mrk 501 by VLBA 43 GHz. All the four epoch images of 1659+399 are shown with restored beam size of 0.436 mas × 0.163 mas at a position angle at $-12.3°$. Contours start from three times 8.93 mJy beam^{-1}, which is aligned to that of third epoch.

Table 2.12: VLBA phase-referenced image qualities of 1659+399. Calibrator is Mrk 501.

Epoch	$I_{\rm p}$ (Jy beam^{-1})	$\sigma_{\rm rms}$ (Jy beam^{-1})	$I_{\rm p}/\sigma_{\rm rms}$	$\Delta\alpha$ (mas)	$\Delta\delta$ (mas)
(1)	(2)	(3)	(4)	(5)	(6)
2012/02/12	142	7.54	19	0.085 ± 0.027	-0.033 ± 0.029
2012/03/16	94	7.91	12	0.082 ± 0.027	-0.005 ± 0.032
2012/05/06	92	8.94	10	0.131 ± 0.028	-0.068 ± 0.033
2012/06/11	99	10.7	9	0.138 ± 0.031	0.032 ± 0.035

Notes.−(1) Observing epoch, (2) peak intensity, (3) rms of image noise, (4) image dynamic range, (5) and (6) position shifts from phase-tracking center of 1659+399. These position shifts were measured by two-dimensional gaussian fitting using task JMFIT in AIPS.

2.4.2 Core peak position of four epoch observations

In Fig. 2.19, the phase-referenced core peak positions of Mrk 501 relative to 1659+399 are plotted. This plot is produced by inverting the measured position of phase-referenced image of 1659+399 relative to Mrk 501 against the phase tracking center of 1659+399. The positional accuracy in one epoch is estimated as ~ 35 μas. From Fig. 2.19 and Table 2.12, the spatial distribution scale of phase-referenced core peak positions of Mrk 501 is (56 ± 41, 100 ± 48) μas in RA and Dec, by assuming the close calibrator 1659+399 is stationary.

We further discuss the core peak position of Mrk 501 along its jet axis. In Fig. 2.20, we plotted the projected phase-referenced core peak positions of Mrk 501 along averaged jet position angle of Mrk 501 $\sim 158°$. At a position angle of 158°, we perform chi-squared test of the phase-referenced core positions over four epochs within a χ^2/ndf of 5.5/3, and the core peak positions are stable with 13% probability. This result could be a small variability of radio core peak positions, however, we cannot say there is significant motion of the core peak position along its jet axis relative to 1659+399. The spatial distribution scale of core peak position along the jet axis during our observations is estimated to be 89 ± 43 μas. Therefore, we can say the phase-referenced core peak positions of Mrk 501 lie within 130 μas along its jet direction. Using inner jet viewing angle ~ 4 deg, the core peak positions of Mrk 501 along the jet direction lie within 1.3 pc during our four epoch observations.

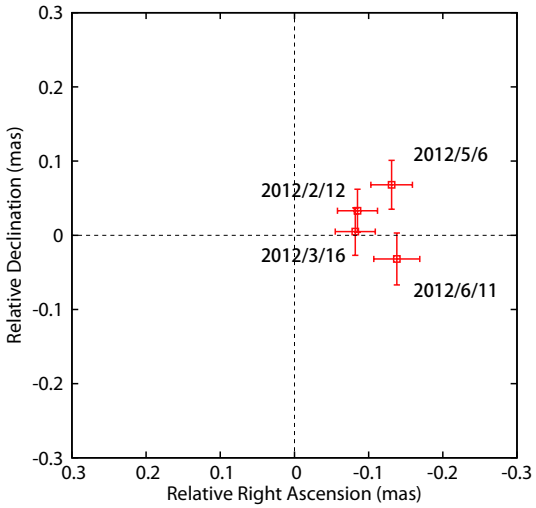

Figure 2.19: Phase-referenced position of Mrk 501 relative to 1659+399. This is a invert plot of phase-referenced position of 1659+399 relative to Mrk 501 against the phase tracking center of 1659+399.

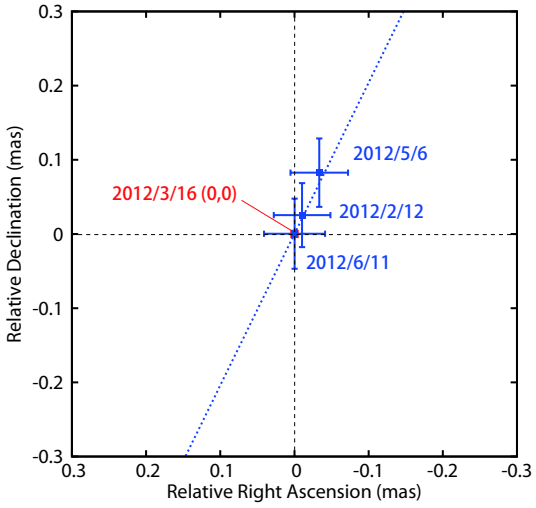

Figure 2.20: Phase-referenced position of Mrk 501, projected along the weighted-mean position angle of Mrk 501 jet $\sim 158^{\circ}$ shown as blue dashed line.

Chapter 3

Innermost Jet Imagings of Mrk 501

3.1 VLBA Data

In order to investigate the nature of inner sub-pc scale structure of Mrk 501, we analyzed totally nine VLBA data including our data and archival data at 43 GHz from the data archive system of the National Radio Astronomy Observatory (NRAO), summarized in Table 3.1. Data reduction was performed by using AIPS. A priori amplitude calibration was done based on the measurements of the system noise temperature during the observations and the elevation-dependent antenna gain provided by each station. In this process, we also applied opacity correction due to the atmospheric attenuation, assuming that the time variation of the opacity is not significant during each observation. Phase and delay offset depending on each IFs were solved by using the calibrator 3C 345 in our observation, and OJ 287 in archival data. Fringe fitting was performed with the AIPS task FRING on Mrk 501 by combining hole bandwidth into one channel. Imaging and self-calibration process was performed using Difmap software package (Shepherd, 1997). The final images were produced after iterations of CLEAN, phase and amplitude self-calibration processes. In some epochs, one or more antennas did not work properly because of technical problems or weather condition (see Table 3.1).

3.2 Results

3.2.1 Overall structures

Fig. 3.1 shows the total intensity images at 43 GHz. The convolved beam size is the common circular gaussian which is the averaged minor axis among our observations in natural weighting. We set the lowest contour equal to about three times the rms noise level of each image.

Table 3.1: Summary of VLBA 43 GHz Data

Epoch date	Obs Code	Map peak (mJy beam^{-1})	Beam size[a] (mas × mas, deg)			1σ rms (mJy beam^{-1})	Notes
2009 May 15	BK150	0.311	0.447	0.255	-30.8	2.498	HN raining
2010 May 30	BB281	0.261	0.371	0.181	-28.7	1.696	SC raining
2011 Sep 24	S4172F	0.235	0.477	0.260	-37.9	1.877	HN raining
2012 Feb 12	BK172A	0.231	0.514	0.1542	-19.8	0.898	no KP, SC, FD
2012 Mar 16	BK172B	0.234	0.490	0.187	-20.9	0.948	
2012 May 06	BK172C	0.253	0.443	0.158	-15.8	1.462	SC raining
2012 Jun 11	BK172D	0.279	0.409	0.226	11.4	0.988	no MK
2013 Jan 18	BK172E	0.158	0.513	0.198	-27.3	0.981	HN snow
2013 Feb 15	BK172F	0.187	0.465	0.178	-27.9	0.923	FD cloudy

Notes.−[a]Major axis, minor axis, and position angle of synthesized beam in natural weighting.

All the images shows core-dominant one side jet structure elongated toward south. The jet extends for roughly 1.1 mas (0.73 pc) at a position angle of $\sim -168^\circ$ .A few epochs seem to show the inner jet structures toward north, however, they might be side lobes. Especially, this time we newly find all the images except for top left panel shows elongated structure from the core toward north-east direction.

3.2.2 Modeling the VLBA data

In order to investigate jet structure change in Mrk 501, we deconvolve the source structure using the Difmap task model fit. In the modelfit process, we fit either elliptical or circular Gaussian model components to the visibility data of each epoch. For all epochs except for first and second epoch, overall structures are mostly well represented by four model components.

In the component identification process, we identify the brightest, innermost compact feature as the radio core. We assume the radio core are always the reference position, because the map peak positions are stationary from the result of phase-referencing observations in §2.3. This time we identify new component labeled NE, located at ~ 0.2 mas north-east of the core (see Fig. 3.2). Since typical beam size of our observation is $\sim$0.15 mas toward north-east direction, the component NE is resolved from the radio core. We label the other components C3 as the outermost component and C4 as the second outermost component, which were also identified in Piner et al. (2010). We could not identify component C5, locating at ~ 0.1 mas from the core with PA$\sim -170^\circ$ (Piner et al., 2010).

All details of the model fit analysis are shown in Table 3.2. We calculated the position uncertainties of each components by using the ratio of the size of each component to the signal-to-noise ratio (S/N). When the nominal error value is too small, we replace the error by a

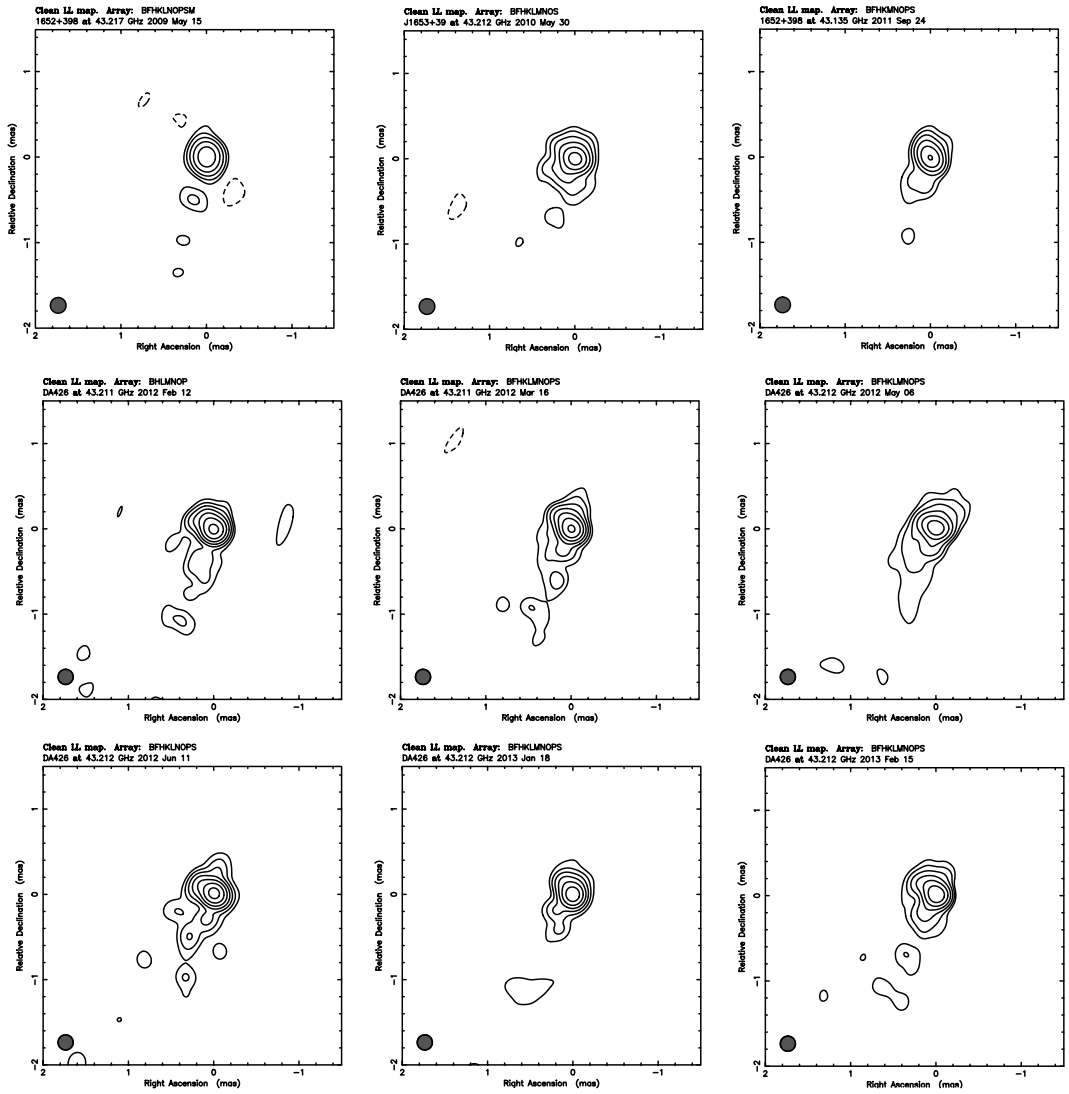

Figure 3.1: VLBA 43 GHz self-calibrated CLEAN images from 2009 May 15 to 2013 February 15. Image sizes are 3.5×3.5 mas^2 (1 mas corresponds to 0.662 pc). All the images are convolved with the same restoring beam of 0.184 mas in diameter. The lowest contours are all set to three times the rms noise level.

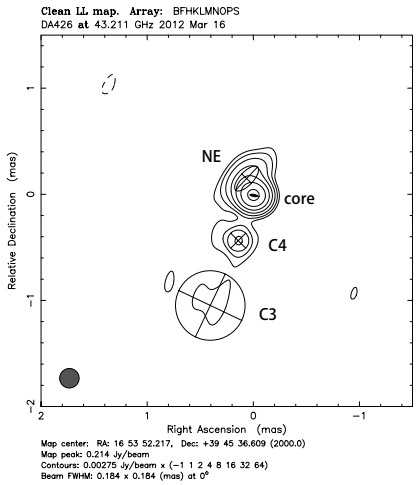

Figure 3.2: Image of Mrk 501 with model fit components for the 2012 Mar 16 at 43 GHz. Levels are drawn at (-1,1,2,4$\cdots$)$\times$ the lowest contour, that is 2.75 mJy beam^{-1}. The restoring beam size is the circular gaussian 0.1835 mas in radius.

conservative value equal to 10% of the beam size (Orienti et al., 2011).

3.2.3 Flux density variability

Using the results of the mode-fitting, we analyzed the time variability of the flux density for each component of the source. In Fig. 3.3, we show the light curve of all modelfit components for Mrk 501 from 2009 May 15th to 2013 February 15th. The average flux density of core is around 280 mJy, varying from 167 mJy to 412 mJy. We note a decrease in the NE flux density. From 2012 February to 2013 February, the flux density of NE decrease $\sim$60 mJy.

3.2.4 Proper motion

The results obtained from model fitting of visibilities (Table 3.2) are plotted in Fig. 3.4. We determined the proper motion of each component by means of linear fits to the separation of the individual features from the core at different epochs. From our analysis, we conclude that there is no radial proper motion in component NE from chi-squared test with 66% probability within a χ^2/ndf of 0.85/7. The relative distance of component NE from the radio core is ~ 0.19 mas. We estimate that two components have low-significance proper motion: C3 is $0.02 \pm 0.06c$ and C4 is$-0.10 \pm 0.06c$. These values are consistent with the proper motion derived by Piner & Edwards (2004).

Table 3.2: Gaussian models.

Epoch	Component ID	S^{a} (mJy)	$\sigma_S{}^{b}$ (mJy)	r^{c} (mas)	σ^{d} (mas)	PA^{c} (deg)	a^{e} (mas)	b/a^{f}	Φ^{g} (deg)
2009 May 15	Core	412	51	⋯	⋯	...	0.19	0.69	-7.8
	C4	41	14	0.54	0.03	164.4	0.16	1	⋯
	C3	23	2.3	1.00	0.03	165.8	0.18	1	⋯
2010 May 30	Core	329	38	⋯	⋯	...	0.16	0.62	-41.2
	NE	63	12	0.20	0.01	35.9	0.43	0.26	-40.1
	C4	80	13	0.39	0.12	159.3	0.61	1	⋯
2011 Sep 24	Core	272	34	⋯	⋯	...	0.17	0.77	-7.7
	NE	23	9.0	0.21	0.02	16.8	...	1	⋯
	C4	41	11	0.28	0.04	159.0	0.25	1	
	C3	32	10	0.93	0.11	158.9	0.51	1	
2012 Feb 12	Core	231	27	⋯	⋯	...	0.09	0.74	-58.5
	NE	89	13	0.17	0.02	18.4	0.24	0.09	-75.8
	C4	21	5.7	0.52	0.04	161.9	0.20	1	...
	C3	47	8.4	1.10	0.16	159.6	0.69	1	⋯
2012 Mar 16	Core	224	27	⋯	⋯	...	0.07	0.31	80
	NE	81	13	0.17	0.02	23.0	0.30	0.42	-43.3
	C4	23	6.8	0.45	0.04	161	0.20	1	⋯
	C3	32	7.7	1.11	0.24	158.4	0.66	1	⋯
2012 May 06	Core	383	44	⋯	⋯	...	0.23	0.63	-19.5
	NE	63	12	0.19	0.01	69.7	0.58	0.065	-28.2
	C4	29	8.5	0.56	0.03	151.4	0.21	1	⋯
	C3	18	7.4	1.11	0.04	160.6	0.15	1	⋯
2012 Jun 11	Core	311	36	⋯	⋯	...	0.16	0.61	-0.14
	NE	53	11	0.17	0.02	46.4	0.124	1	...
	C4	47	10	0.35	0.07	136.0	0.55	1	...
	C3	21	7.5	1.28	0.04	160.4	0.34	1	...
2013 Jan 18	Core	167	20	⋯	⋯	⋯	0.07	1	...
	NE	28	6.1	0.19	0.02	29.4	0.06	1	...
	C4	21	5.4	0.31	0.04	159.5	0.25	1	⋯
	C3	17	5.0	1.08	0.12	158.0	0.48	1	⋯
2013 Feb 15	Core	220	26	⋯	⋯	...	0.17	0.50	-31.8
	NE	58	9.7	0.19	0.01	39.1	0.28	0.43	-52.2
	C4	20	5.9	0.46	0.04	157.9	0.33	1	⋯
	C3	55	9.4	1.24	0.51	150.3	1.02	1	...

Notes. −[a]Flux density. [b]Estimated errors for the component flux density. [c]r and PA (position angle) are the polar coordinates of the component's center with respect to the core. The PA is measured from North through East. [d]Estimated errors in the component position. [e]The FWHM of the major axes of the Gaussian component. [f]The axial ratio of the FWHM of the Gaussian component. [g]Position angle of the major axis measured from North through East.

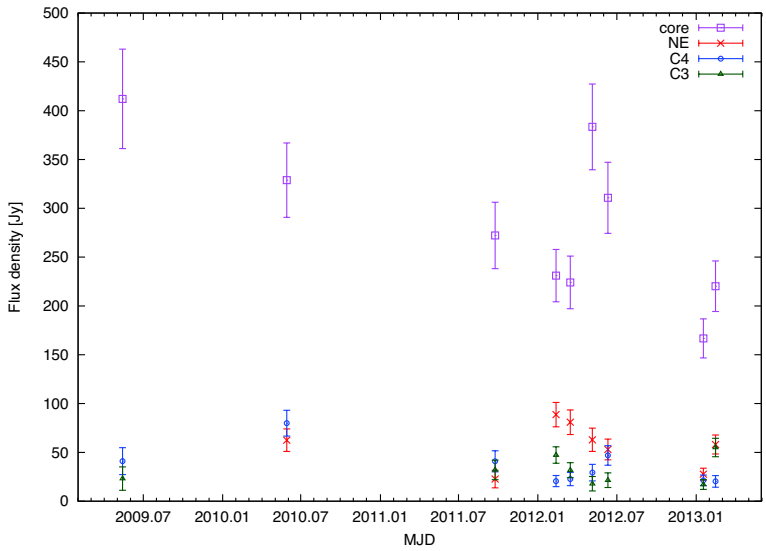

Figure 3.3: Light curves for Mrk 501. Purple squares, red crosses, blue circles and green triangles refer the flux densities of core, NE, C4 and C3, respectively. The flux error is estimated as the sum of typical 10 % calibration error and modelfit image rms of each epoch.

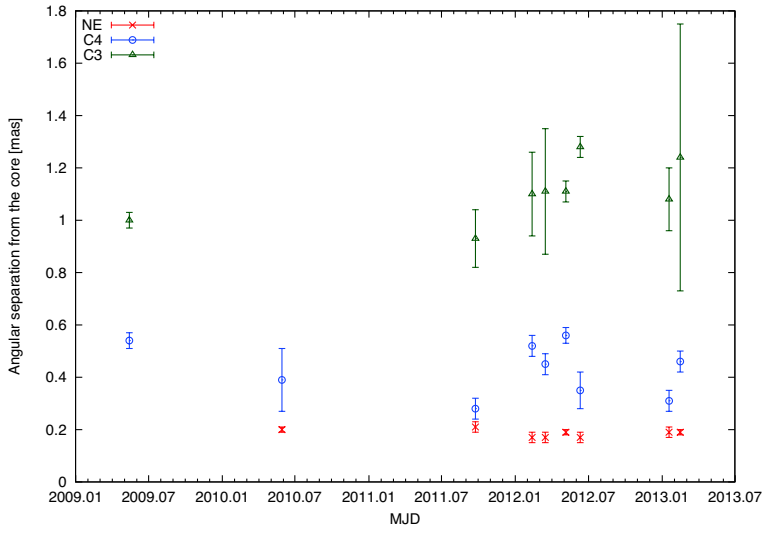

Figure 3.4: Angular separation from the core to each component. Red crosses, blue circles and green triangles represent the location of NE, C4 and C3, respectively.

Fig. 3.6 shows the two-dimensional position of each component relative to the core. For component NE, although the relative distance from the core does not change, the position angle against the core changes randomly. The other component C4 and C3 are located at average PA of 158°.

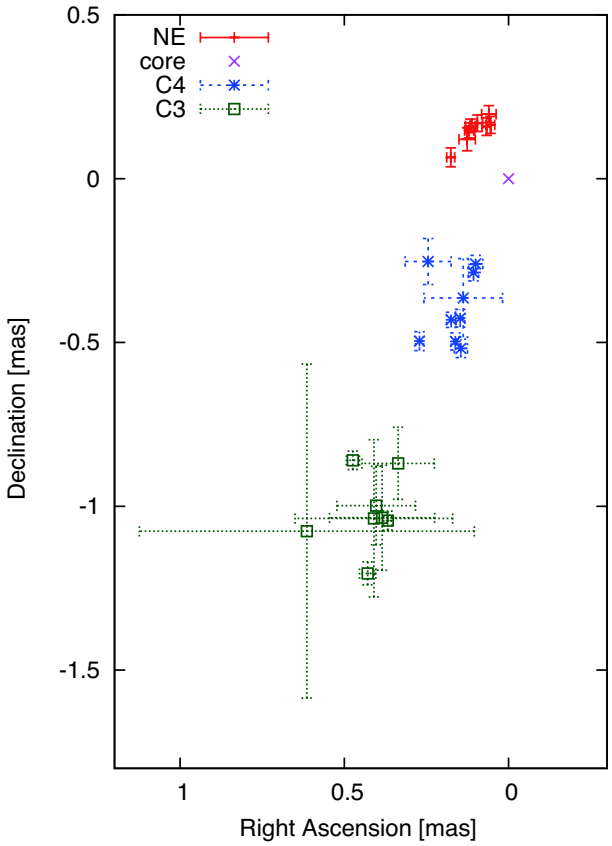

Figure 3.5: Relative positions of all the components refer to core peak position. Position error is estimated as 10% of the beam size or component size over SNR.

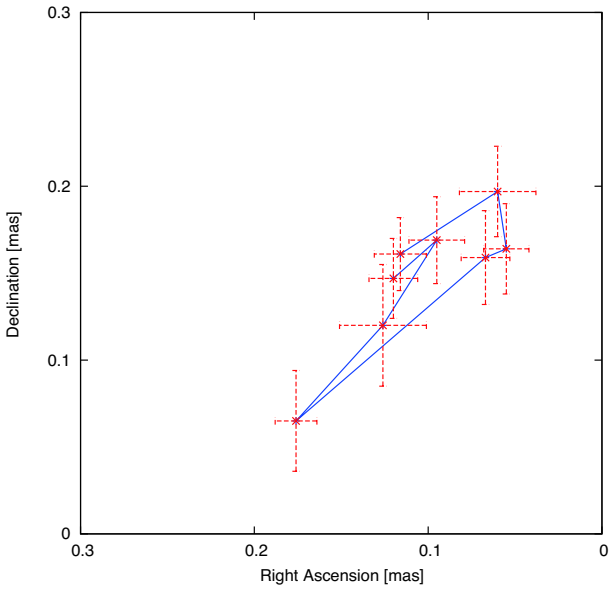

Figure 3.6: Relative positions of component NE refer to core peak position with lines. Position error is estimated as 10% of the beam size or component size over SNR.

Chapter 4

Discussion

4.1 Constraints on Bulk Lorentz Factor Ratio of X-ray Emitting Blobs

X-ray light curves of TeV blazars show the short-term variability, which means multiple flares occurring on timescales of about 1 day during continuous ∼7 days (e.g., Takahashi et al., 2000; Tanihata et al., 2001), and the long-term variability, which represents high amplitude variation spanned more than one month (e.g., Isobe et al., 2010). By comparing observed X-ray light curves of a TeV blazar to the numerical simulations of the internal shock model, it is found that the bulk Lorentz factor ratio of a maximum bulk Lorentz factor divided by minimum one in single collision within continuous seven days is ≤ 1.01 (Tanihata et al., 2003). However, the bulk Lorentz factor ratio of a maximum bulk Lorentz factor divided by minimum one during more than one month (b) has not been studied so far. In this work, we directly measure the positions of X-ray emitting blobs spanned more than one month with VLBI, since TeV blazars' synchrotron spectrum from radio to X-rays is characterized by one-zone model such that the positions of X-ray emitting blobs are identical to the peak positions of radio core. By using our astrometric measurements on the positions of X-ray emitting blobs, we discuss the bulk Lorentz factor ratio b in the framework of the internal shock model.

A distance between an internal shock region and a jet origin ($D_{\rm IS}$) is expressed in eq. (A.55) by using a faster blob's Lorentz factor ($\Gamma_{\rm f}$), a slower blob's Lorentz factor ($\Gamma_{\rm s}$), and the initial separation of the blobs ($I_{\rm IS}$) (see Fig.4.1). The shortest distance between an internal shock region and the jet origin ($D_{\rm min}$) is given by

$$D_{\rm min} \equiv D_{\rm IS,1} \sim 2\frac{\Gamma_{\rm f,1}^2\Gamma_{\rm s,1}^2}{\Gamma_{\rm f,1}^2-\Gamma_{\rm s,1}^2}I_{\rm IS,1} = 2\frac{a_1^2}{a_1^2-1}\Gamma_{\rm s,1}^2 I_{\rm IS,1} \tag{4.1}$$

where, $\Gamma_{\rm f,1},\ \Gamma_{\rm s,1} \gg 1$ and

$$\Gamma_{\rm f,1} \equiv a_1\Gamma_{\rm s,1}\ (a_1 > 1). \tag{4.2}$$

The subscript 1 represents the parameters of the internal shock occurred at the time of $t = t_1$. In the same way, the longest distance between the internal shock region and the jet origin ($D_{\rm max}$) is expressed as

$$D_{\rm max} \equiv D_{\rm IS,2} = 2\frac{a_2^2}{a_2^2 - 1}\Gamma_{\rm s,2}^2 I_{\rm IS,2}, \tag{4.3}$$

where, $\Gamma_{\rm f,2},\ \Gamma_{\rm s,2} \gg 1$ and

$$\Gamma_{\rm f,2} \equiv a_2\Gamma_{\rm s,2}\ (a_2 > 1). \tag{4.4}$$

The subscript 2 represents the parameters of the internal shock occurred at the time of $t = t_2$. Here $D_{\rm IS,2} \geq D_{\rm IS,1}$ (see Fig.4.1).

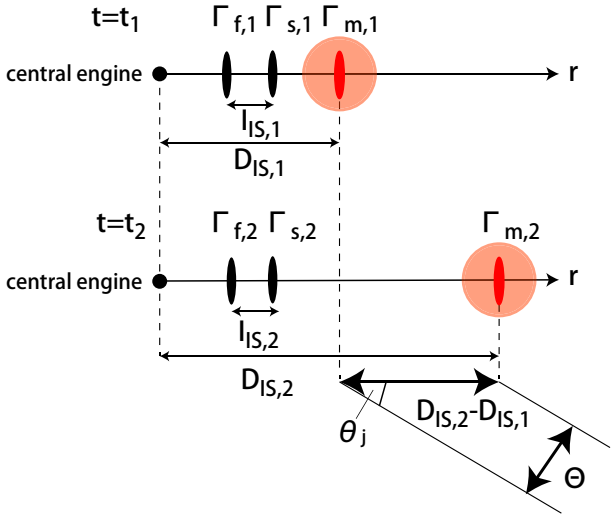

Figure 4.1: Notations of the internal shock model. The small red blobs represent the X-ray emitting blobs. The orange circles represent VLBI radio cores, which peak positions correspond to the locations of X-ray emitting blobs. We measure Θ, the spatial distribution scale of radio core positions, by conducting phase-referencing observations at 43 GHz with VERA and VLBA.

During our VERA astrometric observations, the core peak positions of Mrk 501 lie within the spatial distribution scale $\Theta \sim 220\ \mu$as between 2011 February and October. The deprojected scale is 2.0 pc, by using the lower limit of jet viewing angle $\theta_{\rm j} \sim 4^\circ$ (Giroletti et al., 2004a), and can be expressed by using eq.(4.1) and eq. (4.3) as

$$\begin{aligned} & D_{\rm IS,2} - D_{\rm IS,1} \leq 2.0\ {\rm pc}\left(\frac{\Theta}{220\ \mu{\rm as}}\right)\left(\frac{\theta_{\rm j}}{4^\circ}\right)^{-1}, \\ \Leftrightarrow\ & 2\frac{a_2^2}{a_2^2 - 1}\Gamma_{\rm s,2}^2 I_{\rm IS,2} - 2\frac{a_1^2}{a_1^2 - 1}\Gamma_{\rm s,1}^2 I_{\rm IS,1} \leq 2.0\ {\rm pc}\left(\frac{\Theta}{220\ \mu{\rm as}}\right)\left(\frac{\theta_{\rm j}}{4^\circ}\right)^{-1}. \end{aligned} \tag{4.5}$$

This equation includes six parameters: $a_1,\ a_2,\ \Gamma_{\rm s,1},\ \Gamma_{\rm s,2},\ I_{\rm IS,1},\ I_{\rm IS,2}$. Below, we assume following three relations to constrain on the maximum bulk Lorentz factor ratio of a maximum Lorentz factor divided by minimum one during more than one month interval, $b = \Gamma_{\rm s,2}/\Gamma_{\rm s,1}$ ($b \geq 1$).

(1) We assume the bulk Lorentz factor ratio of a faster blob and a slower blob in single collision at the time of $t = t_1$ is equal to that at the time of $t = t_2$: $a_1 = a_2 \equiv a$. Following Tanihata et al. (2003), the unshocked bulk Lorentz factor ratio of a maximum bulk Lorentz factor of a faster blob divided by minimum one of a slower blob within successive seven days is constrained to be ≤ 1.01. Therefore, we assume the upper limit of a for single collision is $a = 1.01$ to derive the upper limit of right-hand side in eq. (4.5). Thus, we substitute two parameters $(a_1,\ a_2) = 1.01$ in eq. (4.5). Note that we do not apply larger value of a (≥ 3) which is sometimes used in the several other internal shock models (e.g., Spada et al., 2001b; Guetta et al., 2004), because the simulated light curves are highly variable compared to the observed X-ray light curves (e.g., Tanihata et al., 2003).

(2) The mass of colliding blobs are equal: $m_1 = m_2$. When the blobs with equal mass collide, the efficiency of the collision is maximum as we estimated in eq. (A.41). In this case, we have the relation $\Gamma_{\rm s,1} = \Gamma_{\rm m,1}/\sqrt{a}$ and $\Gamma_{\rm s,2} = \Gamma_{\rm m,2}/\sqrt{a}$, where $\Gamma_{\rm m,1}$ and $\Gamma_{\rm m,2}$ is merged blob's Lorentz factor occurred at $t = t_1$ and $t = t_2$ ($\Gamma_{\rm m,1} \leq \Gamma_{\rm m,2}$). Moreover, since we observe the emission from the accelerated electrons in the merged blob, the range of merged blob's Lorentz factor is constrained from one-zone SED model fitting to be $\Gamma_{\rm m,1} \geq 8$ and $\Gamma_{\rm m,2} \leq 50$ (lower limit: Kino et al. 2002; upper limit: Albert et al. 2007). We substitute the minimum of $\Gamma_{\rm m,1} = 8$ into eq. (4.5) in order to derive the upper limit of its right-hand side. Note that the bulk Lorenz factor ratio b is $b = \Gamma_{\rm s,2}/\Gamma_{\rm s,1} = \Gamma_{\rm f,2}/\Gamma_{\rm f,1} = \Gamma_{\rm m,2}/\Gamma_{\rm m,1}$ ($b \geq 1$), since $a_1 = a_2 \equiv a$.

(3) The blob is ejected at constant distance (time) interval: $I_{\rm IS,1} = I_{\rm IS,2} \equiv I_{\rm IS}$. This assumption is reasonable because X-ray light curve of Mrk 501 for successive seven days shows roughly constant ($\sim$ 1 days) flare interval (Tanihata et al., 2001). In the case of Mrk 501, Schwarzschild radius $R_{\rm s}$ is estimated to be $(1.2 - 2.2) \times 10^9 M_\odot$ by using its central black hole mass (Barth et al., 2003), which is derived from $M - \sigma$ relation. Thus, $1R_{\rm s}$ is estimated to be $3.6 \times 10^{14} \leq R_{\rm s} \leq 6.6 \times 10^{14}$ cm. To derive the lower limit of the right-hand side in eq. (4.5), we use the lower limit of $I_{\rm IS} \equiv kR_{\rm s}$, that is, $k = 1$, $R_{\rm s} = 3.6 \times 10^{14}$ cm, and $M_{\rm BH} = 1.2 \times 10^9 M_\odot$. Here we substitute two parameters $(I_{\rm IS,1},\ I_{\rm IS,2}) = 1R_{\rm s}$ in eq. (4.5).

By substituting these 5 parameters: a_1, a_2, $\Gamma_{\rm m,1}$, $I_{\rm IS,1}$, and $I_{\rm IS,2}$, into eq. (4.5), we constrain remaining one parameter, that is, the bulk Lorentz factor ratio $b = \Gamma_{\rm m,2}/\Gamma_{\rm m,1} (= \Gamma_{\rm s,2}/\Gamma_{\rm s,1})$ as

$$
\begin{aligned}
& 2\frac{a}{a^2-1} I_{\rm IS} \left(\Gamma_{\rm m,2}^2 - \Gamma_{\rm m,1}^2\right) \leq 2.0 \text{ pc} \left(\frac{\Theta}{220\ \mu\text{as}}\right) \left(\frac{\theta_{\rm j}}{4^\circ}\right)^{-1}, \\
\Leftrightarrow\ & b^2 - 1 \leq 2.75\ k^{-1} \left(\frac{\Gamma_{\rm m,1}}{8}\right)^{-2} \left(\frac{A}{0.02}\right) \left(\frac{M_{\rm BH}}{1.2 \times 10^9 M_\odot}\right)^{-1} \left(\frac{\Theta}{220\ \mu\text{as}}\right) \left(\frac{\theta_{\rm j}}{4^\circ}\right)^{-1}, \quad (4.6)
\end{aligned}
$$

where we replace $(a^2 - 1)/a$ to A. Therefore, we obtain the constraint on the bulk Lorentz factor ratio b as

$$1 \leq b \leq 1.9 \ \text{ for VERA observations}, \quad (4.7)$$

$$1 \leq b \leq 1.6 \ \text{ for VLBA observations.} \tag{4.8}$$

In the case of VLBA observations, we obtain the constraint on b by applying $\Theta \sim 130$ μas. This constraints means the bulk Lorentz factor ratio is $b \leq 1.9$ over our long-term observations with VERA and VLBA. In this work, we firstly constrain the bulk Lorentz factor ratio spanned over eight months by VERA and over four months by VLBA. Here we note that for successive four days astrometric observations by VERA, the coincidence of the positions of X-ray emitting blobs within ~ 110 μas accuracy is consistent with the bulk Lorentz factor ratio within successive seven days being $a \leq 1.01$.

Next, we estimate the spatial distribution scale of radio core positions (and bulk Lorentz factor ratio) during different activity in X-ray for future observations. Following Iwashimizu et al. (2002), there is a model that the bulk Lorentz factor ratio $b_{\rm model}$ is related to observed synchrotron luminosity ratio q with one equation $q = b_{\rm model}^{3-s/2}$, where $q \equiv L_{\rm syn,o,2}/L_{\rm syn,o,1}$, $b_{\rm model} \equiv \Gamma_{\rm m,2}/\Gamma_{\rm m,1}$, and s is the power law index of electron energy distribution defined as $N_e(\gamma) \propto \gamma^{-s}$, which are determined through one-zone model fitting to SEDs of a TeV blazar in different activities. This model means that the larger (smaller) ratio of Lorentz factors corresponds to the higher (lower) variability of X-ray light curve. By using their model, we derive the model-dependent Lorentz factors during our observations by using the observed X-ray flux ratio. By applying $s = 1.6$ (where $s = 2\alpha + 1$ and $\alpha = 0.3$ for the spectrum of radio core in Mrk 501 from Sokolovsky et al. 2010), the index of $b_{\rm model}$ is 2.2. We summarized our input values and derived quantities in Table.4.1. During our astrometric observations, we derive the maximum X-ray count rate ratio by using the daily flux of Mrk 501 at energy 15-50 keV obtained from *Swift* X-ray/BAT public data. The ratio of averaged X-ray count rate is $q = 2.1$ among VERA observations, and $q = 2.3$ among VLBA observations. By using q, the model-dependent Lorentz factor ratio is estimated to be $b_{\rm model} = 1.4$ among VERA observations, and $b_{\rm model} = 1.5$ among VLBA observations, respectively. We apply this model to the different states of X-ray variability to estimate a spatial distribution scale of radio core positions. This source showed flaring states more than 10 times higher than usual in 1997 April at 10-100 keV by *BeppoSAX* observations (Pian et al., 1998; Tavecchio et al., 2001). When synchrotron luminosity ratio is roughly $q = 10$, the model-dependent Lorentz factor ratio is expected to be $b_{\rm model} = 2.8$. By substituting $b_{\rm model} = 2.8$ as b in eq. (4.6), the expected spatial distribution scale of radio core positions is estimated as

$$\Theta \geq 500 \ \mu{\rm as} \ k \left(\frac{\Gamma_{\rm m1,min}}{8}\right)^2 \left(\frac{A_{\rm max}}{0.02}\right)^{-1} \left(\frac{M_{\rm BH}}{1.2 \times 10^9 M_\odot}\right) \left(\frac{\theta_{\rm j}}{4^\circ}\right) \left[\left(\frac{b_{\rm model}}{2.8}\right)^2 - 1\right]. \tag{4.9}$$

This estimation suggests that the radio core position shift can be detectable by VERA phase-referencing observations with ~ 110 μas accuracy, during X-ray high flaring state with more than $q = 10$.

Table 4.1: Summary of our derivatives in §4.1.

epoch	q	$b_{\rm model}$	b	Θ
	(1)	(2)	(3)	(4)
2011 Feb/Oct	2.1	1.4	$1 < b < 1.9$	< 220 μas
2012 Feb/Mar/May/Jun	2.3	1.5	$1 < b < 1.6$	< 130 μas
1997 Apr	10	2.8	2.8 (expected)	500 μas (expected)

Notes.−(1) Observed X-ray luminosity ratio. (2) Model-dependent Lorentz factor ratio. (3) Bulk Lorentz factor ratio during more than one month interval. (4) Distribution range of X-ray emitting blobs.

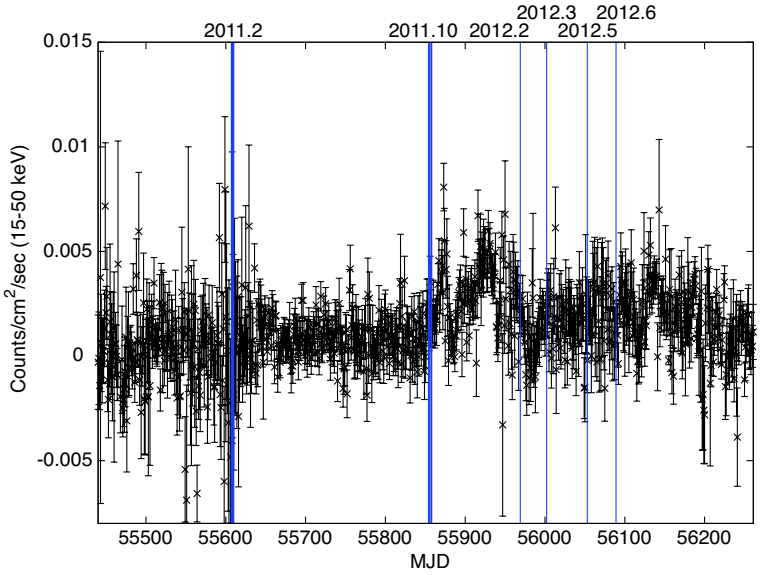

Figure 4.2: Swift/BAT X-ray light curve of Mrk 501 from 2010 September 1st to 2012 August 31st. The data points are obtained from Swift archive data service (http://heasarc.gsfc.nasa.gov/docs/swift/results/transients/weak/Mrk501/). The vertical blue lines represent the date of our VERA and VLBA astrometric observations.

4.2 Interpretation of North-East Components

From imaging analysis of Mrk 501 in §3, we find the new component NE, locating ~ 200 μas against the radio core at an averaged position angle of $\sim 35°$. In this section, we interpret the nature of NE within a framework of internal shock model.

In the previous section, we consider that the peak positions of radio core corresponds to the positions of the internal shock regions. If a direction of jet axis occasionally changes at its base, we expect the positions of component NE would corresponds to the positions of the internal shock regions (e.g., McKinney et al., 2013). The observed flux of radio core at frequency ν $S_{\rm core}(\nu)$ and that of component NE $S_{\rm NE}(\nu)$ is related to their intrinsic flux at frequency ν' $S_{\rm core}(\nu')(\propto \nu'^{-\alpha_1})$ and $S_{\rm NE}(\nu')(\propto \nu'^{-\alpha_2})$ ($\alpha_1,\ \alpha_2 \geq 0$) with their Doppler factor $\delta_{\rm core}$ and $\delta_{\rm NE}$ as follows:

$$\begin{aligned} S_{\rm core}(\nu) &= \delta_{\rm core}^{3+\alpha_1} S_{\rm core}(\nu'), \\ S_{\rm NE}(\nu) &= \delta_{\rm NE}^{3+\alpha_2} S_{\rm NE}(\nu'). \end{aligned}$$

For the exponent of each Doppler factor, we adopt $(3+\alpha)$ which is the case of discrete blobs (Urry & Padovani, 1995). The ratio of the flux of radio core to that of component NE ($R_{\rm obs}$) is expressed as

$$R_{\rm obs} \equiv \frac{S_{\rm core}(\nu)}{S_{\rm NE}(\nu)} = \frac{\delta_{\rm core}^{3+\alpha_1}}{\delta_{\rm NE}^{3+\alpha_2}} \frac{S_{\rm core}(\nu')}{S_{\rm NE}(\nu')} \equiv \frac{\delta_{\rm core}^{3+\alpha_1}}{\delta_{\rm NE}^{3+\alpha_2}} R_{\rm int} \tag{4.10}$$

where we define the ratio of the intrinsic flux of radio core and that of component NE as $R_{\rm int} = S_{\rm core}(\nu')/S_{\rm NE}(\nu')$. Eq. (4.10) contains eight parameters: $R_{\rm obs}$, $R_{\rm int}$, α_1, α_2, the bulk Lorentz factor of radio core $\Gamma_{\rm core}$ and jet viewing angle between the line of sight and the jet axis for core $\theta_{\rm core}$ in $\delta_{\rm core}$, and the bulk Lorentz factor of component NE $\Gamma_{\rm NE}$ and the viewing angle of component NE $\theta_{\rm NE}$ in $\delta_{\rm NE}$. By using the flux of radio core and that of component NE in Table 3.2, the observed flux ratio is

$$2.4 \leq R_{\rm obs} \leq 12 \tag{4.11}$$

during the detection of component NE. Assuming $R_{\rm int} = 1$, that is, $S_{\rm core}(\nu') = S_{\rm NE}(\nu')$, and $\alpha_1 = \alpha_2 \equiv \alpha$, eq. (4.10) yields

$$R_{\rm obs} = \left(\frac{\delta_{\rm core}}{\delta_{\rm NE}}\right)^{3+\alpha} = \left[\frac{\Gamma_{\rm NE}(1-\beta_{\rm core}\cos\,\theta_{\rm NE})}{\Gamma_{\rm core}(1-\beta_{\rm core}\cos\,\theta_{\rm core})}\right]^{3+\alpha}. \tag{4.12}$$

Let us consider the case that the fixed viewing angle of radio core $\theta_{\rm core} = 4°$ and $\alpha = 0.3$ which is the index of simultaneous spectrum for the radio core of Mrk 501 (Sokolovsky et al., 2010), and the small change of $\theta_{\rm NE}$ would strongly modulate the relativistically beamed jet emission with constant bulk Lorenz factor $\Gamma_{\rm core} = \Gamma_{\rm NE} \equiv \Gamma$ ($\beta_{\rm core} = \beta_{\rm NE} \equiv \beta$). For example, when we assume $\Gamma = 10$ ($\delta_{\rm core} = 13$), it yields to $6° \leq \theta_{\rm NE} \leq 8°$ ($5 \leq \delta_{\rm NE} \leq 9$) to interpret the observed

flux ratio. However, the half-opening angle of beaming corn with $\Gamma = 10$ is $\theta^* \sim 5^\circ$ from the relation of $\theta^* \sim 1/\Gamma$ (§A.1.3), the emission does not reach the observer with the viewing angle of $5^\circ \leq \theta_{\rm NE} \leq 8^\circ$. In Fig.4.3, we plot the expected $\theta_{\rm NE}$ as changing Γ. Red line and green dotted curve show the viewing angle of component NE when the observed flux ratio is $R_{\rm obs} = 2.4$ and $R_{\rm obs} = 12$, respectively. The allowed region of the viewing angle of component NE to satisfy the observed flux ratio range and the half-opening angle of beaming corn θ^* is shown as red shaded area in Fig. 4.3. However, the allowed region does not reproduce the green shaded area between the green dotted line and blue line in Fig. 4.3. To reproduce $R_{\rm obs} = 12$ under the constraint of $\theta^* \sim 1/\Gamma$, intrinsically the flux of NE should be lower than that of radio core, that is, $R_{\rm int} \geq 1.8$. Thus, the small ratio of intrinsic flux of radio core to that of component NE can explain the observed flux ratio by satisfying $\theta^* \sim 1/\Gamma$.

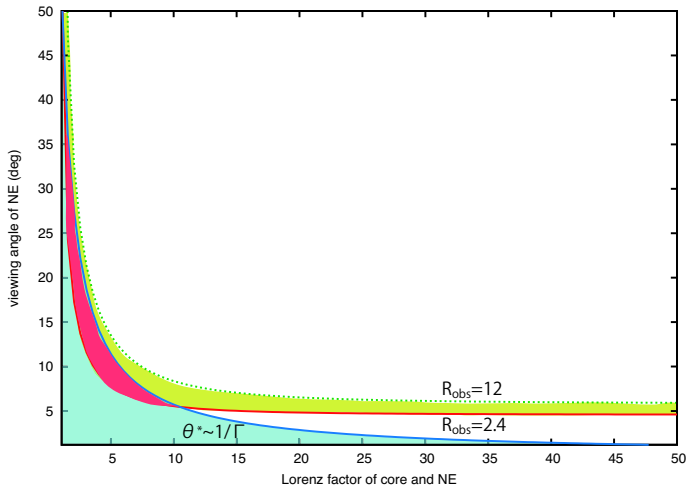

Figure 4.3: Bulk Lorentz factor of radio core and component NE vs viewing angle of NE. The green dotted line represents $R_{\rm obs} = 12$, the red line is $R_{\rm obs} = 2.4$, and the blue line is the half-opening angle of beaming corn $\theta^* \sim 1/\Gamma$. The red shaded area represents the allowed region from the half-opening angle of beaming corn and flux ratio between radio core and component NE.

4.3 Implications for Location of the Central Engine

When the positions of radio core and component NE corresponds to the locations of the internal shock regions, we predict that there two different jet axis on radio core and component NE respectively. We estimate one jet axis on the positions of radio core, C3, and C4 for all epochs by using least square fitting. In the same way, we estimate another jet axis on the positions of component NE for all epochs. In Fig. 4.4, we show the positions of all the components and the fitted lines. The intersection of two lines implies the location of central engine. The distance

between the intersection and the radio core corresponds to ~ 550 μas (5.2 pc). According to the internal shock model, the lower limit of the distance between the central engine and the internal shock region is estimated to be

$$D_{\rm min} \geq 0.75 \text{ pc } k^{-1} \left(\frac{\Gamma_{\rm m1}}{8}\right)^2 \left(\frac{A}{0.02}\right)^{-1} \left(\frac{M_{\rm BH}}{1.2 \times 10^9 M_\odot}\right) \tag{4.13}$$

by using eq. (4.1) and the parameters we used in §4.1. By substituting $k = 7$, or $\Gamma_{\rm m,1} = 21$, or $A = 2 \times 10^{-3}$ ($a = 1.001$) to eq. (4.13), $D_{\rm min} = 5.2$ pc. The apparent opening angle of the two jet axis is $\psi_{\rm ob} = 24°$. The actual opening angle (ψ) is magnified by the small viewing angle of the jet ($\theta_{\rm j}$),

$$\tan\psi_{\rm ob} = \frac{\tan\psi}{\sin\theta_{\rm j}}, \tag{4.14}$$

(Kameno et al., 2000). Taking $\theta_{\rm j} \geq 4°$, we have a jet opening angle of $\psi \geq 1.8°$.

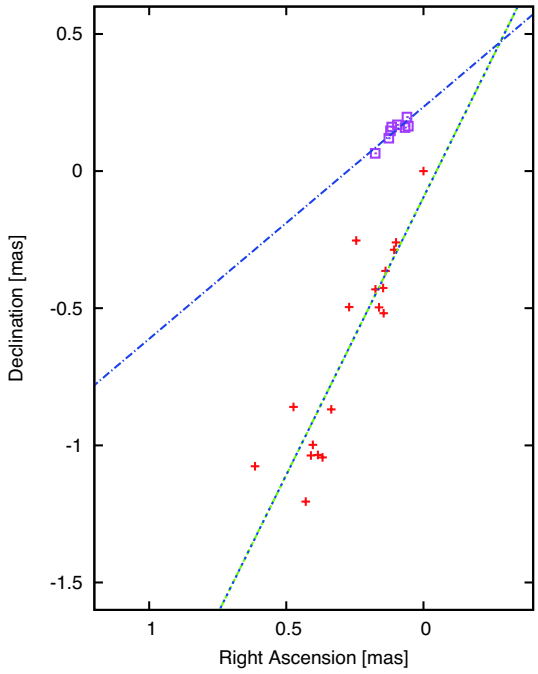

Figure 4.4: The dashed-dotted blue line is the least square line of the positions of component NE for all observations. The green dotted line is the least square line of the positions of radio core, C3, and C4 for all epochs.

Chapter 5

Conclusion

In order to test the internal shock model for blazars, we explore the positions of X-ray emitting blobs in TeV blazar Mrk 501 by conducting phase-referencing VLBI observations at 43 GHz. Since the radio core is optically thin against synchrotron self-absorption at 43 GHz and both X-ray and radio synchrotron emission is radiated by same electron populations, the positions of X-ray emitting blobs are identical to radio core positions. We have successfully measured the relative positions of 43 GHz radio core by VERA and VLBA and clarify the spatial distribution scales of X-ray emitting blobs in a blazar for the first time. The results and future prospects are summarized below.

1. By using VERA, we made phase-referencing observations of the radio core on successive four-days in February and October 2011. The phase-referenced radio core positions over successive four-days coincide within a positional accuracy ~ 200 μas. We conclude that the positional accuracy of X-ray emitting blobs for successive four-days as a single observation is ~ 110 μas.

2. During VERA observations, it is found that the averaged phase-referenced radio core positions over successive four-days projected along the jet axis lie within 83 ± 140 μas. Therefore, we conclude that the spatial distribution scale of X-ray emitting blobs along the jet axis is 220 μas (2.0 pc) at maximum between in February and October 2011.

3. We further conducted four epoch VLBA observations at 43 GHz, in February, March, May, and June 2012. With higher positional accuracy of VLBA, we find the radio core positions remain stationary within 89 ± 43 μas between February and June 2012.

We did not detect the significant position change of X-ray emitting blobs, however, our result can be interpreted in the framework of internal shock model. Based on our long-term (more than one month) observational results, we further constrain the bulk Lorentz factor ratio b of a maximum bulk Lorentz factor divided by minimum one, being $b \leq 1.9$. For future prospects, we expect the significant position change of X-ray emitting blobs during large X-ray flare states,

and the adequacy of the internal shock model can be test with the positional accuracy we have achieved in this work. Therefore, this work have established a new method to test the internal shock model for blazars.

Additionally, we investigate the sub-pc scale inner jet structure and its kinematics of Mrk 501 based on our astrometric results. From our VLBA 43 GHz observations and archival data, after 2010 May we discover a new component NE, located at ~ 200 μas northeast to the radio core, which direction is orthogonal to the jet axis. The relative positions of component NE to the radio core do not show any systematic motion but random trajectory and distribute within ~ 200 μas, which is comparable to the spatial distribution scale of the radio core derived by our astrometric observations. The ratio of radio core flux to the flux of component NE can be explained in a framework of the internal shock model. When the locations of component NE and radio core correspond to the location of internal shock region, we estimate the location of the central engine is ~ 550 μas (5.2 pc) upstream of radio core, and the intrinsic opening angle of the jet is $\sim 1.8°$.

Appendix A

Blazar Physics

Here we review relativistic effects and internal shock model which are used in this thesis. We use cgs unit throughout this paper.

A.1 Lorentz Transformation

This section is based on Chapter 4 in Rybicki & Lightman (1979). The theory of special relativity is based on two relations: (i) the laws of nature are the same in two frames of reference in uniform relative motion with no rotation, (ii) the speed of light is c in all frames. Let us consider two frames K^* and K', corresponding to AGN frame and comoving frame respectively, as shown in Fig.A.1 with relative uniform velocity v along the x axis. The origins of the two frames are assumed to coincide at $t = 0$. The relation between x^* y^* z^* t^* and x' y' z' t' is called the Lorentz transformation:

$$x' = \Gamma(x^* - vt^*),\ y' = y^*, \tag{A.1}$$

$$z' = z^*,\ t' = \Gamma(t^* - \frac{v}{c^2}x), \tag{A.2}$$

where

$$\Gamma \equiv \left(1 - \frac{v^2}{c^2}\right)^{-1/2} \tag{A.3}$$

The inverse of this transformation is

$$x^* = \Gamma(x' + vt'),\ y^* = y', \tag{A.4}$$

$$z^* = z',\ t^* = \Gamma(t' + \frac{v}{c^2}x), \tag{A.5}$$

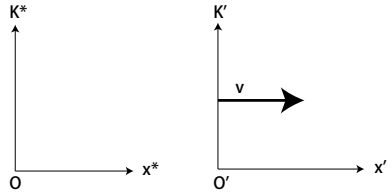

Figure A.1: Two frames K' (comoving frame) and K^* (AGN frame) with a relative velocity v along the x axis.

A.1.1 Length contraction

Suppose a rod of length $L_0 = x'_2 - x'_1$ at rest in comoving frame K'. This length measured in K^* is equal to $L = x^*_2 - x^*_1$ where x^*_2 and x^*_1 are the positions of the ends of the rod at the same time $t^*_2 = t^*_1$.

$$L = x^*_2 - x^*_1 = \frac{1}{\Gamma}(x'_2 - x'_1) = L_0/\Gamma \tag{A.6}$$

Therefore, the rod appears shorter by a factor $1/\Gamma$ at the rest in frame K^*.

A.1.2 Time dilation

Suppose a clock at rest at the origin of frame K' ($x' = 0$) an interval of time $T_0 = t'_2 - t'_1$. The interval of time measured at $x^* = 0$ in K^* is

$$T = t^*_2 - t^*_1 = \Gamma(t'_2 - t'_1) = \Gamma T_0 \tag{A.7}$$

The interval measured has increased by a factor Γ in frame K^*. Thus, the moving clock appears to have slowed down.

A.1.3 Transformation of velocities

We consider the relation between velocity u^* in frame K^* and velocity u' in frame K' measured at a point, as shown in Fig.A.2. With Lorentz transformation for differentials, we have the following relations:

$$u^*_x = \frac{dx^*}{dt^*} = \frac{\Gamma(dx' + vdt')}{\Gamma(dt' + vdx'/c^2)} = \frac{u'_x + v}{1 + vu'_x/c^2}, \tag{A.8}$$

$$u^*_y = \frac{u'_y}{\Gamma(1 + vu'_x/c^2)}, \tag{A.9}$$

$$u^*_z = \frac{u'_z}{\Gamma(1 + vu'_x/c^2)}. \tag{A.10}$$

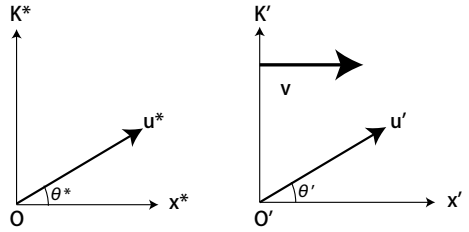

Figure A.2: Lorentz transformation of velocities between source comoving frame K' and AGN frame K^*.

The directions of the velocities of light ($|u'| = c$) in the two frames are related by the aberration formula,

$$\tan\theta^* = \frac{u_z^*}{u_x^*} = \frac{\sin\theta'}{\Gamma(\cos\theta' + v/c)}, \tag{A.11}$$

$$\cos\theta^* = \frac{u_x^*}{\sqrt{u_x^{*2} + u_z^{*2}}} = \frac{\cos\theta' + v/c}{1 + (v/c)\cos\theta'}, \tag{A.12}$$

$$\sin\theta^* = \frac{u_z^*}{\sqrt{u_x^{*2} + u_z^{*2}}} = \frac{\sin\theta'}{\Gamma[1 + (v/c)\cos\theta']}. \tag{A.13}$$

Photon is emitted to all direction, we set $\theta' = \pi/2$,

$$\tan\theta^* = \frac{c}{\Gamma v}, \tag{A.14}$$

$$\cos\theta^* = \frac{v}{c}, \tag{A.15}$$

$$\sin\theta^* = \frac{1}{\Gamma}. \tag{A.16}$$

For highly relativistic speeds v, that is, $\Gamma \ll 1$,

$$\theta^* \sim \frac{1}{\Gamma}. \tag{A.17}$$

If photons are emitted isotropically in K', then the photons in K^* are concentrated in forward direction, with half of them lying within a cone of half-angle $1/\Gamma$. This is called relativistic beaming effect.

A.1.4 Light travel time effect

Here we introduce third frame K, which is the rest frame of the observer as shown in Fig.A.3. The angle between observer's line of sight and the blob moving axis is θ. The moving source

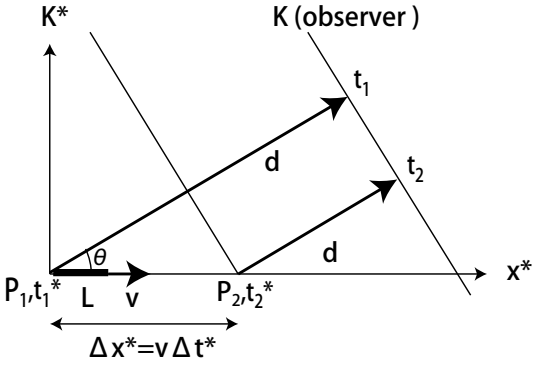

Figure A.3: Geometry for the Doppler effect.

emits one period of radiation as it moves from point 1 to point 2 during $\Delta t^* = t_2^* - t_1^*$ at velocity v. The difference in photon arrival times is

$$\begin{aligned} \Delta t_A &= t_2 - t_1 = (t_2^* + d/c) - (t_1^* + v\Delta t^* \cos\theta + d/c) \\ &= \Delta t^* \left(1 - \frac{v}{c}\cos\theta\right). \end{aligned} \tag{A.18}$$

The frequency of the radiation $\omega^{'}$ in the rest frame of the source (K') has the following relation between the period Δt^*

$$\Delta t^* = \frac{2\pi\gamma}{\omega^{'}}. \tag{A.19}$$

The frequency of the radiation ω in the rest frame of the observer is

$$\omega = \frac{2\pi}{\Delta t_A} = \frac{\omega^{'}}{\gamma\left(1 - \frac{v}{c}\cos\theta\right)}. \tag{A.20}$$

We usually define $v/c \equiv \beta$, and $\gamma(1 - v\cos\theta/c) \equiv 1/\delta$ as Doppler factor. Therefore, we have the relation:

$$\omega = \delta\omega^{'}. \tag{A.21}$$

This is the relativistic Doppler formula.

Apparent transverse velocity for observer is

$$\beta_{\rm app} = \frac{\beta\Delta t^* \sin\theta}{\Delta t_A} = \frac{v\sin\theta}{1 - \beta\cos\theta}. \tag{A.22}$$

For example, when $\cos\theta = \beta$, $\beta_{\rm app} = \gamma\beta$, apparent velocity can exceed the speed of light.

We consider a rod of length L_0 in the comoving frame K' is $L = L_0/\gamma$ in the frame K^*. The apparent length of a moving rod, which is affected by the fact that photons which arrive at the observer at the same time are emitted at different times. Equating the arrival times of photons emitted from point 1 and point 2 at times t_1^* and t_2^* respectively, we get:

$$\begin{aligned} t_1^* + \frac{\Delta x^* \cos\theta}{c} + \frac{d}{c} &= t_2^* + \frac{d}{c}, \\ \Delta t^* = t_2^* - t_1^* &= \frac{\Delta x^* \cos\theta}{c}, \end{aligned} \tag{A.23}$$

During Δt^*, the rod moves $\Delta x^* - L$.

$$\Delta x^* - L = v\Delta t^*, \tag{A.24}$$

$$\Delta x^* = \frac{L}{1 - \beta\cos\theta}. \tag{A.25}$$

Therefore, apparent length of the moving rod in observer frame is

$$\begin{aligned} L_{\rm app} &= \Delta x^* \sin\theta \\ &= \frac{L_0 \sin\theta}{\gamma(1 - \beta\cos\theta)} \\ &= \delta L_0 \sin\theta. \end{aligned} \tag{A.26}$$

In the case of $\cos\theta = \beta$, apparent length is $L_{\rm app} = \gamma L = L_0$, which is the same length as the proper length in comoving frame. This means that the moving rod is not affected by the Lorentz contraction.

A.1.5 Luminosity enhancement

When the observer's line of sight lie within the beaming corn, the observed luminosity is enhanced due to doppler boosting. Since the photon number from emission time $\Delta t'$, solid angle $2\pi\Delta\cos\theta'$, per unit frequency $\Delta\nu'$ in source comoving frame is conserved in observer's frame, there are following relations:

$$2\pi\Delta\cos\theta' \frac{L_{\nu'}}{4\pi h\nu'} \Delta\nu'\Delta t' = 2\pi\Delta\cos\theta \frac{F_\nu d^2}{h\nu} \Delta\nu\Delta t, \tag{A.27}$$

where d is the distance between observer and the emitting source. The energy in comoving frame E' can be relate to energy in observer frame E:

$$\begin{aligned} E' &= \Gamma(E - vp\cos\theta) \\ &= E\Gamma(1 - \beta\cos\theta) \\ &= E/\delta. \end{aligned} \tag{A.28}$$

where p is the momentum of the photon. From previous subsection, the relation between frequency and time is

$$\begin{aligned} \nu &= \delta\nu', \\ \Delta t &= \Delta t'/\delta. \end{aligned}$$

The conversion of solid angle is

$$\Delta\cos\theta = \frac{\Delta\cos\theta'}{\delta^2}. \tag{A.29}$$

By using above relations, eq.(A.27) can be rewrite to

$$F_\nu = \frac{L_{\nu'}}{4\pi d^2}\delta^3. \tag{A.30}$$

Thus, the observed luminosity is

$$\begin{aligned} L_{\rm ob} &= \int 4\pi d^2 F_\nu d\nu \\ &= \int L_{\nu'} d\nu' \delta^4 \\ &= L_{\rm so}\delta^4. \end{aligned} \tag{A.31}$$

Therefore, the observed luminosity $L_{\rm ob}$ is Doppler boosted by factor δ^4 from the source intrinsic luminosity $L_{\rm so}$.

A.2 Internal Shocks

A.2.1 Two-blob interaction

For instance, consider a collision between two blobs with masses $m_{\rm r}$ and $m_{\rm s}$ that are moving at different relativistic velocities $\beta_{\rm r}$ and $\beta_{\rm s}$, corresponding to Lorentz factor $\Gamma_{\rm f}$ and $\Gamma_{\rm s}$, respectively ($\Gamma_{\rm f} > \Gamma_{\rm s}$). After the rapid blob r catches up a slower one s, the two merge to form a single one m with mass m_m and Lorentz factor $\Gamma_{\rm m}$. From the conservation law of kinetic energy and momentum,

$$m_{\rm r}\Gamma_{\rm f}c^2 + m_{\rm s}\Gamma_{\rm s}c^2 = (m_{\rm r}+m_{\rm s})\Gamma_{\rm m}c^2 + E_{\rm m}\Gamma_{\rm m}, \tag{A.32}$$

$$m_{\rm r}\Gamma_{\rm f}\beta_r + m_{\rm s}\Gamma_{\rm s}\beta_{\rm s} = (m_{\rm r}+m_{\rm s})\Gamma_{\rm m}\beta_m + (E_{\rm m}/c^2)\Gamma_{\rm m}\beta_m, \tag{A.33}$$

where $E_{\rm m}$ is the internal energy of merged blob in the local frame and $E_{\rm m}\Gamma_{\rm m}$ is in the frame of external observer. From eq.(A.32),

$$E_{\rm m}\Gamma_{\rm m} = m_{\rm r}c^2(\Gamma_{\rm f}-\Gamma_{\rm m}) + m_{\rm s}c^2(\Gamma_{\rm s}-\Gamma_{\rm m}). \tag{A.34}$$

By substituting eq.(A.34) to eq.(A.33),

$$\begin{aligned}\beta_m &= \frac{m_{\rm r}\Gamma_{\rm f}\beta_r + m_{\rm s}\Gamma_{\rm s}\beta_{\rm s}}{m_{\rm r}\Gamma_{\rm f} + m_{\rm s}\Gamma_{\rm s}},\\ \Gamma_{\rm m} &= \frac{m_{\rm r}\Gamma_{\rm f} + m_{\rm s}\Gamma_{\rm s}}{\sqrt{m_{\rm r}^2 + m_{\rm s}^2 + 2m_{\rm r}m_{\rm s}\gamma_{rs}}},\end{aligned} \tag{A.35}$$

where $\gamma_{rs} = \Gamma_{\rm f}\Gamma_{\rm s} - \sqrt{\Gamma_{\rm f}^2 - 1}\sqrt{\Gamma_{\rm s}^2 - 1}$ is the relative Lorentz factor of blob s seen from blob r. Here we use the relation $\gamma^2\beta^2 = \gamma^2 - 1$. From eq.(A.32), the dynamical efficiency for converting the kinetic energy into the internal energy in a single collision is given by

$$\epsilon = 1 - \frac{(m_{\rm r} + m_{\rm s})\Gamma_{\rm m}}{m_{\rm r}\Gamma_{\rm f} + m_{\rm s}\Gamma_{\rm s}}. \tag{A.36}$$

When $\Gamma_{\rm f} > \Gamma_{\rm s} \gg 1$, the following part of the denominator of eq.(A.35) will be

$$\begin{aligned}2\gamma_{rs} &= 2(\Gamma_{\rm f}\Gamma_{\rm s} - \sqrt{\Gamma_{\rm f}^2 - 1}\sqrt{\Gamma_{\rm s}^2 - 1})\\ &= 2\Gamma_{\rm f}\Gamma_{\rm s}\left[1 - \sqrt{\left(1 - \frac{1}{\Gamma_{\rm f}^2}\right)\left(1 - \frac{1}{\Gamma_{\rm s}^2}\right)}\right]\\ &\approx 2\Gamma_{\rm f}\Gamma_{\rm s}\left[1 - \sqrt{1 - \left(\frac{1}{\Gamma_{\rm f}^2} + \frac{1}{\Gamma_{\rm s}^2}\right)}\right]\\ &\approx \Gamma_{\rm f}\Gamma_{\rm s}\left(\frac{1}{\Gamma_{\rm f}^2} + \frac{1}{\Gamma_{\rm s}^2}\right).\end{aligned} \tag{A.37}$$

Therefore, eq.(A.35) will be

$$\begin{aligned}\Gamma_{\rm m} &= \frac{m_{\rm r}\Gamma_{\rm f} + m_{\rm s}\Gamma_{\rm s}}{\sqrt{m_{\rm r}^2 + m_{\rm s}^2 + m_{\rm r}m_{\rm s}(\Gamma_{\rm s}/\Gamma_{\rm f} + \Gamma_{\rm f}/\Gamma_{\rm s})}}\\ &= \frac{m_{\rm r}\Gamma_{\rm f} + m_{\rm s}\Gamma_{\rm s}}{\sqrt{(m_{\rm r}\Gamma_{\rm f} + m_{\rm s}\Gamma_{\rm s})(m_{\rm r}/\Gamma_{\rm f} + m_{\rm s}/\Gamma_{\rm s})}}\\ &= \sqrt{\frac{m_{\rm r}\Gamma_{\rm f} + m_{\rm s}\Gamma_{\rm s}}{m_{\rm r}/\Gamma_{\rm f} + m_{\rm s}/\Gamma_{\rm s}}}.\end{aligned} \tag{A.38}$$

By using eq.(A.36) and eq.(A.38), we consider the following cases.

1. equal mass case: $m_{\rm r} = m_{\rm s}$

$$\Gamma_{\rm m} = \sqrt{\Gamma_{\rm f}\Gamma_{\rm s}}, \tag{A.39}$$

$$\epsilon = 1 - \frac{2\Gamma_{\rm m}}{\Gamma_{\rm f} + \Gamma_{\rm s}} = 1 - \frac{2\sqrt{\Gamma_{\rm f}\Gamma_{\rm s}}}{\Gamma_{\rm f} + \Gamma_{\rm s}}. \tag{A.40}$$

When the Lorentz factor of rapid blob is $\Gamma_{\rm f} = a\Gamma_{\rm s}$,

$$\Gamma_{\rm m} = \sqrt{a}\Gamma_{\rm s} \ , \tag{A.41}$$

$$\epsilon = 1 - \frac{2\sqrt{a}}{a+1}. \tag{A.42}$$

2. equal density case: $m_{\rm r}/\Gamma_{\rm f} = m_{\rm s}/\Gamma_{\rm s}$

$$\Gamma_{\rm m} = \sqrt{\frac{\Gamma_{\rm f}^2 + \Gamma_{\rm s}^2}{2}}, \tag{A.43}$$

$$\epsilon = 1 - \frac{\Gamma_{\rm f} + \Gamma_{\rm s}}{\sqrt{2(\Gamma_{\rm f}^2 + \Gamma_{\rm s}^2)}}. \tag{A.44}$$

When the Lorentz factor of rapid blob is $\Gamma_{\rm f} = a\Gamma_{\rm s}$,

$$\Gamma_{\rm m} = \sqrt{\frac{a^2+1}{2}}\Gamma_{\rm s}, \tag{A.45}$$

$$\epsilon = 1 - \frac{a+1}{\sqrt{2(a^2+1)}}. \tag{A.46}$$

3. equal energy case: $m_{\rm r}\Gamma_{\rm f} = m_{\rm s}\Gamma_{\rm s}$

$$\Gamma_{\rm m} = \sqrt{\frac{2\Gamma_{\rm f}\Gamma_{\rm s}}{\Gamma_{\rm f}/\Gamma_{\rm s} + \Gamma_{\rm s}/\Gamma_{\rm f}}}, \tag{A.47}$$

$$\epsilon = 1 - \frac{\Gamma_{\rm f} + \Gamma_{\rm s}}{\sqrt{2(\Gamma_{\rm f}^2 + \Gamma_{\rm s}^2)}}. \tag{A.48}$$

Therefore, the dynamical efficiency is the same as that of equal density case. When the Lorentz factor of rapid blob is $\Gamma_{\rm f} = a\Gamma_{\rm s}$,

$$\Gamma_{\rm m} = \sqrt{\frac{2}{a^2+1}}a\Gamma_{\rm s}, \tag{A.49}$$

$$\epsilon = 1 - \frac{a+1}{\sqrt{2(a^2+1)}}. \tag{A.50}$$

For example, when $a = 3$, (1) $\gamma_{m,1} \simeq 1.7\Gamma_{\rm s}$ and $\epsilon_1 = 0.13$, (2) $\gamma_{m,2} \simeq 2.2\Gamma_{\rm s}$ and $\epsilon_2 = 0.11$, and (3) $\gamma_{m,3} \simeq 1.3\Gamma_{\rm s}$ and $\epsilon_3 = 0.11$. Thus, we get the following relations: $\gamma_{m,2} > \gamma_{m,1} > \gamma_{m,3}$ and $\epsilon_1 > \epsilon_2 = \epsilon_3$. When $\Gamma_{\rm f} \to \infty$, $\epsilon_2 = \epsilon_3 \to 1 - 1/\sqrt{2} \simeq 0.3$ and $\epsilon_1 \to 1$, that means the collisions between equal mass blobs dissipate all the energy through internal shocks.

A.2.2 Pulse separation of internal shocks

The pulse width δT and the pulse separation ΔT of the light curves are well explained by the internal shock model (Kobayashi et al., 1997; Nakar & Piran, 2002). Firstly we consider the pulse separation time scale in §**??**, then explain the pulse width in §A.2.3. For pulse separation time scale, Kobayashi et al. (1997) simulated the internal shock model which N blobs are placed the same separation L apart at $t = 0$, then search the minimal collision time among all the collision time. (Nakar & Piran, 2002) simulate more realistic case, at $t = 0$ the front end of the first blob is emitted from the central black hole ($x = 0$) and the blob ejection interval can be set to the same separation L/c. They consider the arrival time interval between the photons from the first collision and the ideal photon from the first blob just ejected from the origin. We consider the arrival time interval between the photons from the first and second collision.

Consider N blobs ejected from the central engine into jet flow. For instance, three blobs are shown in Fig.A.4. Each blob (labeled i) is characterized by four parameters: a Lorentz factor $\Gamma_{\rm i}$ (a velocity β_i), a mass m_i, a blob's width l_i, the time of $\tilde{t}_i$ when the blob was ejected from the source. We define $L_{i,j}$ as the ejection interval between the rear end of the ith blob and the front of the jth blob. The time l_i/c corresponds to the period during the inner engine has operated, while $L_{i,j}/c$ corresponds to the period during the inner engine was quiet. We set the origin of time when the front end of the first blob is ejected at the time of $t = \tilde{t}_1 = 0$ and the position of $R_1(0) = 0$. At time $t > 0$, the front end of the blobs are at position : $R_i(t) = (t - \tilde{t}_i)\beta_i c$. At $t = \tilde{t}_{i+1}$, the initial separation between the front end of the blob i and $i + 1$ is

$$\begin{aligned} \delta R_{i,i+1} &= R_i(\tilde{t}_{i+1}) - R_{i+1}(\tilde{t}_{i+1}) = L_{i,i+1} + l_i, \\ \delta t_{i,i+1} &= \tilde{t}_{i+1} - \tilde{t}_i = \delta R_{i,i+1}/\beta_i c = (L_{i,i+1} + l_i)/\beta_i c. \end{aligned} \tag{A.51}$$

We denote the collision between blob i and $i + 1$ by the index $i, i + 1$ which takes place at the time of $t_{i,i+1}$ and the position of $R_c(t_{i,i+1})$. The collision time interval $\Delta t_{i,i+1}$, which is defined by the difference between the collision time ($t_{i,i+1}$) and the ejection time of blob $i+1$ ($\tilde{t}_{i+1}$), for all pairs $(i, i + 1)$ which satisfy $\beta_{i+1} > \beta_i$, is

$$\Delta t_{i,i+1} = t_{i,i+1} - \tilde{t}_{i+1} = L_{i,i+1}/c(\beta_{i+1} - \beta_i). \tag{A.52}$$

The collision position between blob i and $i + 1$ is

$$\begin{aligned} R_c(t_{i,i+1}) &= c\beta_{i+1}\Delta t_{i,i+1} \\ &= \frac{\beta_{i+1}}{\beta_{i+1} - \beta_i} L_{i,i+1}. \end{aligned} \tag{A.53}$$

By using the approximation $\beta_i \simeq (1 - 1/2\Gamma_{\rm i}^2)$,

$$R_c(t_{i,i+1}) \simeq \left(1 - \frac{1}{2\Gamma_{\rm i+1}^2}\right) / \left(\frac{1}{2\Gamma_{\rm i}^2} - \frac{1}{2\Gamma_{\rm i+1}^2}\right) \cdot L_{i,i+1}.$$

For $1/\Gamma_{\rm i}^2 \ll 1$,

$$R_c(t_{i,i+1}) \approx \frac{2\Gamma_{\rm i}^2\Gamma_{\rm i+1}^2}{\Gamma_{\rm i+1}^2-\Gamma_{\rm i}^2}L_{i,i+1}. \tag{A.54}$$

When $\Gamma_{\rm i+1} = a_{i+1}\Gamma_{\rm i}$ (a_{i+1}:constant),

$$R_c(t_{i,i+1}) \approx \frac{2a_{i+1}^2}{a_{i+1}^2-1}\Gamma_{\rm i}^2 L_{i,i+1}. \tag{A.55}$$

An observer at $R = R_0$ will begin to detect the radiation from this collision between blob i and $i+1$ at a time

$$t_{o,i,i+1} = t_{i,i+1} + [R_0 - R_c(t_{i,i+1})]/c. \tag{A.56}$$

We consider the next collision between a new unshocked blob $i+2$ and the merged blob j formed by the previous collision between blob i and $i+1$. The arrival time of the radiation from the collision occurred at position $R_c(t_{j,i+2})$ and time $t_{j,i+2}$ is

$$t_{o,j,i+2} = t_{j,i+2} + [R_0 - R_c(t_{j,i+2})]/c. \tag{A.57}$$

The observed time interval between collision $(i, i+1)$ and $(j, i+2)$ is

$$\begin{aligned}
\Delta T &= t_{o,j,i+2} - t_{o,i,i+1} \\
&= t_{j,i+2} + [R_0 - R_c(t_{j,i+2})]/c - [t_{i,i+1} + (R_0 - R_c(t_{i,i+1}))/c] \\
&= t_{j,i+2} - t_{i,i+1} - R_c(t_{j,i+2})/c + R_c(t_{i,i+1})/c \\
&= t_{j,i+2} - t_{i,i+1} - \beta_{i+2}\Delta t_{j,i+2} + \beta_{i+1}\Delta t_{i,i+1} \\
&= t_{j,i+2} - t_{i,i+1} - \beta_{i+2}(t_{j,i+2} - \tilde{t}_{i+2}) + \beta_{i+1}(t_{i,i+1} - \tilde{t}_{i+1}) \\
&\approx \tilde{t}_{i+2} - \tilde{t}_{i+1} \qquad \text{(A.58)} \\
&\approx L_{i+1,i+2}/c + l_{i+1}/c. \qquad \text{(A.59)}
\end{aligned}$$

Here we used the approximation $\beta \sim 1$. The time interval of pulse peak separation corresponds to the observed time interval between each collision. The observed time interval between the collisions $(i, i+1)$ and $(j, i+2)$ are equal to the ejection time interval of blob $i+1$ and $i+2$. In the case of $N \geq 4$ collision, the faster shell ejection interval reflect the observed pulse width.

A.2.3 Detail time profile of pulse width

There are five important time scales to interpret detail time profile of pulse width. Dominant two time scales basically determine the rise and decay time scales of the profile. Other four time scales should be considered as smearing effect on the profile when their time scales are longer than the dominant time scales. This section is based on §10 in Kataoka et al. (1999).

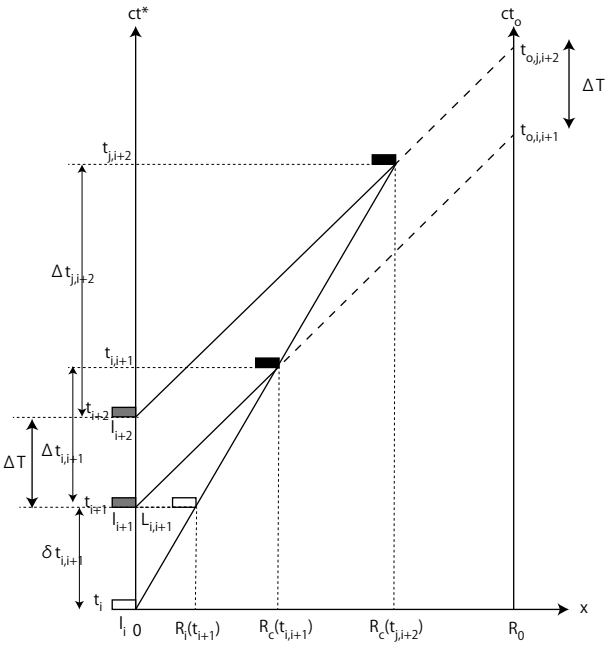

Figure A.4: Space-time coordinate of the internal shock model by using three blobs.

Dominant decay time scale: synchrotron cooling time $t_{\rm cool}$

Synchrotron cooling time corresponds to the time scale for a single electron to lose its kinetic energy E via synchrotron cooling power $P_{\rm sync}$.

$$\begin{aligned} t_{\rm cool} &= \frac{E}{P_{\rm sync}} \\ &= \frac{\gamma mc^2}{\frac{4}{3}\sigma_T c\beta^2 U_B \gamma^2} \\ &= C_1 B^{-2}\gamma^{-1}, \end{aligned} \tag{A.60}$$

where

$$C_1 = \frac{6\pi mc}{\sigma_T \beta^2} = 7.8\times 10^8. \tag{A.61}$$

Here $\sigma_T = 8\pi r_0^2/3$ is the Thomson cross section, and $U_B = B^2/8\pi$ is the magnetic energy density. The synchrotron critical frequency is defined as

$$\nu_c = C_2 \gamma^2 B, \tag{A.62}$$

where

$$C_2 = \frac{3e}{4\pi mc} = 4.2\times 10^6. \tag{A.63}$$

For example, the Lorentz factor of an electron emitting X-ray ($\sim$ 1keV) is estimated as

$$\gamma = 7.6 \times 10^5 \left(\frac{\nu}{2.4 \times 10^{17}\ \mathrm{Hz}}\right)^{1/2} \left(\frac{B}{0.1\ \mathrm{G}}\right)^{-1/2}, \tag{A.64}$$

by assuming typical magnetic field strength $B \sim 0.1$ G. Therefore, synchrotron cooling timescale for X-ray emitting electron is estimated as

$$t_{\mathrm{cool}} = 1.0 \times 10^5 \left(\frac{B}{0.1\ \mathrm{G}}\right)^{-2} \left(\frac{\gamma}{7.6 \times 10^5}\right)^{-1}\ [\mathrm{sec}]. \tag{A.65}$$

This means that X-ray photon from a single electron is cooled by synchrotron radiation over $\sim$27 minutes. Since the cooling time is proportional to γ^{-1}, higher energy electrons are cooled much faster than lower energy electrons.

$$B_{\mathrm{eq}} = 0.35 \left(\frac{S}{89\ \mathrm{mJy}}\right)^{2/7} \left(\frac{a \cdot b \cdot c}{0.24 \cdot 0.02 \cdot 0.2}\right)^{-2/7}\ [\mathrm{G}], \tag{A.66}$$

by assuming the component flux $S = 89$ mJy and the ellipsoid volume $4\pi a \cdot b \cdot c/3$. The Lorentz factor of an electron emitting radio ($\sim$ 43 GHz) is

$$\gamma = 1.7 \times 10^2 \left(\frac{\nu}{4.3 \times 10^{10}\ \mathrm{Hz}}\right)^{1/2} \left(\frac{B_{\mathrm{eq}}}{0.35\ \mathrm{G}}\right)^{-1/2}. \tag{A.67}$$

Synchrotron cooling time for the radio emitting electron is estimated to be

$$t_{\mathrm{cool}} = 3.7 \times 10^7 \left(\frac{B_{\mathrm{eq}}}{0.35\ \mathrm{G}}\right)^{-2} \left(\frac{\gamma}{1.7 \times 10^2}\right)^{-1}\ [\mathrm{sec}]. \tag{A.68}$$

The electron is cooled by synchrotron radiation over 7.5 years.

Dominant rise time scale: acceleration time t_{acc}

Electrons in the system is accelerated by a shock at a time via first order Fermi acceleration.

$$t_{\mathrm{acc}} = \frac{3}{v_1 - v_2}\left(\frac{K_1}{v_1} + \frac{K_2}{v_2}\right), \tag{A.69}$$

where

$$K = \frac{v r_L}{3}\eta, \tag{A.70}$$

and

$$r_L = \frac{\gamma m v}{qB}.$$

η is typically $1 \sim 10$. Assuming $K_1 = K_2$ and $v_1 = 4v_2$,

$$t_{\mathrm{acc}} = \frac{5K_1}{4v_2^2}. \tag{A.71}$$

$v_2 \sim c/\sqrt{3}$ for relativistic shock speed. Thus, typical acceleration time scale is ~ 1 sec.

Smearing rise time scale: injection time $t_{\rm inj}$

The non-thermal electrons are injected into the shock front, which are newly produced by collisions of blobs moving with different bulk Lorentz factors (internal shock model). Injection time scale is

$$t_{\rm inj} = \frac{2R}{v_s}, \tag{A.72}$$

where $2R$ is the size of a single blob, and v_s is the shock velocity. The shock velocity is usually $\sim v_s \sim c/\sqrt{3}$ in the case of relativistic shock, derived by relativistic Rankine-Hugoniot equations.

Smearing time scale: angular spreading timescale $t_{\rm ang}$

Suppose that the spherical shell of radius $R^*(t)$ is expanding with relativistic velocity $\beta \sim 1$, $\Gamma \ll 1$ and energized by a stationary point at its center. By considering of relativistic beaming effects, an observer sees up to solid angle of Γ^{-1} of isotropically expanding shell at the rest of AGN frame. Referring to Fig.A.5, we see that the cones of emission at any surface point region of the sphere, between points B and B'. Emission from points such as C will not reach the observer. The observed duration δt of any pulse has the time delay between the observed radiation from A and B (or B'):

$$\begin{aligned} \delta t &= R^*(t)(1-\cos\theta^*)/c \\ &\approx \frac{R^*(t)\theta^2}{2c}. \end{aligned}$$

For $\theta \sim 1/\Gamma$,

$$\delta t \approx R^*(t)/2\Gamma^2 c, \tag{A.73}$$

$$\delta t^* \approx 2\Gamma^2 \delta t. \tag{A.74}$$

δt is called as angular (spreading) time scale. The observed duration $\sim R/c$ in non-relativistic case is contracted by the doppler beaming by a factor of $1/2\Gamma^2$.

Smearing time scale: light crossing time $t_{\rm crs}$

Light crossing time means the difference of photon arrival time emitted from the front side and back end of the emitting spherical blob:

$$t_{\rm crs} = \frac{R}{c}. \tag{A.75}$$

This time scale affects both rise and decay of the pulse light curve.

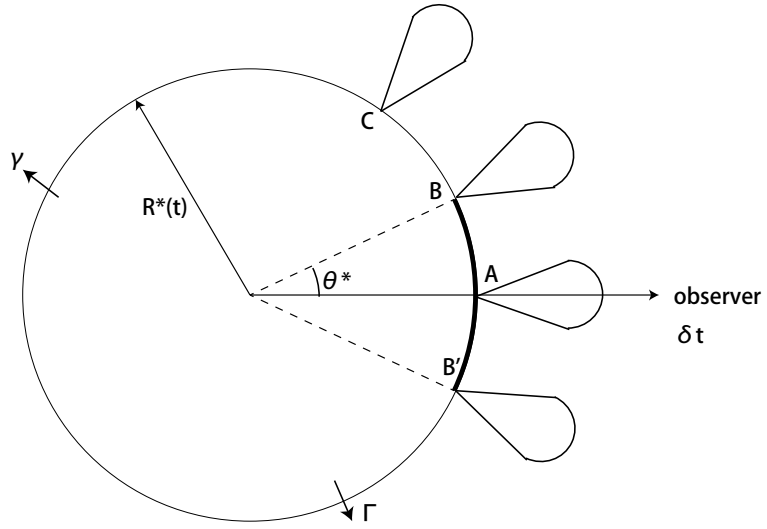

Figure A.5: Geometry of emission cones from points on the surface of a rapidly expanding blob.

Smearing decay time scale: adiabatic expansion time $t_{\rm ad}$

The flux of the blob decay via adiabatic expansion.

$$t_{\rm ad} = \frac{R}{v_{\rm ad}}, \tag{A.76}$$

where $v_{\rm ad}$ is the adiabatic expansion velocity, which corresponds to the sound speed propagating through the blob. Therefore, usually $\sim 2R/c$ is dominant time scale for explaining pulse width at X-ray, and $t_{\rm cool}$ is dominant decay time scale at radio band.

A.3 Fermi Acceleration

Fermi acceleration is the acceleration process that charged particles gain the energy when they are reflected by a (magnetic) mirror. There are two types of Fermi acceleration: First order Fermi acceleration and Second order Fermi acceleration. Power law spectrum is came out from First order Fermi acceleration. Second order Fermi acceleration is thought to be the more effective acceleration mechanism which particles gain nonthermal energies in astrophysical shock waves, such as supernova remnants and AGN jets.

A.3.1 Second order Fermi acceleration

Fermi acceleration is originally suggested by Enrico Fermi (1949).

Firstly, we consider a collision between two particles 1 and 2, with mass m_1, m_2, velocity v_1, v_2, and velocity after the collision v_1', v_2', respectively. Here we assume $m_1 \ll m_2$ and completely-elastic collision. For the collision coefficient is uniform,

$$1 = -\frac{v_1' - v_2'}{v_1 - v_2}. \tag{A.77}$$

This formula means that the initial relative velocity of particle 1 with reference to particle 2 is just sign inverted relative velocity after the collision. For momentum conservation,

$$m_1 v_1 + m_2 v_2 = m_1 v_1' + m_2 v_2'. \tag{A.78}$$

From eq. (A.77) and (A.78),

$$\begin{aligned} v_1' &= \frac{(m_1 - m_2)v_1 + 2m_2 v_2}{m_1 + m_2} \\ v_2' &= \frac{2m_1 v_1 + (m_2 - m_1)v_2}{m_1 + m_2}. \end{aligned} \tag{A.79}$$

If $m_1 \ll m_2$,

$$\begin{aligned} v_1' &= -v_1 + 2v_2, \\ v_2' &= v_2. \end{aligned} \tag{A.80}$$

For Fermi acceleration case, a charged particle with mass $m_1 = m$, velocity $v_1 = v$, and momentum p, is reflected by the magnetic field which is striking several heavy clouds lying L interval with each mass $m_2 = M$ ($m \ll M$) and velocity $v_2 = -V$. This case corresponds to a head-on collision. The velocities after collision are

$$v_1' = -v + 2(-V) = -(v + 2V), \tag{A.81}$$

$$v_2' = -V. \tag{A.82}$$

The variation of the absolute momentum of the particle is

$$\begin{aligned} \Delta p_e &= m(v + 2V) - mv \\ &= 2mv\frac{V}{v} \\ &= 2p\frac{V}{v}. \end{aligned} \tag{A.83}$$

For the case of rear-end collision, we replace $v_2 = -V$ by $v_2 = V$,

$$\Delta p_f = 2p\frac{(-V)}{v}. \tag{A.84}$$

The particle gains the energy through the head-on collisions and loses the energy through the rear-end collision. The time interval between the collisions of the particle and several clouds is

$$t_{\rm coll,f} = \frac{L}{v+V}, \tag{A.85}$$

for head-on collision case. The collision frequency is

$$f_{\rm coll,f} = \frac{v+V}{L}. \tag{A.86}$$

For rear-end collision case,

$$f_{\rm coll,e} = \frac{v-V}{L}. \tag{A.87}$$

Therefore, the rear-end collision frequency is less than the head-on collision frequency. The increase rate of absolute momentum is

$$\begin{aligned} \frac{dp}{dt} &= \Delta p_f f_{\rm coll,f} + \Delta p_e f_{\rm coll,e} \\ &= \frac{4pV^2}{vL} \\ &= \frac{4pv}{L}\left(\frac{V}{v}\right)^2. \end{aligned} \tag{A.88}$$

When the velocity of the particle is relativistic ($v \sim c$),

$$\frac{dp}{dt} = \frac{4pc}{L}\beta^2, \tag{A.89}$$

where $\beta = v/c$. The increase rate of particle absolute momentum is inversely proportional to the square of β. Since $\beta < 1$, the momentum increase rate is not effective.

$$\begin{aligned} \frac{dp}{p} &= \frac{4c\beta^2}{L} \\ log\ p &= \frac{4c\beta^2}{L}t + \text{const.} \\ p &= p_0 \exp(\frac{t}{\tau_{\rm acc}}), \end{aligned} \tag{A.90}$$

where $\tau_{\rm acc}$: the acceleration time scale is

$$\tau_{\rm acc} = \frac{L}{4c}\beta^{-2}. \tag{A.91}$$

The absolute value of particle momentum (or its energy) increase exponentially with time evolution. By substituting typical values,

$$\tau_{\rm acc} = 2.2 \times 10^{17} \text{ sec} \left(\frac{L}{10 \text{ pc}} \right) \left(\frac{V}{10^6 \text{ cm s}^{-1}} \right)^{-2}. \tag{A.92}$$

Actually it is difficult for accelerating the particle via second order Fermi acceleration since $\tau_{\rm acc}$ is about the age of the universe.

We assume that all the particles escape from the system during average escape time scale $\tau_{\rm esc}$. The probability that the particle which is injected into the system at $t = 0$ stays until time t, is accelerated, and escape from the system is

$$P(t) = \exp\left(-\frac{t}{\tau_{\rm esc}} \right). \tag{A.93}$$

The momentum spectrum of the particle is

$$\begin{aligned} \frac{dN}{dp} &\propto \left| \frac{dP}{dt} \right| \frac{dt}{dp} \\ &\propto \exp\left(-\frac{t}{\tau_{\rm acc}} - \frac{t}{\tau_{\rm esc}} \right) \\ &\propto p^{-\left(1+\frac{\tau_{\rm acc}}{\tau_{\rm esc}}\right)}. \end{aligned} \tag{A.94}$$

The acceleration time scale and escape time scale depend on each supernova remnant or other system, the spectrum index of the particle momentum is underspecified.

Appendix B

VERA Data Reduction Flowchart

For reducing VERA data with dual beam mode, we have to pay attention to calibrating the phase between the two beam. Here we introduce the details of data reduction strategy especially in the case of digital filter mode VERA 7. In the total bandwidth of 256 MHz (16 IFs $\times$ 16 MHz), one of the sixteen 16 MHz IF channels was set to A beam, and assigned to the bright main calibrator 3C 345. The other 15 IF channels were set to B beam, assigned to the target Mrk 501 and another calibrator NRAO 512. [A] or [B] represent the procedure for A beam or B beam, respectively.

1. Load the FITS data files using AIPS task FITLD [A, B]
   -CL table interval: 0.05 min
   -Edit elevation limit ($\geq 80°$) visibilities at Mizusawa stations using AIPS task EDITR [A]

2. Apply *uvw*-recalculation SN tables, which are recalculated by using the same calibrator coordinates as those of VLBA observations [A,B]
   -read the file ‘ ***.A-APPLY-2A.TXT’ for A beam and ‘ ***.B-APPLY2B.TXT’ for B beam by using AIPS task TBIN
   -apply the tables using AIPS task CLCAL with parameters: interpol ‘ seln ’ ; opcode ‘ cali ’ ; smotype ‘ vlbi ’
   —CL2

3. Apply delay offset table between two beams [B]
   -read the file ‘ B-MINUS.1111’
   -apply the table using AIPS task CLCAL: interpo ‘’
   —CL3

4. Correct digital sampler bias of VERA correlator by using AIPS task ACCOR [A, B]
   -set solution interval 0.1 min

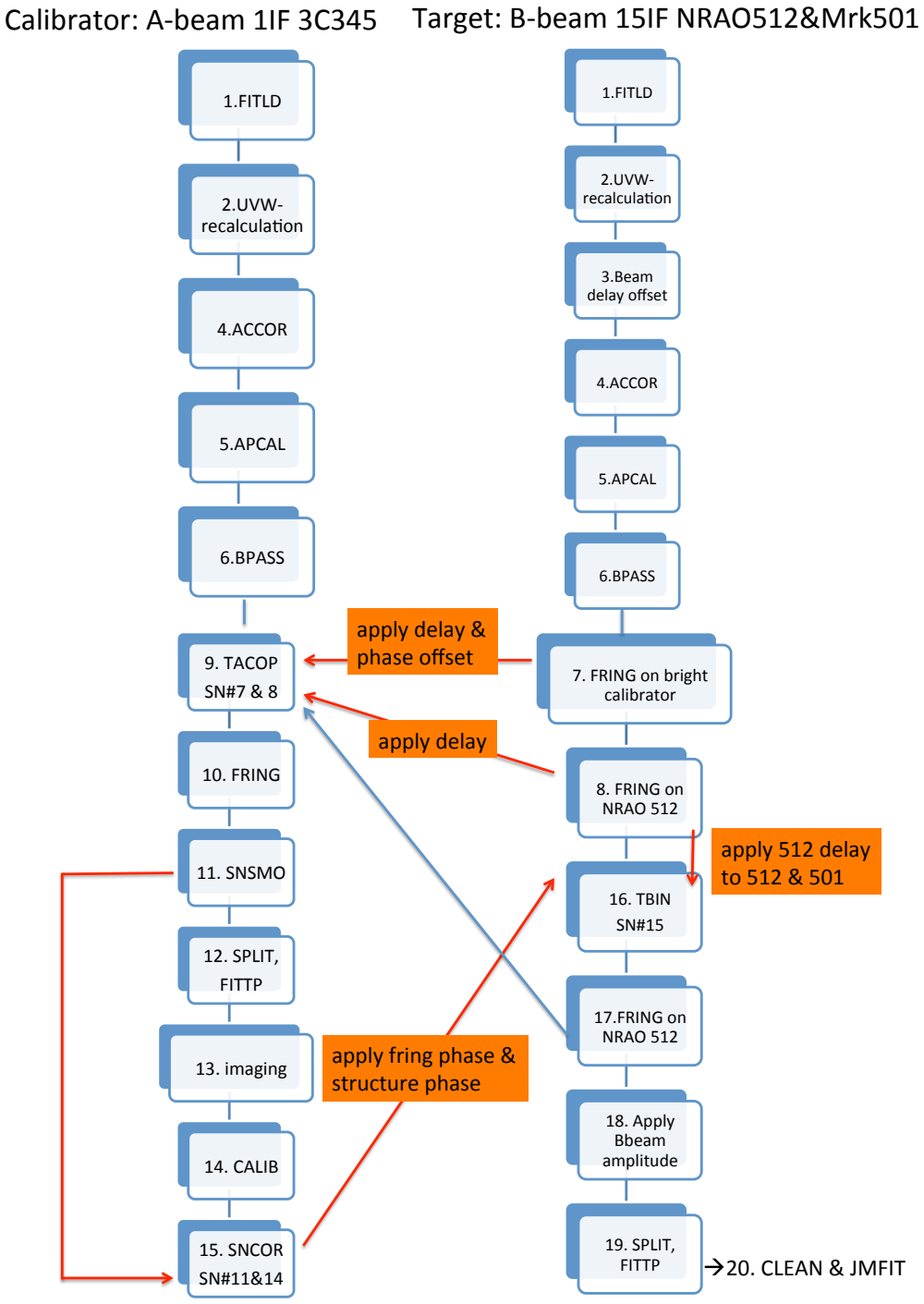

Figure B.1: Reduction flowchart of VERA continuum astrometric data.

-apply the solution using AIPS task CLCAL: interpo 'self' —CL4

5. Perform amplitude calibration with Tsys and Gain curve table by using AIPS task APCAL [A, B]
   -flag TY table above 1000K using AIPS task SNEDT
   -read GC table ver. 2009 using AIPS task TBIN
   -Correct amplitude offset between each IF channel
   -Correct beam separation angle dependency on antenna gain by using the values measured in 2004 at Iriki station
   -apply the solution table using AIPS task CLCAL: interpol 'self'
   —CL5

6. Perform bandpass calibration using AIPS task BPASS [A, B]
   -use 3C345 for A beam, and bright calibrators or NRAO 512 for B beam as calibration sources
   -use autocorrelation data: bpassprm (1)=1, (10)=1
   -use CL5
   —BP1

7. Solve single band delay in B beam by performing fringe-fitting on bright calibrator by using AIPS task FRING [B, sometimes skip here due to bad calibrator]
   -solve IF delay & phase offset by using one good scan
   -use below parameters: dparm(8)=1 (solve delay & phase), solint 5; refan 1or2; totally 4-5 scan
   -apply the solution table using AIPS task CLCAL: interpo '' ; dobtween 1
   —CL7

8. Perform global fringe-fitting on NRAO 512 using AIPS task FRING [B]
   -solve IF combined delay, rate, and phase over hole time range
   -apply this solution using AIPS task CLCAL: interpo '' ; dobtw 1
   —CL8

9. Copy the solution table from B beam to A beam using AIPS task TACOP [B—-A]
   -copy the solutions of IF channel No.9 in B beam to all IF channels using AIPS task SNCOR
   -apply the solution using AIPS task CLCAL: interpo '' ; dobtween 1
   —-CL9

10. Perform global fringe-fitting on 3C 345 in A beam using AIPS task FRING [A]
    -parameters: solint 0.5; solsub 5; doban 1;gainu 9; aparm (7) 2.8; dparm 0 100 100 0
    -apply this solution using AIPS task CLCAL
    —CL10

11. Smooth the delay and rate solutions by using AIPS task SNSMO [A]
    -parameters: samptype 'mwf', bparm 0 0 0.5 0.5, smotype 'full'
    -apply the solution using AIPS task CLCAL: interpo ' ambg ' ; dobtween -1
    —CL11

12. Split the calibrated data into single source by using AIPS task SPLIT [A]
    -aparm 2 0
    -source ' 3c345 ''
    -FITTP, CLEAN & self-cal & JMFIT [A]
    -Using difmap, perform imaging of calibrator
    -uvaver 10,tru, flag bad data
    -phase & amplitude selfcal 30min
    -wmap: output clean model

13. Solve the amplitude and phase modified through self-calibration by using AIPS task CALIB [A]
    -12&13; solmode ' A&P '

14. Leave only phase solutions by using AIPS task SNCOR [A]
    -SN11: opcode ' zdel ' — set delay=0
    -SN14: opcode ' norm ' — set amp=0
    -copy to 15IFs (other program outer AIPS)

15. Read the SN table by using AIPS task TBIN [B]
    -SN15 X2
    -CLCAL: interpo ' ambg ' ——CL16

16. Perform global fringe-fitting on NRAO 512 through FRING [B]
    -use CL16, solint 7 min(=1scan), solve phase only
    -IF offset table
    -apply the table to A beam CL9, re-fring—SN17

-apply SN17 & OF17 to B beam CL8—CL17

17. Apply B beam self-cal amplitude solutions[B]

18. Split the calibrated data into single source and average all the IFs into single IF through SPLIT
    -clean, JMFIT, model fit
    -subtract calibrator ' s core modelfit position from PR core position results

Appendix C

Phase Referencing

C.0.2 Observation equations

We consider an observing schedule of a simple phase-referencing with a pair consisting of a target (T) and calibrator (C1), both of which provide high signal-to-noise ratios enough to do self-calibration. After determination of amplitude-gain, delay and delay-rate solutions, all we have to consider is phase terms. Observed visibility phases, $\phi_{\rm OBS}$, involve various phase terms.

$$\phi^{\rm C1}_{\rm OBS} = \phi^{\rm C1}_{\rm stru} + \phi^{\rm C1}_{\rm pos} + \phi^{\rm C1}_{\rm inst} + \phi^{\rm C1}_{\rm geo} + \phi^{\rm C1}_{\rm atmo} + \phi^{\rm C1}_{\rm rapid} \quad \text{(C.1)}$$

$$\phi^{\rm T}_{\rm OBS} = \phi^{\rm T}_{\rm stru} + \phi^{\rm T}_{\rm pos} + \phi^{\rm T}_{\rm inst} + \phi^{\rm T}_{\rm geo} + \phi^{\rm T}_{\rm atmo} + \phi^{\rm T}_{\rm rapid}, \quad \text{(C.2)}$$

where, $\phi^{\rm C1}$ and $\phi^{\rm T}$ are phase terms for C1 and T, respectively. $\phi_{\rm stru}$ is a phase term originating in source structure; $\phi_{\rm pos}$ is a positional-phase delay relative to a phase-tracking center; $\phi_{\rm inst}$ is an instrumental-phase delay; $\phi_{\rm geo}$ is a geometric-phase delay error; $\phi_{\rm atmo}$ is tropospheric/ionospheric-phase delay error; $\phi_{\rm rapid}$ is a rapidly variable phase due to the non-uniform component of water vapor flowing at low altitude (< 10 km). We ignore thermal phase noise and calibration errors in the equiations. separately because we will show an astrometric term and its error expressly at the final stage. Time scales of the change of these phase-error components are usually more than several tens of minutes, except for $\phi_{\rm rapid}$ in which the time scale is typically a few minutes or less (Ulvestad et al., 1998).

C.0.3 Calibration process

We assume that sufficiently feasible source structure models for C1 and T in the form of a series of clean components ("CC model") are obtained:

$$\Phi^{\rm C1}_{\rm CC} = \Phi^{\rm C1}_{\rm stru} + \Phi^{\rm C1}_{\rm CCpos}, \quad \text{(C.3)}$$

$$\Phi^{\rm T}_{\rm CC} = \Phi^{\rm T}_{\rm stru} + \Phi^{\rm T}_{\rm CCpos}, \quad \text{(C.4)}$$

where $\Phi^{i}_{\rm stru}$ is the phase component of source structure and $\Phi^{i}_{\rm CCpos}$ is a possible positional-phase delay error (relative to a phase-tracking center) that may be included into the CC model during iterative clean–self-calibration procedures.

Before phase-referencing using C1, we desire to separate only the structure phase from the raw visibility of C1. Practically, however, we can only separate the visibility phase equivalent to the CC model from the other phase components by self-calibration with the CC model:

$$\begin{aligned} \phi^{\rm C1}_{\rm OBS} &= \Phi^{\rm C1}_{\rm CC} + \Phi_{\rm SN1}, \\ &= \Phi^{\rm C1}_{\rm stru} + (\Phi^{\rm C1}_{\rm CCpos} + \Phi_{\rm SN1}), \end{aligned} \tag{C.5}$$

where

$$\Phi_{\rm SN1} = -\Phi^{\rm C1}_{\rm CCpos} + \phi^{\rm C1}_{\rm pos} + \phi^{\rm C1}_{\rm inst} + \phi^{\rm C1}_{\rm geo} + \phi^{\rm C1}_{\rm atmo} + \phi^{\rm C1}_{\rm rapid} \tag{C.6}$$

is an antenna-based solution table that can be obtained through the self-calibration. For the purpose of subtracting only the structure phase ($\Phi^{\rm C1}_{\rm stru}$), the positional-phase delay error in the CC model ($\Phi^{\rm C1}_{\rm CCpos}$) would be remained.

With the solution table $\Phi_{\rm SN1}$, we correct the target data so that its phase is free from rapid phase fluctuations due to water vapor as follow:

$$\begin{aligned} \phi^{\rm T}_{\rm PR} &= \phi^{\rm T}_{\rm OBS} - \Phi_{\rm SN1} \\ &= \phi^{\rm T}_{\rm stru} + \phi^{\rm T}_{\rm pos} + \phi^{\rm T}_{\rm inst} + \phi^{\rm T}_{\rm geo} + \phi^{\rm T}_{\rm atmo} + \phi^{\rm T}_{\rm rapid} \\ &\quad -(-\Phi^{\rm C1}_{\rm CCpos} + \phi^{\rm C1}_{\rm pos} + \phi^{\rm C1}_{\rm inst} + \phi^{\rm C1}_{\rm geo} + \phi^{\rm C1}_{\rm atmo} + \phi^{\rm C1}_{\rm rapid}) \\ &= \phi^{\rm T}_{\rm stru} + \Phi^{\rm C1}_{\rm CCpos} + \Delta\phi^{\rm T-C1}_{\rm pos} + \Delta\phi^{\rm T-C1}_{\rm inst} + \Delta\phi^{\rm T-C1}_{\rm geo} + \Delta\phi^{\rm T-C1}_{\rm atmo} + \Delta\phi^{\rm T-C1}_{\rm rapid} \\ &\approx \phi^{\rm T}_{\rm stru} + \Phi^{\rm C1}_{\rm CCpos} + \Delta\phi^{\rm T-C1}_{\rm pos} + \Delta\phi^{\rm T-C1}_{\rm geo} + \Delta\phi^{\rm T-C1}_{\rm atmo}, \end{aligned} \tag{C.7}$$

where $\Delta\phi^{\rm T-C1}_i \equiv \phi^{\rm T}_i - \phi^{\rm C1}_i$ represents a differential phase term. Presumably, $\Delta\phi^{\rm C2-C1}_{\rm rapid} \approx 0$, because its random fluctuation is not responsible for a systematic residual, therefore, must be averaged out. Furthermore, $\Delta\phi^{\rm C2-C1}_{\rm inst} \approx 0$ because an identical receiving system is used. This is a normal phase-referencing, which has been commonly used (Beasley & Conway, 1995). The other differential phase terms may not be zero and they cause long-term phase drifts. As we mentioned above, the time scales are usually more than several tens of minutes. These remaining phase errors may cause some apparent position shift and the degradation of image dynamic range.

The resultant phase-referenced image exhibits the structure of target with some position shift and distortion. Conventionally, the astrometric position had been measured with a Gaussian model fitting to the whole structure or a conceivable target component. Actually, however, the radio source frequently includes a significant structure deviated from a Gaussian profile, for example the core–jet structure of active galactic nuclei and the cluster of astronomical masers. It is worthwhile to subtract the structure phase before the position measurement. Practically, we can subtract the visibility phase equivalent to the CC model from the phase-referenced visibility:

$$\begin{aligned} \phi^{\rm T}_{\rm PR-CC} &= (\phi^{\rm T}_{\rm OBS} - \Phi_{\rm SN1}) - \Phi^{\rm T}_{\rm CC} \\ &= \phi^{\rm T}_{\rm OBS} - \Phi^{\rm T}_{\rm stru} + \Phi_{\rm SN2} \end{aligned} \tag{C.8}$$

where

$$\Phi_{\mathrm{SN2}} = -\Delta\Phi_{\mathrm{CCpos}}^{\mathrm{T-C1}} + \Delta\phi_{\mathrm{pos}}^{\mathrm{T-C1}} + \Delta\phi_{\mathrm{geo}}^{\mathrm{T-C1}} + \Delta\phi_{\mathrm{atmo}}^{\mathrm{T-C1}}. \tag{C.9}$$

Consequently, we obtain the target image as a point source with a positional shift equivalent to astrometric information and the distortion due to remaining errors that are uncorrectable. The position measurement with a Gaussian model fitting results in the astrometric position $\Delta\phi_{\mathrm{pos}}^{\mathrm{T-C1}}$ with an error of $-\Delta\Phi_{\mathrm{CCpos}}^{\mathrm{T-C1}} + \Delta\phi_{\mathrm{geo}}^{\mathrm{T-C1}} + \Delta\phi_{\mathrm{atmo}}^{\mathrm{T-C1}}$. The error component $\Delta\Phi_{\mathrm{CCpos}}^{\mathrm{T-C1}}$ can be determined by image analyses for the self-calibrated images of T and C1.

Acknowledgement

I really appreciate the referees of this thesis, Prof. Kotaro Kohno, Prof. Shin Mineshige, Prof. Masato Tsuboi, Prof. Ken Ebisawa, and Dr. Norikazu Mizuno, for giving me the precious suggestions and comments that helped me to improve this thesis.

I appreciate Prof. Hideyuki Kobayashi, who is my supervisor, for objectively discussing this thesis. I would like to acknowledge Prof. Makoto Inoue, who was my supervisor, for providing me an environment to research at NAOJ. I deeply appreciate Dr. Motoki Kino, who patiently and responsibly supervise me since when I was an undergraduate student. He opened the way for me to study VLBI and gave me many ideas of my researches through a lot of fruitful discussions everyday. I am grateful to Dr. Akihiro Doi, who is a main adviser of my data reduction. He also supervised me from scientific aspects, and encouraged me to write this thesis. I appreciate Dr. Hiroshi Nagai, who collaborate with me since when I was an undergraduate student, give me honest advice, and continuously concern my research. I thank Dr. Kazuhiro Hada, who is the only senior of VSOP-2 group at NAOJ since I started master's course. I thank Dr. Kotaro Niinuma and Dr. Tomoaki Oyama, who deeply discuss VERA data reduction strategy. I am grateful to Dr. Mareki Honma, who encouraged and supported our VERA observations. I appreciate Dr. Tomoya Hirota, Dr. Mayumi Sato, Dr. Mikyoung Kim and Dr. Naoko Matsumoto for advising me the data reduction strategy of VERA. I thank Prof. Katsunori Shibata, who supported our VERA observations. I thank Mr. Kazunori Akiyama, who providing me the program code based on python. I thank Dr. Naoki Isobe, who gave me advice on X-ray observations of blazars and encouraged my ISAS life. I really appreciate Prof. Gabriele Giovannini, Dr. Luigina Feretti, Dr. Marcello Giroletti, and Dr. Monica Orienti for providing me the opportunities to study at Istituto di Radioastronomia in Bologna, collaborating on the studies of Mrk 501 and PKS 1510-089. I appreciate Dr. Keiichi Asada, Dr. Jun Kataoka, and Dr. David Paneque for collaborating with me on the study of Mrk 501. I am thankful to my room mates, Dr. Yoshiaki Hagiwara, Dr. Umemoto Tomofumi, and Mr. Min Choulhong, and Mrs. Akiyo Komori, for concerning me so much every day. I would like to thank all of the members of VLBI group in NAOJ and ISAS, and all of my friends at NAOJ and the University of Tokyo. I would like to appreciate Prof. Shoichi Yamada, who opened the way for me to study astrophysics and introduced Dr. Kino to me. I deeply thank my seniors and classmates of Waseda University for encouraging my research life. I am thankful to all of my precious friends for supporting me mentally. Finally, I thank my parents, grandmother, and relatives for continuously supporting me financially and mentally, and devote this thesis to

the late Takashi Kominato, the late Shizue Kominato, the late Sumio Kominato, and the late Shigeo Koyama.

最後に、研究生活をあらゆる面から支えてくれた父、母、祖母、親戚と、精神的に支えてくれた多くの友人達に心から感謝します。そして、博士になることを応援してくれていた、故、小湊高、小湊しず江、小湊純男、小山繁雄に、本論文を捧げます。

Bibliography

Abdo, A. A., Ackermann, M., Ajello, M., et al. 2011, ApJ, 727, 129

Ackermann, M., Ajello, M., Allafort, A., et al. 2011, ApJ, 743, 171

Agudo, I., Bach, U., Krichbaum, T. P., et al. 2007, A&A, 476, L17

Agudo, I., Jorstad, S. G., Marscher, A. P., et al. 2011a, ApJL, 726, L13

Agudo, I., Marscher, A. P., Jorstad, S. G., et al. 2011b, ApJL, 735, L10

Aharonian, F., Akhperjanian, A., Barrio, J., et al. 2001, ApJ, 546, 898

Aharonian, F. A., Akhperjanian, A. G., Barrio, J. A., et al. 1999, A&A, 342, 69

Albert, J., Aliu, E., & Anderhub, H. 2007, ApJ, 669, 862

Anderhub, H., Antonelli, L. A., Antoranz, P., et al. 2009, ApJ, 705, 1624

Antonucci, R. 1993, ARAA, 31, 473

Bach, U., Krichbaum, T. P., Ros, E., et al. 2005, A&A, 433, 815

Bartel, N., Herring, T. A., Ratner, M. I., Shapiro, I. I., & Corey, B. E. 1986, Nature, 319, 733

Barth, A. J., Ho, L. C., & Sargent, W. L. W. 2003, ApJ, 583, 134

Beasley, A. J., & Conway, J. E. 1995, in Astronomical Society of the Pacific Conference Series, Vol. 82, Very Long Baseline Interferometry and the VLBA, ed. J. A. Zensus, P. J. Diamond, & P. J. Napier, 327

Begelman, M. C., Fabian, A. C., & Rees, M. J. 2008, MNRAS, 384, L19

Blandford, R. D., & Königl, A. 1979, ApJ, 232, 34

Cassaro, P., Stanghellini, C., Bondi, M., et al. 1999, AAPS, 139, 601

Catanese, M., Bradbury, S. M., Breslin, A. C., et al. 1997, ApJL, 487, L143

Deller, A. T., Brisken, W. F., Phillips, C. J., et al. 2011, PASP, 123, 275

Dhawan, V., Kellermann, K. I., & Romney, J. D. 1998, ApJL, 498, L111

Djannati-Atai, A., et al. 1999, A&A, 350, 17

Doi, A., Fujisawa, K., Habe, A., et al. 2006, PASJ, 58, 777

Edwards, P. G., & Piner, B. G. 2002, ApJL, 579, L67

Finke, J. D., Dermer, C. D., & Böttcher, M. 2008, ApJ, 686, 181

Fossati, G., Maraschi, L., Celotti, A., Comastri, A., & Ghisellini, G. 1998, MNRAS, 299, 433

Gabuzda, D. C., Rastorgueva, E. A., Smith, P. S., & O'Sullivan, S. P. 2006, MNRAS, 369, 1596

Ghisellini, G., Celotti, A., Fossati, G., Maraschi, L., & Comastri, A. 1998, MNRAS, 301, 451

Giommi, P., & Padovani, P. 1994, MNRAS, 268, L51

Giroletti, M., Giovannini, G., Cotton, W. D., et al. 2008, A&A, 488, 905

Giroletti, M., Giovannini, G., Taylor, G. B., & Falomo, R. 2004a, ApJ, 613, 752

Giroletti, M., Giovannini, G., Feretti, L., et al. 2004b, ApJ, 600, 127

Guetta, D., Ghisellini, G., Lazzati, D., & Celotti, A. 2004, A&A, 421, 877

Hartman, R. C., Bertsch, D. L., Bloom, S. D., et al. 1999, ApJS, 123, 79

Honma, M., Tamura, Y., & Reid, M. J. 2008, PASJ, 60, 951

Honma, M., Fujii, T., Hirota, T., et al. 2003, PASJ, 55, L57

Iguchi, S., Kkurayama, T., Kawaguchi, N., & Kawakami, K. 2005, PASJ, 57, 259

Isobe, N., Sugimori, K., Kawai, N., et al. 2010, PASJ, 62, L55

Iwashimizu, C. 2001, Master thesis

Jorstad, S. G., Marscher, A. P., Larionov, V. M., et al. 2010, ApJ, 715, 362

Jung, T., Sohn, B. W., Kobayashi, H., et al. 2011, PASJ, 63, 375

Kameno, S., Inoue, M., Fujisawa, K., Shen, Z.-Q., & Wajima, K. 2000, PASJ, 52, 1045

Kataoka, J. 1999, Ph.D. thesis

Kataoka, J., Takahashi, T., Makino, F., et al. 2000, ApJ, 528, 243

Kataoka, J., Takahashi, T., Wagner, S. J., et al. 2001, ApJ, 560, 659

Kawaguchi, N., Sasao, T., & Manabe, S. 2000, in Society of Photo-Optical Instrumentation Engineers (SPIE) Conference Series, Vol. 4015, Society of Photo-Optical Instrumentation Engineers (SPIE) Conference Series, ed. H. R. Butcher, 544–551

Kellermann, K. I., Sramek, R., Schmidt, M., Shaffer, D. B., & Green, R. 1989, AJ, 98, 1195

Kino, M., Mizuta, A., & Yamada, S. 2004, ApJ, 611, 1021

Kino, M., & Takahara, F. 2008, MNRAS, 383, 713

Kino, M., Takahara, F., & Kusunose, M. 2002, ApJ, 564, 97

Kobayashi, S., Piran, T., & Sari, R. 1997, ApJ, 490, 92

Komatsu, E., Dunkley, J., Nolta, M. R., et al. 2009, ApJS, 180, 330

Konigl, A. 1981, ApJ, 243, 700

Kovalev, Y. Y., Lobanov, A. P., Pushkarev, A. B., & Zensus, J. A. 2008, A&A, 483, 759

Lipovetsky, V. A., Markarian, B. E., & Stepanian, J. A. 1987, in IAU Symposium, Vol. 121, Observational Evidence of Activity in Galaxies, ed. E. E. Khachikian, K. J. Fricke, & J. Melnick, 17

Lobanov, A. P. 1998, A&A, 330, 79

Lobanov, A. P., & Roland, J. 2005, A&A, 431, 831

Lu, R.-S., Fish, V. L., Weintroub, J., et al. 2012, ApJL, 757, L14

Lu, R.-S., Fish, V. L., Akiyama, K., et al. 2013, ApJ, 772, 13

Marcaide, J. M., & Shapiro, I. I. 1984, ApJ, 276, 56

Marscher, A. P., Jorstad, S. G., D'Arcangelo, F. D., et al. 2008, Nature, 452, 966

McKinney, J. C., Tchekhovskoy, A., & Blandford, R. D. 2013, Science, 339, 49

Mimica, P., & Aloy, M. A. 2010, MNRAS, 401, 525

Nagai, H., Kino, M., Niinuma, K., et al. 2013, PASJ, 65, 24

Nakar, E., & Piran, T. 2002, ApJL, 572, L139

Orienti, M., Venturi, T., Dallacasa, D., et al. 2011, MNRAS, 417, 359

Orienti, M., Koyama, S., D'Ammando, F., et al. 2012, MNRAS, 169

Osterbrock, D. E. 1981, ApJ, 249, 462

O'Sullivan, S. P., & Gabuzda, D. C. 2009, MNRAS, 400, 26

Peterson, B. M. 1997, An Introduction to Active Galactic Nuclei

Pian, E., Vacanti, G., Tagliaferri, G., et al. 1998, ApJL, 492, L17

Piner, B. G., & Edwards, P. G. 2004, ApJ, 600, 115

Piner, B. G., Pant, N., & Edwards, P. G. 2010, ApJ, 723, 1150

Piner, B. G., Pant, N., Edwards, P. G., & Wiik, K. 2009, ApJL, 690, L31

Piran, T. 1999, PhR, 314, 575

Pradel, N., Charlot, P., & Lestrade, J.-F. 2006, A&A, 452, 1099

Pushkarev, A. B., Hovatta, T., Kovalev, Y. Y., et al. 2012, A&A, 545, A113

Quinn, J., Akerlof, C. W., Biller, S., et al. 1996, ApJL, 456, L83

Rees, M. J. 1978, MNRAS, 184, 61P

Reid, M. J., Readhead, A. C. S., Vermeulen, R. C., & Treuhaft, R. N. 1999, ApJ, 524, 816

Rieger, F. M., & Mannheim, K. 2003, A&A, 397, 121

Rybicki, G. B., & Lightman, A. P. 1979, Radiative processes in astrophysics

Samuelson, F. W., Biller, S. D., Bond, I. H., et al. 1998, ApJL, 501, L17

Savolainen, T., Wiik, K., Valtaoja, E., & Tornikoski, M. 2006, A&A, 446, 71

Shapiro, I. I., Wittels, J. J., Counselman, III, C. C., et al. 1979, AJ, 84, 1459

Shepherd, M. C. 1997, in Astronomical Society of the Pacific Conference Series, Vol. 125, Astronomical Data Analysis Software and Systems VI, ed. G. Hunt & H. Payne, 77

Sokolovsky, K. V., Kovalev, Y. Y., Lobanov, A. P., et al. 2010, ArXiv e-prints

Sokolovsky, K. V., Kovalev, Y. Y., Pushkarev, A. B., & Lobanov, A. P. 2011, A&A, 532, A38

Spada, M., Ghisellini, G., Lazzati, D., & Celotti, A. 2001a, MNRAS, 325, 1559

Spada, M., Lazzati, D., Ghisellini, G., & Celotti, A. 2001b, MmSAI, 72, 157

Takahashi, T., Kataoka, J., Madejski, G., et al. 2000, ApJL, 542, L105

Tanihata, C., Takahashi, T., Kataoka, J., & Madejski, G. M. 2003, ApJ, 584, 153

Tanihata, C., Urry, C. M., Takahashi, T., et al. 2001, ApJ, 563, 569

Tavecchio, F., Maraschi, L., Pian, E., et al. 2001, ApJ, 554, 725

Thompson, A. R., Moran, J. M., & Swenson, Jr., G. W. 2001, Interferometry and Synthesis in Radio Astronomy, 2nd Edition

Ulrich, M.-H., Kinman, T. D., Lynds, C. R., Rieke, G. H., & Ekers, R. D. 1975, ApJ, 198, 261

Ulvestad, J. S., Roy, A. L., Colbert, E. J. M., & Wilson, A. S. 1998, ApJ, 496, 196

Urry, C. M., & Padovani, P. 1995, PASP, 107, 803